Mikko Saarinen

Cantilever enhanced gas sensing using photoacoustic spectroscopy

Faculty of Electronics, Communications and Automation

Thesis submitted for examination for the degree of Master of Science in Technology.

Espoo 27.9.2010

Thesis supervisor:

Prof. Ilkka Tittonen

Thesis instructor:

M.Sc. (Tech.) Päivi Sievilä

Aalto University
School of Science
and Technology

AALTO UNIVERSITY
SCHOOL OF SCIENCE AND TECHNOLOGY

ABSTRACT OF THE
MASTER'S THESIS

Author: Mikko Saarinen

Title: Cantilever enhanced gas sensing using photoacoustic spectroscopy

Date: 27.9.2010 Language: English Number of pages:10+73

Faculty of Electronics, Communications and Automation

Department of Micro and Nanosciences

Professorship: Electrophysics Code: S-129

Supervisor: Prof. Ilkka Tittonen

Instructor: M.Sc. (Tech.) Päivi Sievilä

The ability to detect small amount of trace gases is vital in many applications. The photoacoustic spectroscopy is one of the methods that produce the most sensitive detection schemes. It is based on detecting a gas specific acoustic wave generated in the absorption of light. The sensitivity of the traditional membrane microphones is limited by electrical noise and the nonlinearity of the displacement of the mechanical sensor at high optical power levels. Membrane microphones have been therefore replaced with optically measured cantilevers in the most sensitive systems. Even though a MEMS cantilever has shown the best sensitivity to date, further work is needed to fully exploit its full potential.

This thesis consists of two parts. The first part gives a review of the photoacoustic effect and the components used to build a photoacoustic system based on the literature. In addition, a brief review of the fabrication process of cantilevers is given. In the second part, a photoacoustic setup assembled at Micronova is used to compare the theoretical model with the measured signal spectra of the cantilevers. The cantilever design is like a tight micromachined "door" in which the gas leakage through the gap between the moving door and the frame is of crucial importance. The used model could explain the experimental data very well when this narrow gap is in a few μm range. For larger gaps, the gas leakage and dynamics change the overall behaviour so much that the agreement becomes worse.

The sensitivity of the microfabricated cantilevers is mainly limited by a gas spring. Therefore various shapes for the component were modeled with the finite element method (FEM) showing that the effective spring constant can be efficiently altered by perforating the cantilever.

Keywords: Cantilever, Photoacoustics,
Spectrosopy, Microfabrication

AALTO-YLIOPISTO
TEKNILLINEN KORKEAKOULU

DIPLOMITYÖN
TIIVISTELMÄ

Tekijä: Mikko Saarinen

Työn nimi: Kaasun mittaaminen piiläppään perustuvalla fotoakustisella spektroskopialla

Päivämäärä: 27.9.2010 Kieli: Englanti Sivumäärä:10+73

Elektroniikan, tietoliikenteen ja automaation tiedekunta

Mikro- ja nanotekniikan laitos

Professuuri: Sähköfysiikka Koodi: S-129

Valvoja: Prof. Ilkka Tittonen

Ohjaaja: DI Päivi Sievilä

Monet sovellukset vaativat erittäin pienten kaasumäärien tunnistamista. Tähän tarkoitukseen on kehitetty monia tekniikoita, joista fotoakustisella spektroskopialla on saavutettu kaikkein herkimpiä tuloksia. Menetelmä perustuu näytekaasun synnyttämään akustiseen aaltoon, joka syntyy kaasun absorboidessa valoa. Kalvomikrofonien herkkyyttä rajoittaa mittaukseen kytkeytyvä elektroninen kohina, sekä kalvon mekaanisen liikkeen epälineaarisuus suuria optisia tehoja käytettäessä. Tästä syystä herkimpiä mittauksia varten kalvomikrofonit on korvattu optisesti mitattavalla, oven tavoin toimivalla, palkilla. Palkki on erotettu kehyksestä kolmelta sivulta kapealla raolla. Vaikka mikromekaanisilla palkeilla onkin saavutettu pienimmät mitatut herkkyydet, vaatii niiden vahvuuksien täydellinen hyödyntäminen vielä lisää tutkimusta.

Tämä työ muodustuu kahdesta osasta. Ensimmäisessä osassa tehdään kirjallisuuskatsaus fotoakustiseen ilmiöön ja sitä hyödyntävän laitteiston vaatimiin osiin. Lisäksi esitellään piipalkkien valmistukseen käytetty prosessi. Toisessa osassa Micronovaan kootulla järjestelmällä mitattuja signaalispektrejä verrataan teoreettiseen malliin. Vaikka mallin antamat tulokset vastaavatkin mitattuja arvoja käytettäessä kapeita rakoja, huomattiin mallin ja kokeellisten tulosten välillä suuria poikkeamia sekä signaali- että kohinaspektrissä, kun raon leveyttä kasvatettiin.

Piipalkkien herkkyyttä rajoittaa pääasiassa näytekaasun aiheuttama kaasujousi. Kaasujousen vaikutuksen vähentämiseksi työssä mallinnetaan elementtimenetelmällä (FEM) eri muotoisia antureita. Mallien perusteella palkin perforointi pienentää efektiivistä jousivakiota tehokkaasti.

Avainsanat: Piipalkki, Fotoakustiikka,
Spektroskopia, Mikrovalmistus

Preface

I would like to thank my supervisor professor Ilkka Tittonen for the chance to write my thesis in Micro and Quantum Systems group. Special thanks to my instructor Päivi Sievilä for our several discussions considering this thesis and for teaching me the fabrication process of the cantilevers.

I also want thank to Nikolai Chekurov, Ville Pale, Osmo Vänskä and Ossi Kimmelma for their help with various things related to this thesis. I am also very grateful to professor Jyrki Kauppinen and Tom Kuusela at the University of Turku, who offered helpful discussion and the possibility to make the first measurements with our cantilevers.

Otaniemi, 27.9.2010

Mikko Saarinen

Contents

Symbols and abbreviations

Symbols

c_p	specific heat capasity at constant pressure [J/K]
c_V	specific heat capacity at constant volume [J/kgK]
d	distance between electrodes [m]
dU	change of internal energy [J]
dW	work done by a system [J]
f	frequency [Hz]
f_0	resonance frequency [Hz]
f_s	sampling frequency [Hz]
h	Planck's constant $\approx 6.626 \times 10^{-34}[\mathrm{m^2kg/s}]$
k	effective spring constant [N/m]
k_0	spring constant[N/m]
k_B	Boltzmann constant $\approx 1.3807 \times 10^{-23}[\mathrm{m^2kg/s^2K}]$
l	absorption path length [m]
l_c	length of the cantilever [m]
l_pipe	length of a pipe resonator [m]
m	mass [kg]
m_C	mass of the cantilever [kg]
m_eff	effective mass [kg]
m_mol	mass of a gas molecule [kg]
n	number of moles
n_j	complex refractive index
p	pressure [Pa]
r	radius of the sample cell [m]
t	thickness of the cantilever [m]
t	time [s]
v_avg	average speed [m/s]
v_sound	speed of sound [m/s]
w	width of the cantilever [m]
x	displacement [m]
x_i	input element
y	distance from the base of the cantilever [m]
y_i	output element

A	common area of the electrodes [m^2]
A_C	surface area of the cantilever [m^2]
A_g	area of gap between the frame and the cantilever [m^2]
$A(\omega)$	amplitude of the displacement of the cantilever [m]
B	maximum change in the wavelength [m]
C	capacitance [F]
C_V	total heat capacity [J/K]
D	damping constant [Ns/m]
D_{CM}	distance between center of masses [m]
E	Young's modulus [Pa]
E_1	real part of the Young's modulus
E_2	complex part of the Young's modulus
F	force [N]
F_0	amplitude of external force [N]
$F_{ext}(t)$	time depending external force [N]
F_{th}	random force due to thermal fluctuations [N]
G	thermal conductivity [W/Km]
$H(\omega)$	transfer function
I	moment of inertia [m^4]
N_{FFT}	block size of the fast fourier transform
P_0	maximum power [W]
Q	quality factor
Q	thermal energy [J]
$Q_{clamping}$	Q value due to clamping of the cantilever
Q_{TED}	thermoelastic Q value
Q_{volume}	Q value due to volume effects
$Q_{surface}$	Q value due to surface effects
R	radius of a membrane [m]
R	reflectance
S_1	noise spectrum of 1/f noise
S_2	noise spectrum of Brownian noise
$S_{th}(\omega)$	spectral power density function
T	temperature [K]
T_0	initial temperature [K]
U	internal energy [J]
U_x	signal from detector x [V]
V	volume [m^3]
V^*	effective volume [m^3]
V_{eff}	effective volume [m^3]
$W(r)$	radius dependent thermal diffusion

α	coefficient of the thermal expansion [1/K]
α_{x}	absorption coefficient [1/m]
γ	ratio of specific heat capacities
δ	surface thicknesss [m]
δQ	change in heat energy [J]
ϵ	permittivity [F/m]
λ	wavelength [m]
$\lambda(0)$	wavelength of the absorption peak [m]
μ	thermal diffusion length [m]
ρ_{C}	density of the cantilever [kg/m^3]
ρ_{gas}	density of gas [kg/m^3]
ρ_{Si}	density of silicon $\approx 2,330 \times 10^3$[kg/m^3]
σ^2	spectral power density [W/Hz]
τ	decay time [s]
τ_1	time constant due the gas heating [s]
τ_2	time constant due the gas transfer through gap [s]
τ_{23}	time constant due gas leakge from the frame gap [s]
τ_3	time constant due the heat transfer through gap [s]
τ_{m}	measurement time [s]
τ_{rel}	time constant due the relaxation time [s]
ϕ	phase shift [rad]
ω	angular frequency [rad/s]
ω_0	resonance angular frequency [rad/s]
Δa	amplitude of acceleration [m/s^2]
ΔA	change in the common area of the membranes [m^2]
Δf	frequency resolution [Hz]
Δl	end correction of a pipe resonator [m]
Δp	acoustical noise pressure [Pa]
Δx	amplitude of displacement [m]
Δx_{rms}	root-mean-square displacement [m]
$\Delta\omega$	bandwidth of the resonator [rad/s]

Abbreviations

AFM	atomic force microscopy
AM	amplitude modulation
BHF	buffered hydrofluoric acid
CO	carbon monoxide
DFB	distributed feedback
DHF	dilute hydrofluoric acid
DME	differential mode excitation
DRIE	deep reactive ion etching
DSP	digital signal processor
ECDL	external cavity diode laser
EDFA	erbium doped fiber amplifier
EDP	ethylenediamine pyrocatechol
FEM	finite element method
FFT	fast fourier transform
FTIR	Fourier transform infrared
H_2O	water
HDMS	hexamethyl disilazane
IPA	isopropyl alcohol
IR	infrared
KOH	potassium hydroxide
LPCVD	low pressure chemical vapor deposition
LTO	low temperature deposited silicon dioxide
N_2O	nitrous oxide
NA	numerical aperture
NNEA	normalized noise equivalent absorption coefficient
OPO	optical parametric oscillator
PAS	photoacoustic spectroscopy
QC	quantum cascade
QEPAS	quartz enhanced photoacoustic spectroscopy
QSW	quasi-square modulation waveform
QTF	quartz tuning fork
RIE	reactive ion etching
SAW	surface acoustic wave
SNR	signal-to-noise ratio
SOI	silicon-on-insulator
TED	thermoelastic dissipation
TMAH	tetramethylammonium hydroxide
UV	ultraviolet
WMS	wavelength-modulation spectroscopy

1 Introduction

1.1 Applications and methods of trace gas detection

At present, the ability to detect small amounts of trace gases plays an important role in many real world applications. A lot of scientific research is focused on environmental issues, for example greenhouse effect, global warming, acid rains, the destruction of ozone layer and air pollution. Photoacoustic spectroscopy (PAS) is a method that can be used to measure stack gases from the power plants, air pollutants from the car exhausts and nitrification of soil. The applications of the trace gas detection include plant physiology in biology, the nitrogen detection of biological systems in microbiology and noninvasive breath analysis in the medicine [1].

Photoacoustic spectroscopy is also used in military, security and industrial applications to identify and detect the presence of explosive ordnances, the weapons of mass destruction and chemical warfare agents from a very small amount of trace gas species they release [2]. Typical requirements for all the applications of the photoacoustic spectroscopy are selectivity, sensitivity or good signal-to-noise ratio (SNR), long-term stability, a low limit of detection, a large dynamic range, a low number of false alarms, ability to measure multiple components with the same equipment, fast response time and good time resolution and easy calibration [3, 4]. Additional properties desired include usually portability and a low price.

Trace gases can be detected with various methods, which can be divided into spectroscopic and nonspectroscopic techniques. Most of the spectroscopic techniques are based on the detection of the absorption spectrum of the molecules in infrared (IR) region. Two of the most used nonspectroscopic techniques are chemiluminescence and gas chromatography. The chemiluminescence is based on the emission of electromagnetic radiation as a result of the relaxation of energy excited by chemical reactions. This requires modifying the composition of the sample gas, which is not possible in some applications. Gas chromatography can be used to detect several components almost simultaneously, but it requires preparation and extraction of the sample gas making the measuring slow. [5]

Photoacoustic spectroscopy can be used to detect very low concentrations relatively quickly. The total size of the system can be made small making it possible to have portable systems capable to in-situ measurements. The photoacoustic system is immune to the background signal in the absence of the sample gas since it measures absorbed energy. A photoacoustic system is usually used with a tunable source making it possible to measure multiple components from the sample with a single system. Since the signal is measured with a microphone, the photoacoustic system can be used with a wide range of wavelengths. Other optical spectroscopic techniques such as Raman spectroscopy, fluorescence, optical reflection and transmission, luminescence and laser induced breakdown spectroscopy require an optical detector, whose response can depend strongly on from the wavelength. A photoacoustic system can also be combined with several techniques, for example Fourier transform infrared (FTIR). Photoacoustic systems also have a very wide dynamic range, which reduces the need for calibrations. [5]

1.2 History of photoacoustic spectroscopy

Photoacoustic effect was documented for the first time in 1880 when Bell invented by accident a process, where a rotating disc modulated sunlight focused on a sample disc, which absorbed photons and generated an acoustic signal. In his later experiments, a sample cell containing absorbing material in the focal point of a lens was connected to a listening tube, which formed an audible acoustical wave at the modulating frequency. This work was continued by Tyndall and Röntgen, who made several experiments with solid, liquid and gaseous samples. These works stirred some interest in the photoacoustic spectroscopy but the use of the method was limited by the lack of high powered infrared sources and the insensitivity of microphones. The first significant improvement in the photoacoustic spectroscopy was made in 1938 when Viengerov used a blackbody radiator and an electrostatic microphone to measure gas concentrations. Development was continued by Luft, who invented differential design using two photoacoustic cells and broadband infrared source gaining major improvements in selectivity and sensitivity. [1, 6]

The invention of the laser made high powered infrared sources available. In 1968, Kerr and Atwood demonstrated a laser illuminated absorption spectrophone. With the help of enhanced lock-in amplifiers, they managed to improve the photoacoustic signal and measure very low concentrations of air pollutants. Three years later, Kreuzer made experiments with intensity modulated infrared HeNe-laser. He used photoacoustic spectroscopy to measure 10^{-8} parts of methane in nitrogen with photoacoustic spectroscopy. [1]

Even though Röntgen and Tyndall had made experiments with photoacoustic effect in solid materials nearly a century earlier, it had not gained as much attention as the gas spectroscopy. The interest in solids was revived by Parker in 1970's. His work was continued by Rosencwaig and Gersho who explained the theory of photoacoustic in solids. By the end of the 1970's, the mechanisms behind the photoacoustic effect in solids were well understood. [7]

1.3 Principle of photoacoustic spectroscopy

The photoacoustic system is based on the excitation of molecules in a sample gas from the ground state to excited states by infrared light. The number of the excited molecules depends on the intensity and spectrum of the incoming light as well as the absorption spectrum and the absorption cross section of the molecules. The non-radiative decay of excited molecules generates heat variations, which leads to pressure variations by thermal expansion as depicted in Fig. 1. [3]

A typical photoacoustic spectroscopy system is shown in Fig. 2. An optical source, which is usually a laser or a ceramic blackbody radiator, emits IR radiation. The IR beam is chopped with an electrical or a mechanical chopper and directed to the sample cell. Commonly used modulating frequencies for the photoacoustic system vary from 10 Hz to several dozens of kHz depending on the detector. When a blackbody radiator is used, one or more optical filters are required in order to separate different gases. Absorption of IR radiation increases pressure in a closed

Figure 1: Signal generation from the laser to the microphone.

sample cell. The modulation of the IR beam forces pressure in the sample cell to vibrate with the same frequency. Sound waves created by the variations of the pressure are converted into an electric signal with an acoustic detector, for example a condenser microphone. The signal can be seen in the measured spectrum as a peak at the modulation frequency. [3]

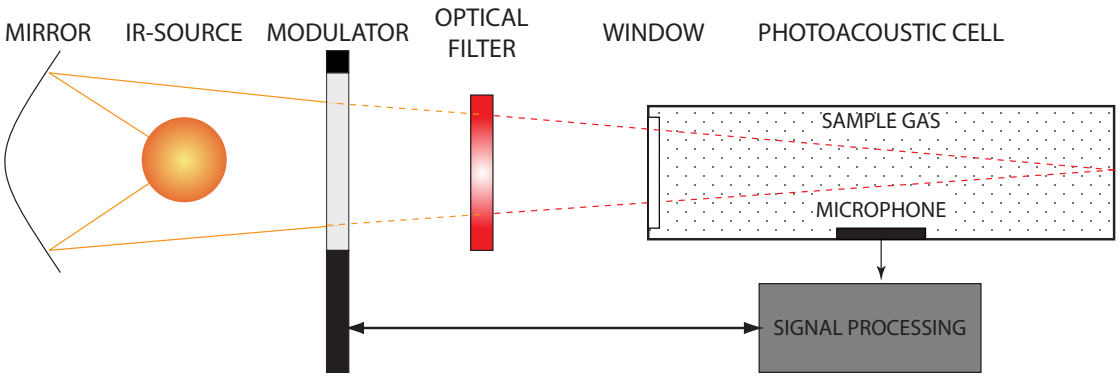

Figure 2: A photoacoustic spectroscopy system.

The selectivity of a photoacoustic spectroscopic system can be achieved by using a tunable laser. Each molecule has unique absorption spectrum, i.e. they absorb radiation only at certain narrow wavelengths. In the simplest case, the absorption peaks of different components do not overlap and the selectivity is achieved simply by tuning the source wavelength and comparing the results with a component library. In reality, the absorption peaks overlap with each other and algorithms must be used in order to differentiate multiple components. Another way to get good selectivity is to use a differential system, which can be used to separate different molecules. [4]

The sensitivity of the PAS system can be increased by increasing the signal or by decreasing the noise. The most direct way to increase the signal is to use higher powered infrared source but it can also be improved with a proper design of the sample cell. The noise is decreased with active or passive dampeners but the sample cell design is also used to reduce noise. Chapter 2 presents various sources, sample cell designs and acoustic detectors used to improve the photoacoustic system.

1.4 Microfabricated cantilever

The sensitivity of the photoacoustic spectroscopy system can be further increased over hundredfold times by replacing the condenser microphone with a microfabricated cantilever. The microfabricated cantilever is a rectangular, mm^2 sized piece of silicon that is connected to a frame from a single side shown in Fig. 3. A small, few μm wide gap is surrounding the cantilever from three sides. The pressure variations can bend the free end of the cantilever and the displacement can then be measured optically or electrically.

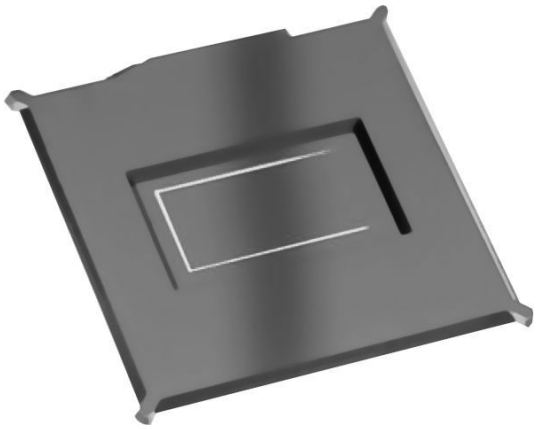

Figure 3: A microfabricated cantilever. Courtesy of Päivi Sievilä.

A cantilever enhanced photoacoustic spectroscopy system can be used to detect sample gas concentrations down to few parts per billion by volume. While a cantilever based microphone with an interferometric detection system has superior sensitivity compared with an electric microphone, it is also less robust and bulkier solution. Due to the optical measurement, the cantilever does not act as a heat source and cause extra noise in the measurement based on the heating of the sample gas.

Unlike electric microphones, these microfabricated cantilevers are not available off-the-shelf. The cantilevers analyzed in this work are made in the cleanroom at the Micronova, which makes it possible to modify them substantially. Cantilevers for photoacoustic spectroscopy have not been studied very widely and further research might enhance their properties significantly.

1.5 Goals of this thesis

The main theme of this work is to optimize the cantilevers as a part of a PAS system. In order to test them in their intended environment, a measurement setup is assembled at Micronova. The system is based on a photoacoustic cell and control electronics manufactured by Gasera Ltd. Before the system is acquired, a literature review of the essential components of the photoacoustic system is made. In order to understand the weaknesses and strengths of the measurement setup, an insight of the development and structure of the PAS system are needed.

Since the cantilevers are relatively new type of optical microphones for photoacoustic spectroscopy, their properties are not completely known. The cantilevers cannot be developed without a solid knowledge of the physics behind the signal generation in the photoacoustic system and thus Chapter 3 concentrates on the signal and noise generation in the photoacoustic systems. Work has been done in order to predict the noise components in the total system response but there are still unknown factors in noise properties. The noise spectrum is mostly dominated by 1/f noise and Brownian noise, which are also the main interest of the noise measurements.

In order to develop the cantilevers, their shape and dimensions need to be optimized. Since the fabrication process requires time and effort, the new shapes are modeled before they will be made. Chapter 4 presents the fabrication process used to make the micromachined cantilevers, since it limits the possible structures. Second part of the chapter presents alternative materials and shapes for the cantilevers. Chapter 5 gives a detailed account of the measurement setup and the measured cantilevers. The measured sample gases are carbon dioxide in the air and pure nitrous oxide. The results of these measurements and their future prospects and challenges will be discussed in Chapters 6 and 7.

2 Photoacoustic spectroscopy

Photoacoustic spectroscopy is based on the ability to measure pressure variations caused by the absorption of the infrared radiation. The signal is directly related to the power of the source and the selectivity to the bandwidth of the IR radiation. While the invention of the lasers was a cornerstone for a PAS system, ceramic blackbody radiators are still used because of their wide spectral range even though tunable laser types are becoming more common. In addition to the infrared source, a modulator is needed. Mechanical choppers are usually used with blackbody radiators even though they can be replaced with electronically controlled resistor networks. The amplitude or the frequency of the lasers are usually modulated electrically, which generates lower noise than a mechanical chopper.

The sample cell is used to couple the infrared radiation to the sample gas. The design of the sample cell is usually a compromise between a small sample volume and a long absorption length. The sample cell diameter is limited by the beam size since the absorption of the walls would lead to increased noise. The signal-to-noise ratio can be enhanced by various ways even if the volume is kept constant. Methods in use are for example multipass cells, low loss windows or acoustic resonators.

The membrane microphones have limited dynamic range due to their structure and therefore they limit the sensitivity of the photoacoustic system. The first microfabricated cantilever microphone was built by Lee, Ried and White in 1996. This novel microphone structure was free from the residual stress caused by the clamped-clamped structure used in the earlier microphones. In 2003, an optically measured cantilever was used to replace the traditional membrane microphone in a PAS system by Wilcken and Kauppinen resulting in significant improvement in the sensitivity. [8]

2.1 Infrared sources

Sources of periodic radiation used to excite electrons are blackbody radiators, lasers and LEDs. The infrared source must emit radiation at wavelengths matching the absorption spectrum of the sample gas. In addition to overlapping the absorption peak, the linedwidth of the source should not overlap with the absorption peak of other gases. For example, water vapor has 364 absorption lines, carbon dioxide 2511 lines and carbon monoxide 31 lines within the optical telecommunication C band covering 1530...1565 nm [9]. When suitable radiation is available, the radiation will be absorbed in the sample cell accordingly to the Beer-Lambert law. The absorbed energy will then be transformed to heat inside the sample cell.

2.1.1 Source types

A blackbody radiator with one or more optical filters can have wide tunability over IR-region according to the Planck's radiation law. A considerable number of the most important trace gases have strong absorption bands in the mid-infrared region that can be covered with a radiator heated to 200...500 °C, even though Planckian

sources suit even a wider range of temperatures. The wide bandwidth of blackbody radiators makes it possible to measure multiple components at the same time but in order to distinguish them from each other optical filtering is needed. For good selectivity, multiple optical filters are usually needed. [10]

Since the intensity of a blackbody source is lower than the intensity of a laser, a large sized high temperature radiator with collimating optics is required for high signal levels. A large ceramic blackbody radiator warms up relatively slowly (1...10 min) and must therefore be modulated with a mechanical chopper that can cause unwanted noise and reduce the mechanical reliability of the system. The ceramic source can be replaced with a network of tiny resistors that can be directly modulated up to 50 Hz. Even large radiator networks have simpler structure than the lasers making them more robust sources. [10]

When a high powered source is needed, lasers are used. In the simplest from, a laser is a cavity filled with amplifying medium ended with two mirrors. When energy is fed to the amplifying medium, electrons are excited to higher states. When a photon, which energy corresponds to the difference between two energy states in the medium, travels through the medium, additional photons with the same phase can be emitted through the relaxation of the electrons. Thus a beam reflecting between the mirrors becomes stronger. If one of the mirrors is partially transmitting, a high intensity beam with a narrow linewidth can be acquired.

Tunable gas laser sources such as CO and CO_2 lasers had significant part in the advancement of photoacoustic spectroscopy in the 1970s and 1980s. Lasers could achieve several watts of optical power tuned in the fundamental absorption band of the gas. The narrow bandwidth of the laser took the sensitivity of photoacoustic systems to a new level. Even though tunable gas lasers tended to be complex and bulky, their advantages compensated their faults. Advancement of lasers reduced their size and complexity making laser sources even a more attractive choice for a compact PAS system. [11]

Diode lasers offer a smaller, cheaper and more reliable alternative for gas lasers. A near infrared region diode laser operated at the room temperature cannot compete with CO_x lasers in optical power, but they made up this lack of power with longer lifetime and easier electrical amplitude and wavelength modulation. Limited tuning range can be extended with external cavity diode lasers (ECDL) up to 60...100 nm [12]. The power of diode lasers can be increased with optical fiber amplifiers more typically used in telecommunication systems. A high powered pump laser is coupled with an IR laser into a rare-earth ion doped fiber. Energy is transferred from the pump laser to the signal laser through the excitation of ions and stimulated emission of radiation. Erbium doped fiber amplifiers (EDFA) can amplify the optical power of a diode laser from a typical value of 10 mW to several watts. Increased power makes it possible to achieve high sensitivity even with a low powered diode laser. [11, 13]

Standard *distributed feedback* (DFB) lasers used in optical telecommunication systems are also widely used in compact PAS systems in the near infrared region. Their frequency and amplitude can be easily tuned by modulating the injection current, they have high reliability and they are easy to couple into optical fibers.

The wavelength of a DFB laser can easily be tuned a few nanometers, which is enough for the detection of multiple gases even though the range is much lower than what is achieved with external cavities. In addition DFB lasers are compatible with optical fibers making the coupling and the alignment much easier. Even a relatively low powered DFB laser used in this thesis produced an infrared beam strong enough to measure the absorption peaks of carbon dioxide in air. [13, 14]

Development of a continuous wave *optical parametric oscillator* (OPO) systems opened up possibility for a compact laser source with a large continuous tuning range and a relatively high optical power. OPO system with a temperature controlled, periodically poled $LiNbO_3$ crystal can be tuned from 1400 to 2000 nm. OPO systems can produce over 100 mW optical power. An optical parameter oscillator is based on power transfer from a pump laser to a signal and an idler beams in a nonlinear crystal. The output beam bandwidth can be limited down to 0.1 nm with properly selected etalons or gratings. [15]

Novel promising laser sources are *quantum cascade* (QC) and *interband cascade lasers*. Thermo-electrically cooled InGaAs/InAlAs heterostructure QC lasers can operate at several hundred mW within a very narrow bandwidth. A temperature controlled QC laser chip with DFB structure can have a tuning range of a few hundred nanometers. Structures using bound-to-continuum transitions and heterogeneous structure can be tuned over 3 μm around 10 μm. With the help of an external cavity, the QC laser resolution can be better than 10 pm, which is similar to the linewidth of the absorption peaks of the most common trace gases. [9, 16]

2.1.2 Modulation schemes

Photoacoustic spectroscopy is considered as a first order system where should be no signal if suitable molecules are not present. Still, the *amplitude modulation* (AM) can excite a coherent background noise with the signal due to the thermal absorption of the window and the nonselective absorption of the sample gas. In the amplitude modulation, the intensity of the signal is modulated either electrically or with a mechanical chopper. The mechanical chopper offers a simpler structure, but it is prone to cause noise. Several methods have been developed for the electrical chopping. The easiest way is to modulate the current or the voltage connected to the laser. This method is very simple to realize and it has a sufficient speed for the relatively low modulation frequencies used with the photoacoustic spectroscopy.

The absorption signal from the windows has been solved in several acoustic cells with buffer volumes and tunable air columns [17]. Unfortunately, the nonselective absorption cannot be removed from an amplitude modulated system since it has the same frequency and the same point of origin as the real signal. If the amplitude modulation is changed to a *wavelength modulated system* (WMS), both noise components can be suppressed. Due to their wide absorption peaks, the amplitude of the noise signals remains nearly a constant when the wavelength of the laser is changed. The signal from the narrow absorption peak of the sample gas will drop quickly when the wavelength changes, which makes it possible to calculate the trace gas concentration from the derivative of the signal. [18]

Typical WMS is made with a sinusoidal scanning over the absorption peak, i.e. the wavelength λ of the laser as a function of time t can be written as

$$\lambda(t) = \lambda(0) + B\sin(\omega t), \tag{1}$$

where the $\lambda(0)$ is the wavelength of the absorption peak, B the maximum change in the wavelength and ω the modulation frequency. The photoacoustic signal measured from WMS system is twice the modulation frequency since the wavelength of the laser overlaps the absorption peak twice in each period.

In the ideal, case wide spectrum noise should be almost completely compensated. In reality, the instability of the laser frequency and change of the optical path due the thermal expansion will produce fringe signals. The use of different modulating waveforms can increase signal-to-noise ratio further. Measurements of carbon dioxide (CO_2) sample gas with a triangular, an absorption profile shaped and a symmetrical quasi-square modulation waveform are depicted in Fig. 4 gave an increase of 12 %, 42 % and 57 % respectively in the SNR in comparison to sinusoidal modulation. [18]

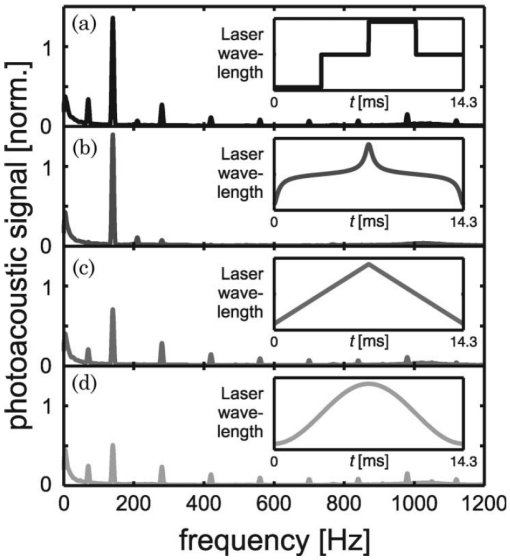

Figure 4: PA signal spectra with a (a) quasi-square (b) shaped (c) triangular and (d) sinusoidal modulating wave. [18]

2.1.3 Absorption of heat energy

When the infrared radiation is absorbed by the sample gas, heat is generated in the sample cell. At each moment, the amount of released heat energy in the system equals $\delta Q(dt)$. In order to measure the amount of absorbed radiation, the relation between the optical power and the absorbed heat energy must be known.

The infrared laser is modulated periodically either with amplitude or wavelength modulation. Consequently, the sample gas absorbs heat energy periodically creating a modulated heat source inside the sample cell. If the sample cell is closed, i.e. we are

not measuring flowing gas, the temperature of the sample gas will increase until the heat conduction through the walls equals the heat energy absorbed by the sample. Usually, the walls are good heat conductors and thus the heat conduction in the sample gas limits the temperature of the system. When the size of the sample cell is decreased significantly, the heat conduction of the walls can also limit the maximum temperature of the cavity.

The absorbed heat energy can be calculated from the Beer-Lambert law for absorbance relating the absorption of the infrared radiation to the optical path length l, the absorption coefficient α_{x} and the partial pressure of the absorbing gas p_{x}. Thus the absorbed heat energy as a function of optical power P_0 is

$$\frac{\delta Q}{dt} = \alpha_{\mathrm{x}} p_{\mathrm{x}} l P_0 [1 - cos(\omega t)] - G(T(t) - T_0), \tag{2}$$

where G is the total thermal conductivity of the sample gas, ω the modulation frequency, T_0 the initial temperature of the sample gas and $T(t)$ the temperature inside the cell at moment t. If the heat conductance of the walls is small, an additional term describing thermal conduction from the walls to the surrounding air must to added to the Eq. 2. The first term describes the modulated infrared source. In real measurements, a part of the incident light can reflect from the cell, in which case an additional term $(1 - R)$ describing reflectivity R have to be added to the equation. If the cell is long, the optical power of the beam will decrease notably while the beam propagates and the absorption coefficient must be changed from the linear $(\alpha_{\mathrm{x}} p_x l)$ to exponential $(1 - \exp(-\alpha_{\mathrm{x}} p_{\mathrm{x}} l))$. Usually, the length of the sample cell is small when the cantilevers are used and the linear approximation is sufficient. [19]

Usually, the optical power is low and the shape and dimensions of the walls do not change notably due to the heat expansion or the pressure inside the cell. Since the total volume of the cavity remains the same, the heat energy transfer process can be approximated as an isochoric process. The change of the heat energy δQ in the Eq. 2 can be replaced with $C_{\mathrm{V}} dT$, where C_{V} is the total heat capacity of the gas, forming a first order differential equation. Using the steady-sate result, the transfer function between the optical power and the heat energy can be written as

$$\delta Q(t) = \frac{\alpha_{\mathrm{x}} p_{\mathrm{x}} l P_0 \tau_1}{\sqrt{1 + (\omega \tau_1)^2}} \cos(\omega t + \phi), \tag{3}$$

where $\tau_1 = C_{\mathrm{V}}/G$ is the time constant due to the heating of gas and ϕ the phase difference between the heating and the modulated optical power. The gas can only warm up at finite speed which limits the measurements at high frequencies that would suite better for the membrane microphones and quartz tuning forks presented in Chapter 2.3. [19]

2.1.4 Relaxation of the excited states

Molecules excited to the higher state by light generate heat when they are relaxed back to the ground state through non-radiative paths. Mechanisms governing the

relaxations through each pathway cannot be easily estimated but their effects can be approximated as a single lowpass filter with transfer function

$$H(\omega) = \frac{1}{\sqrt{1 + (\omega\tau_{\text{rel}})^2}}. \tag{4}$$

The relaxation time τ_{rel} is usually fast, less than 1 ms and therefore it will affect the system response only when the modulation frequencies are greater than $1/\tau_{\text{rel}}$. The modulation frequencies used with microfabricated cantilevers are usually less than 1 kHz and therefore this effect has only a minor effect on the sensitivity of the photoacoustic system. On the other hand, the signal is greatly dampened when condenser microphones and especially quartz tuning forks are used since with the modulation frequencies of tens of kilohertzs. [19]

2.2 Sample cell design

Typical sample cells in photoacoustic spectroscopy are small cylinders where the infrared radiation is focused. The radius of the cavity is limited by the size of the infrared beam since the beam should not hit the walls. The length of the sample cell is usually wanted to be as small as possible in order to reduce the amount of sample gas needed, which reduces the size of the whole system. On the other hand, longer absorption length would lead to a larger signal and better SNR. Various cell types including acoustically resonant photoacoustic, multipass and intracavity cells has been developed to fulfill these requirements. The sample cell design also affects the signal generation by defining the heat conduction out of the cell. Therefore the first part of this chapter is dedicated to the heat conduction effects in the sample cell. The second part presents various structures used to enhance the signal.

2.2.1 Gas heating and thermal diffusion

The design of the photoacoustic cell affects the time constant τ_1 since it is inversely proportional to the thermal conductivity from the sample gas to the walls. When a long cylinder is used, the steady-state time constant τ_1 can be approximated as

$$\tau_1 \approx \frac{\rho_{\text{gas}} c_{\text{V}} r^2}{5.78G}, \tag{5}$$

where ρ_{gas} is the density of the gas, r is the radius of the cavity and G is the thermal conductivity of the gas. This model has been shown to give adequate approximation for the time constant. [19]

If the heat conduction of the walls is high, acoustic waves are not formed near the wall surface because the heat energy absorbed by the gas molecules is directly transported away. As a consequence of this energy loss, the photoacoustic signal is decreased. The thermal diffusion can be approximated as

$$W(r) = 1 - \frac{\mu}{r}\left[1 - \exp\left(-\frac{2r}{\mu}\right)\right], \tag{6}$$

where μ is the thermal diffusion distance from the surface to a point where $(1/e)$ part of heat is conducted to the wall given by

$$\mu = \sqrt{\frac{2G}{\omega \rho c_{\mathrm{p}}}}, \tag{7}$$

where c_{p} is the specific heat capacity of the sample gas. [20]

2.2.2 Mode of operation

Resonant and nonresonant mode of operation describe if the modulation frequency is equal or lower than the lowest resonance frequency of the cavity. In the nonresonant mode, the cavity is much smaller than the acoustic wavelength and standing wave patterns cannot be formed. In a closed resonator, the pressure will vibrate with the modulating frequency whereas in open cell pressure variations will push the gas out. In the resonant mode of operation, the modulation frequency of the source is one of the resonant frequencies of the cavity. Amplitude of the pressure wave at the modulating frequency will be amplified proportional to the quality factor Q, which is relation between the resonant frequency and its bandwidth. All other resonant frequencies will be amplified inversely proportional to the difference between the squared resonant frequency and the squared modulating frequency. With a high Q value and a large separation between adjacent resonance frequencies, only the modulating frequency will be amplified. [11]

When a PAS system is used in a resonant mode of operation, relatively high modulation frequencies are recommended (1... 5 kHz) to suppress the effects of 1/f dependent noise caused by the intrinsic noise of the microphone, amplifier noise and external acoustic noise. Higher frequencies have a shorter cavity length, which means the resonant frequency should be selected as a compromise between a short cavity length and long absorption length. Usually smaller length is preferred because smaller volume leads to a shorter response time and more compact size. [21]

2.2.3 Resonant cavities

Acoustically resonant photoacoustic system is made by fitting the dimensions of a photoacoustic cavity according to the acoustic wavelength. Mostly used resonators are Helmholtz resonators, one dimensional cylindrical resonators and cavity resonators. A set of fundamental resonators is displayed in Fig. 5 featuring a simple pipe, a pipe with buffers and a Helmholtz resonator. Additional buffers connected to the pipe with different cross-section can prevent noise from coupling to the system. The Helmholtz resonator is a combination of two larger cavities and a smaller neck between them, which works as a mechanical resonator. The gas in the cavity works as a spring that moves gas mass in the neck. The resonance frequency of the Helmholtz resonator depends on the speed of sound, the cross-section of the neck, the volume of the cavity and the length of the neck, whereas amplification depends on the viscous and thermal losses on the walls and radiation losses through the opening. Typical amplification for Helmholtz resonator is less than 10. [11]

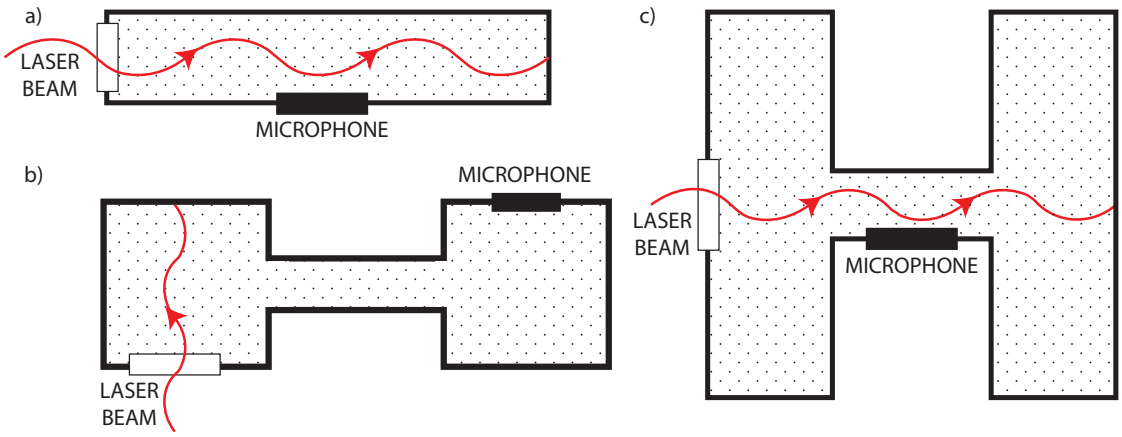

Figure 5: (a) A pipe resonator (b) Helmholtz resonator (c) A buffered resonator.

A cavity with short perpendicular dimensions compared with propagating acoustic wave forms a one-dimensional resonator. Excited sound waves will form standing acoustic waves when the propagating wave reflects from the ends of the cavity and if the phase difference of the waves is a multiple of 2π they will be amplified. The phase difference depends on not only from the acoustic path length but also from the reflection at the ends of the pipe. A pressure antinode will be formed at the closed end such as an air-wall interface since the wall has higher acoustic impedance than air. At the open end, for example an opening to a cavity with a larger diameter, the pressure is at node and the reflected acoustic wave will change its phase by π. If both ends of the pipe are open or closed, the resonance frequency of the pipe can be calculated from

$$f_{\mathrm{n}} = n\frac{v_{\mathrm{sound}}}{4l_{\mathrm{pipe}}}, \tag{8}$$

where n is an even integer, v_{sound} the speed of sound and l_{pipe} length of the pipe. For a pipe with only one end open, the phase shift must be taken into an account and the n must be an odd integer. According to Eq. 8, a 20 cm long pipe with closed ends has the resonance frequency of 857.5 Hz.

In reality, a small change in the open end phase shift is seen. This effect is caused by the cross-section mismatch between the pipe and the cavity. Therefore, a correction term of Δl must be added to the length of the open ended pipe. This term can approximated as $\Delta l = 0.6r$, where r is the radius of the pipe. [11]

The dimensions of *cavity resonators* are the same order of magnitude as the acoustic wavelength, which will lead to several distinct standing waves and resonant frequencies defined by the shape and dimensions of the cell. To match laser beam symmetry, the most used cell shape is a cylinder. For a small microphone, the detected signal is proportional to the pressure amplitude at its location. Unwanted resonance from an external (noise) source can be dampened by placing the microphone at the node of this particular wave. The Q factor for a cylindrical cavity can be made up to 1000 whereas Q factors of 2000...10000 have been realized with a spherical resonator. [11]

2.2.4 Multipass and intracavity cells

A multipass cell is used to increase the photoacoustic signal while using low powered sources. A multipass cell is formed by adding mirrors at both ends of the cavity perpendicular to the laser beam. The laser beam enters through a small hole in one of the mirrors. Fixed mirrors are not usually used since the change of temperature, pressure or measured gas affects the optical path length and thus changes the resonant frequency unless they are compensated by moving the mirrors. One possibility to make a multipass cell is to place concave mirrors outside the cell and close the cell with two highly transmitting windows as shown in Fig. 6. The laser beam reflects between two mirrors until it leaves through the hole or the over edges of the mirrors. Even though power and absorption length are increased, adding a second window also increases the background noise and absorption of the beam. [22]

One of the most used configurations is based on an off-axis resonator (Herriott resonator). It combines a relatively simple construction with a long path length in a small volume. A Herriott resonator has two spherical mirrors illuminated at a off-axis point. Depending on the ratio between the focal length and the distance between the mirrors, a closed path with multiple reflections can be formed. A closed ray path in a focal length spaced system with five reflections is shown in Fig. 6. The absorption length can be increased to a point where window losses and interference fringes equal the signal. The multipass cell can make the whole system smaller without reducing the SNR, which is important in portable and airborne applications. If the identical mirrors are replaced with an astigmatic off-axis resonator, i.e. mirrors having a different radius of curvature, the reflecting beam will fill larger part of the cell. This method is more vulnerable to manufacturing errors, but they can be partially compensated by rotating mirrors about their optical axis. [23, 24]

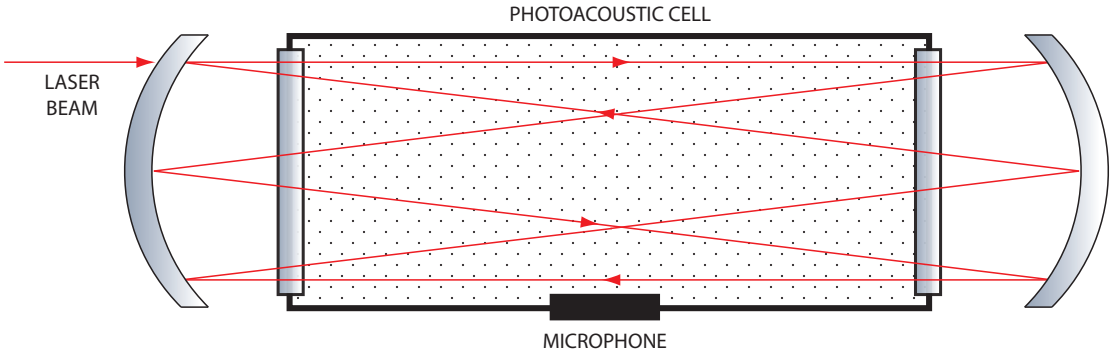

Figure 6: A multipass photoacoustic cell with a Herriott resonator.

Intracavity systems are used to reduce the size and the weight of the system. The sample cell is placed within the laser cavity removing the need for output power coupling for anything else but power monitoring. The laser cavity is ended with two highly reflecting mirrors and the light beam passes the gain material several times. Due to the high reflectance of the mirrors, the optical power of the light beam reflecting inside the laser cavity is usually several order of magnitude higher

than the output power of the laser. The intracavity laser power can be increased up to 100 W in comparison to the 10 mW output power of a diode laser. The power is only limited by the saturation of the gain material. The resonant standing wave amplification enables high frequency operation, which reduces the effects of the 1/f noise. Depending on the structure of the laser, the beam can be modulated for example with a mechanical chopper or by modulating the discharge current in gas lasers. Concentrations of 6 parts per trillion by volume of C_2H_4 in purified air has been measured with an intracavity photoacoustic system. [25, 26]

2.3 Acoustic sensors

The acoustically resonant photoacoustic cell and the multipass and intracavity cells have made it possible to have very high Q values and high intensity radiation in the sample cell. Modern membrane based electric and condenser microphones have reached their theoretical limit and more sophisticated methods are needed in order to measure even lower concentrations and smaller volumes. Quartz tuning forks and optically measured micromachined cantilevers have shown superior sensitivity and dynamic range compared with these traditional microphones and have replaced them in the most sensitive measurements.

2.3.1 Membrane microphones

A typical membrane microphone is based on the change of the capacitance due to the movement of the flexible metal coated membrane. External pressure variations move the membrane and the amplitude of the movement determines the sensitivity of the microphone. The capacitor is formed between a metal coated membrane and a fixed metal electrode as shown in Fig. 7. The capacitance of the microphone depends directly on the dielectric constant of the material inside the microphone and the common area of the electrodes divided by the average distance between them. The dielectric material in condenser microphones is air and the properties of a microphone are determined by the dimensions of the electrodes. The polarizable material in electret microphones has usually larger relative permittivity than air, which makes them more sensitive than condenser microphones.

Most common membrane microphones are condenser and electret microphones. A condenser microphone requires an external bias voltage whereas electret microphones have the permanently electrically polarized sheet of materials that produce the bias voltage. A common property for both membrane microphones is high output impedance at low frequencies. In order to obtain a good signal level, either a high impedance amplifier or high modulation frequencies must be used. The sensitivity of the first method is limited by the input noise of the amplifier and the second by relaxation processes and heat transfer through the walls. [19]

The capacitance C of a membrane microphone as a function of permittivity ϵ, common area of the electrodes A and distance between the electrodes d is

$$C = \epsilon \frac{A}{d} \tag{9}$$

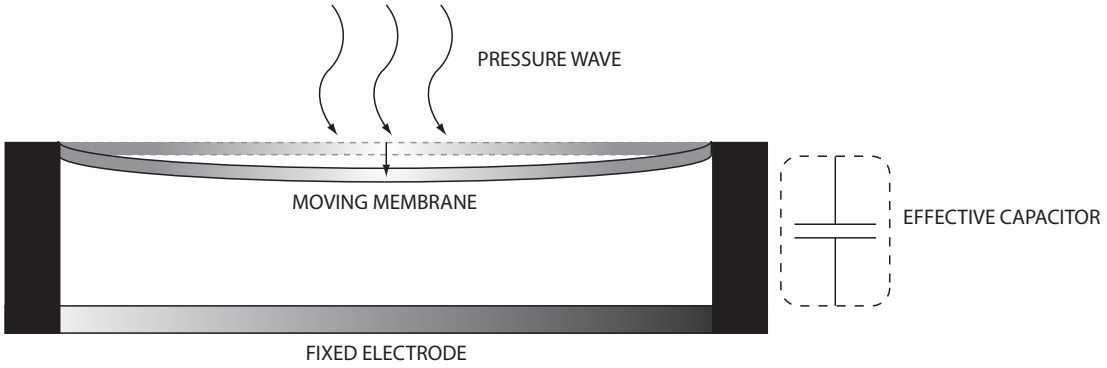

Figure 7: A condenser microphone.

and the change of capacitance ΔC as the distance changes by Δd

$$\Delta C = -\epsilon \frac{A}{d^2} \Delta d. \tag{10}$$

In order to increase the sensitivity of the microphone, the common area should as large as possible and the distance as small as possible. Reducing the distance is usually a more effective method since the change in capacitance is proportional to $\Delta d/d^2$ and only directly proportional to A. The size of the electrodes is usually limited by the application. In addition, large electrodes would lead to a large change in the volume of the microphone. The air inside the microphone must be compressed or removed through small openings in the structure. The compressing air acts as a gas spring, which reduces the sensitivity of the membrane microphones. Decreasing the initial distance between the electrodes would increase the sensitivity, but it would also increase the spring constant since the relative change of volume will be larger for the equal displacement of the membrane. [19]

The sensitivity can also be increased with a more flexible membrane. This can be achieved by making the membrane thinner or by changing its material. In addition to the sensitivity, this method will increase the nonlinearity of the microphone since a more flexible membrane is more susceptible to radial stretching. It will also have to tolerate larger tensions or the membrane can be irreversibly damaged. Usually, these effects reduce the dynamic range since the maximum applied pressures must be restricted in order to protect the membrane. [19]

In order to increase the sensitivity of a membrane microphone, the signal is increased with resonant cavities and noise is decreased with buffer volumes. The disadvantage of these methods is the large size of the system, since the standing wave condition of the resonant cell dictates the minimum size of the cavity and the buffer cells. The response of commercial microphones is spectrally wide and flat making the system vulnerable to external noise. On the other hand, the same membrane microphone can be used with various acoustic cavities having different resonant frequencies and modulating frequencies. The advantages of the membrane microphones compared with the tuning forks and the cantilever microphones are their wide availability and easy measurement.

2.3.2 Quartz tuning forks

Quartz enhanced photoacoustic spectroscopy (QEPAS) is based on the commonly used quartz tuning forks. QEPAS systems need very small amount of the sample gas, only a few cubic centimeters, and they are very resistant to the environmental acoustic noise. The quartz tuning fork (QTF) does not need a large acoustically resonant cavity for high sensitivity since the tuning fork itself gathers the acoustic energy. The quality factor Q of a QTF can be over 10,000 at atmospheric pressure, which would coincide a very good cavity resonator. A suitable QTF microphone for photoacoustic spectroscopy is a quartz tuning fork with approximately 32.76 kHz resonance frequency used in electronic clocks. Since the prongs are usually about 1 mm away from each other, the low frequency acoustic noise will bend the prongs in the same direction and no signal will be detected. [27]

Tuning forks are based on the piezoelectric effect. Deformation of the prongs generates electric charge that can be detected with a transimpedance amplifier and a network signal analyzer. To efficiently excite tuning forks, the optical beam must be directed through the gap between prongs as shown in Fig. 8. Quartz tuning forks are usually used with the wavelength modulation. As described earlier in Chapter 2.1, WMS can be used to suppress the background signal from wide spectrum sources such as tuning fork electrodes and gas cell elements. [28]

A QTF detector can be combined with an acoustic microresonator in order to increase the signal. These approximately centimeter long resonators can be easily added without a large increase in the size of the system. The microresonator can be installed outside the tuning fork, which makes it possible to use a larger infrared beam and thus larger incident power. The highest reported normalized noise equivalent absorption coefficient with H_2O is 1.9×10^{-9} W/$\sqrt{\text{Hz}}$. [29]

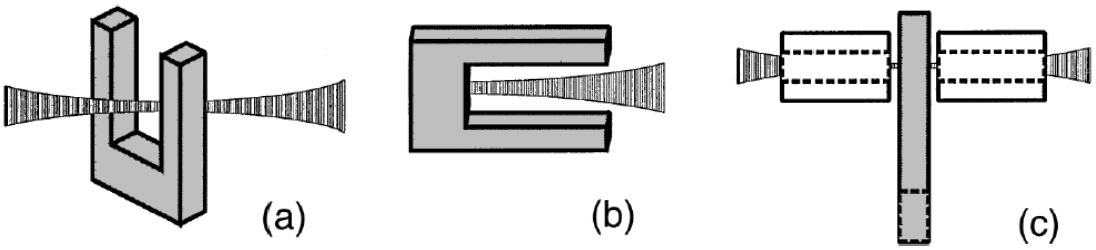

Figure 8: Excitation of a quartz tuning fork with a laser beam (a) perpendicular to the TF plane (b) in the TF plane (c) in an acoustic resonator. [27]

The advantages of QTFs are their good Q value, wide availability and high resonant frequency. A high Q value ensures high sensitivity and a very sharp resonance peak. Since the peak can be only a few Hz wide, the low frequency external noise cannot couple to the resonator. High resonance frequency ensures that the ambient noise having 1/f dependence is very low at the operating frequency. External acoustic resonators can be used to further increase the Q value. The weakness of QTF systems is their relatively long response time.

2.3.3 Micromachined cantilevers

Micromachined cantilever based photoacoustic spectroscopy systems have shown the highest sensitivity to date. The sensitivity of a micromachined cantilever can be over two order of magnitudes higher than the sensitivity of the membrane microphones and one order of magnitude higher than the sensitivity of a QTF system. The highest reported normalized noise equivalent absorption coefficient (NNEA) at atmospheric pressure for carbon oxide is 1.7×10^{-10} W/$\sqrt{\text{Hz}}$ [30]. In addition to the good sensitivity, cantilevers show a very broad frequency response up to the first fundamental flexural frequency, which makes it possible to use them in Fourier transform infrared measurements. Multiple sources with different modulating frequencies can also be used simultaneously due to the flat frequency response. [31]

Micromachined cantilevers are fabricated on a silicon wafer as shown in Fig 9. A small door-like structure is released from three sides enabling the cantilever to bend in one dimension due to a pressure difference. The cantilever is connected from one side to a thick frame and is separated from the other sides with only a few μm wide gap. The sizes of the cantilevers depend on the particular application. In atomic force microscopes, the area of the cantilevers can be a few thousand μm^2 whereas in photoacoustic spectroscopy the cantilever area is a few mm^2.

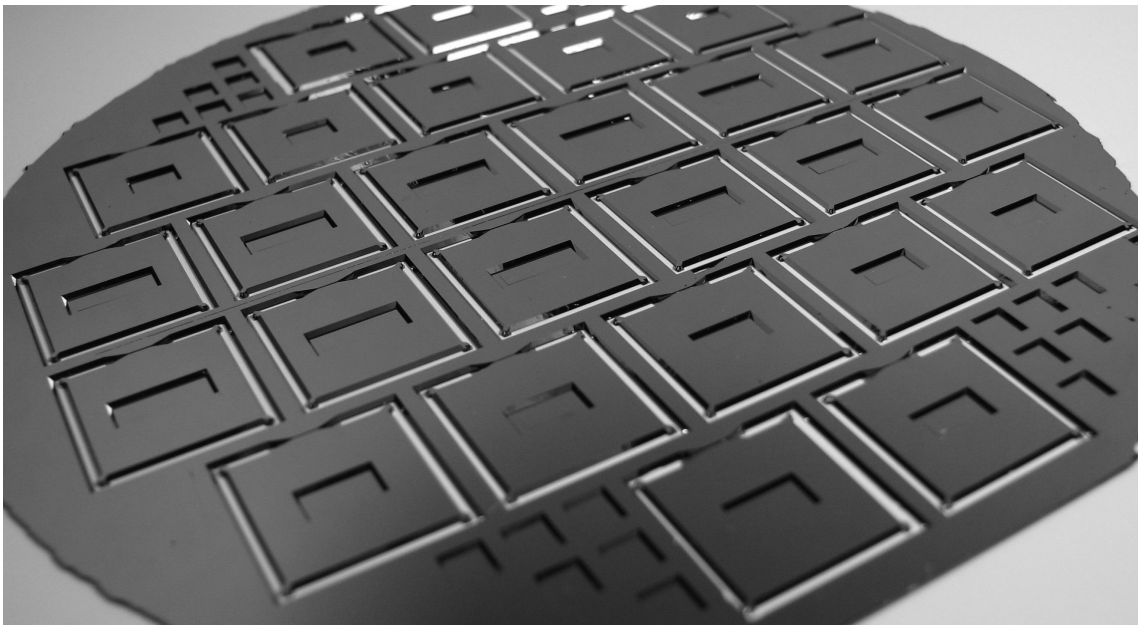

Figure 9: Micromachined cantilevers in a silicon wafer. Courtesy of Päivi Sievilä.

Due to the high sensitivity of a microfabricated cantilever, a resonant cavity is not needed and the size of the photoacoustic system can be kept relatively small. The disadvantages are the challenges in optical measurement and sensitivity to ambient noise. The displacement of the cantilever is usually measured with a Michelson interferometer in order to avoid dampening and electrical noise disrupting the condenser microphones. The cantilevers can be coated with gold in order to increase the reflectivity even though uncoated cantilevers can also be used. In addition to phase

change based interferometric techniques, the displacement of the cantilever can be detected with optical beam deflection techniques. Deflection techniques are based on the change of the reflected power. The pressure wave stirs a reflecting surface at the modulation frequency, which varies the power measured with an optical detector when part of the light is reflected past the detector. Unfortunately, deflection measurements are not as sensitive as the interferometric measurements. [20]

The Michelson interferometer depicted in Fig. 10 consists of a light source, a beam splitter oriented 45 degrees to the beam, reference mirror, the cantilever and one or two detectors. Beam splitter divides light from the source towards the reference mirror and the cantilever. Beams reflected back combine in the beam splitter, where half of the power is directed towards the detector and other half back to the laser and is lost unless a second detector is used. The beam directed towards the detector produces interference fringes on the detector. Depending on the path difference between the branches, light and dark stripes will be seen on the detector. Thus the displacement measurements can be replaced with optical phase measurements. Resolution of 10 pm has been achieved with special Michelson interferometer with a 633 nm HeNe-laser. [32]

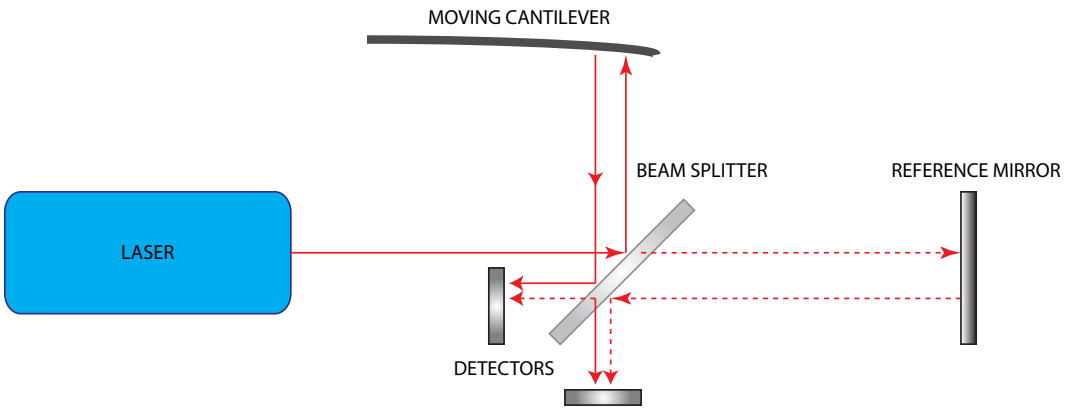

Figure 10: Michelson interferometer.

The optical phase difference can be also measured without a reference mirror when the frame of the cantilever is used as the reference. One differential setup is based on the polarization of the light. A Wollaston prism can be used to separate the light into two orthogonal components. Due to the difference in the refractive index of the Wollaston prism for orthogonal polarizations, the transmitted light beams have a small deviation between them. When one of the beams is aimed at the cantilever and the other one at the frame, a phase change will be created between the beams as the cantilever moves. When the optical beams are recombined with another Wollaston prism, the phase change can be calculated from the measured interference pattern. [33]

2.3.4 Optical fiber based microphones

Another way to measure the vibrations of the cantilever is to place two optical fibers on both sides of a thin cantilever. Optical power coupled to the first fiber is transmitted in free air over the cantilever to the second fiber that is connected to a detector. The movement of the cantilever can be detected by the change of power in the amplifier. This method can be used to build small optical detectors, but the achieved sensitivity is usually even lower than with the membrane microphones. [34]

Optical fiber can also be used as a Michelson interferometer. The fiber is clued to an elastic sample cell wall. Pressure waves can move the wall and thus lengthen the fiber changing the optical path length. This method requires two equally long optical fibers. The first fiber is used as a reference and the second is wound around the photoacoustic cell. A laser beam is first split between these two fibers and after passing the fibers they are again combined to a photodetector. As two beams interfere, the power measured with the detector varies. Placing the microphone outside the cell makes the system simpler but the sensitivity is lower compared with a cantilever microphone. Another problem arises from the optical fibers since even a small deviation in the length can reduce the sensitivity. [35]

If the optical fiber is wound around the sample cell, a Sagnac interferometer depicted in Fig. 11 can be formed. Optical fiber is connected to a delay coil outside the sample cell. A light beam from a laser is directed to both ends of the fiber. After passing the fiber in the opposite directions, light beams are coupled to a detector. The modulated infrared light increases the volume of the photoacoustic cell and thus lengthens the fiber. The light is modulated such way that they experience different delay due to the photoacoustic effect and thus a changing interference pattern is formed at the detector. The length of the delay coil must be equal to the distance light travels in the fiber during a half of the modulation phase. Even though the theoretical sensitivity of the Sagnac interferometer is lower than the sensitivity of the Michelson interferometer it has a few advantages. Sagnac interferometer does not need two equal length fibers and a source of high coherence and it has better stability enabling longer averaging. [35]

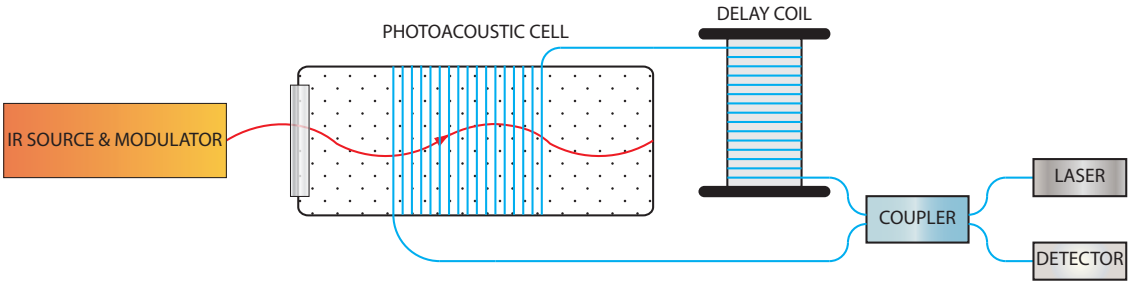

Figure 11: Sagnac interferometer.

2.4 Fourier transform infrared PAS

Fourier transform infrared spectroscopy (FTIR PAS) is used to separate multiple cross correlating components in one measurement. A wideband source is used with an interferometer to excite the sample gas. The exciting wavelength is selected with a setup similar to the Michelson interferometer shown in Fig. 10. Only the wavelengths, for which the phase change due to the optical path length difference is a multiple of 2π, will be reflected from the beam splitter. When the detectors are replaced with a photoacoustic cell, the wavelength exciting the sample gas changes as one of the mirrors is moved. The microphone forms an interferogram, which is used to obtain the spectrum of the sample. [20]

Since the photoacoustic spectroscopy is based on the absorption of the IR radiation, the sample does not have to transmit light and the sampling range can be very wide. The thermal waves created by the absorption of the IR radiation in the sample decay rapidly when they propagate in the sample. This decay defines the layer thickness from which the spectrum is obtained. The modulation frequency determines how far into the sample the thermal waves can propagate. Lower modulation frequencies will measure the spectrum from deeper parts of the sample but they can also saturate the strong absorption bands as the absorption length increases. [36]

FTIR spectroscopy offers a wide dynamic range with good selectivity making it possible to identify components even if the concentrations vary greatly. The low sensitivity of condenser microphones limited the usability of FTIR PAS until high sensitivity photoacoustic detectors such as optically measured micromachined cantilevers were developed. FTIR PAS has a higher response than transmission spectroscopy, which makes it possible to use small sample volumes. In addition FTIR PAS is more immune to the baseline distortions and has a constant response to all frequencies. [20]

The main problem with FTIR PAS is a large decrease in the system response when compared with direct photoacoustic spectroscopy. FTIR PAS can only be used to measure narrow bandwidth in resonant mode. In order to have a wider frequency response, the photoacoustic system must be operated at the nonresonant mode, which leads to a smaller signal. In addition, the interferometer has low throughput further limiting the signal. The best reported sensitivity with gaseous sample FTIR PAS is 0.1 ppm. [8]

3 Signal and noise in PAS system

The signal generation in a photoacoustic system depends on the properties of the sample gas, the sample cell and the microphone. The previous chapter presented how the incident radiation generates a photoacoustic signal in a uniform sample when a nonresonant mode of operation is used. In this chapter, transfer function for the photoacoustic signal is derived when a micromachined cantilever is used as an acoustic detector. This chapter also presents how the sample gas affects the cantilever response. This effect can be taken into an account by replacing the mass and spring constant of the cantilever with effective mass and effective spring constant. The second part of this chapter concentrates on the noise sources disturbing the photoacoustic systems and presents various ways which can be used to reduce noise.

3.1 Cantilever response

The frequency response of the micromachined cantilever depends on the amplitude of the pressure wave generated by heating of the sample gas and the cantilever. The cantilever can be described as a harmonic oscillator. Naturally, it defines the shape and material dependent spectrum of mechanical resonances. Even so, the cantilever is usually used in nonresonant mode due to the better noise performance.

A typical size for the cantilever depicted in Fig. 12 is approximately 10 mm^2 where the length $l_\text{c} = 5$ mm, the width $w = 2$ mm and the thickness t = 9.5 μm. Cantilevers can be approximated as a uniform clamped-free beam for which the first flexural resonance frequency depends on the beam diameter in the direction of oscillation, Young's modulus E and density of silicon ρ_Si and is given by [37]

$$f_0 = 0.162 \frac{t}{l_\text{c}^2} \sqrt{\frac{E}{\rho_\text{Si}}}. \tag{11}$$

For these given values, the resonance frequency $f_0 = 534$ Hz and the corresponding wavelength is over 500 m. The modulation frequencies with cantilevers are usually well below the first resonant frequency, which makes it possible to approximate the cantilever as a spring with a single point mass. High frequency operation would require a full three-dimensional structure model, which is omitted from this thesis. For a harmonic oscillator pressed equally from every point, the spring constant is

$$k_0 = \frac{2}{3} E w \left(\frac{t}{l_\text{c}} \right)^3. \tag{12}$$

The micromachined cantilevers have a very low spring constant in vacuum due to a very low t/l_c ratio. The resonant frequency ω_0 is related to the spring constant k_0 through the effective mass, i.e. $\omega_0 = \sqrt{k_0/m_\text{eff}}$. The effective mass for a cantilever in vacuum is 0.647 times the mass of the cantilever. In real applications, the mass increases due to the sample gas, though. Motion of the free end of the cantilever can be described by a linear differential equation

$$m\ddot{x} + D\dot{x} + kx = m\left(\ddot{x} + \frac{D}{m}\dot{x} + \omega_0^2 x \right) = m\frac{F_\text{ext}(t)}{m}, \tag{13}$$

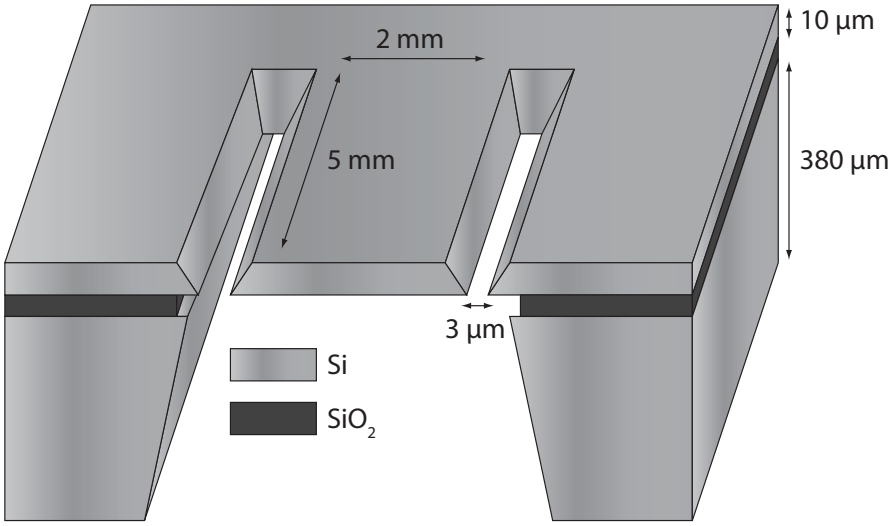

Figure 12: Cross-cut view of a cantilever (not in scale). Redrawn from [37]

where m is the mass of the cantilever, D the damping constant, k the effective spring constant and $F_{\text{ext}}(t)$ is the external force affecting the cantilever caused by the thermal expansion of the sample gas. [19]

This equation can be solved for a sinusoidal external force $F_{\text{ext}}(t) = F_0 \cos(\omega t)$, where F_0 and ω are the amplitude and the angular frequency of the force. The solution for the Eq. 13 is in form of an exponentially decaying transient part and a vibrating steady state part. We are only interested in the steady state and thus the solution for the displacement is given as $x(t) = A\cos(\omega t - \phi)$, where A is the amplitude of the oscillations and ϕ is the phase difference between the exciting signal and the movement of the cantilever. We can now solve the amplitude of the oscillations by estimating

$$\begin{aligned}
\frac{F_0}{m}\cos(\omega t) &= -\omega^2 A\cos(\omega t - \phi) - \frac{D}{m}\omega A\sin(\omega t - \phi) + \omega_0^2 A\cos(\omega t - \phi) \\
&= A\left(\omega_0^2 - \omega^2\right)\cos(\omega t - \phi) - \frac{D}{m}\omega A\sin(\omega t - \phi) \\
&= \left(\omega_0^2 - \omega^2\right) A\left[\cos(\omega t)\cos(\phi) + \sin(\omega t)\sin(\phi)\right] - \\
&\quad \frac{D}{m}\omega A\left[\sin(\omega t)\cos(\phi) - \cos(\omega t)\sin(\phi)\right] \qquad (14)
\end{aligned}$$

When the terms depending on $\cos(\omega t)$ are grouped on the left side and the terms depending on $\sin(\omega t)$ on the right side, we can see that the Eq. 14 is only satisfied at all times when the coefficients for both functions are zero. The coefficient for the sinusoidal terms is

$$A\left(\omega_0^2 - \omega^2\right)\sin(\phi) - A\frac{D}{m}\omega\cos(\phi) = \left(\omega_0^2 - \omega^2\right)\tan(\phi) - \frac{D}{m}\omega = 0, \qquad (15)$$

from which the phase difference can be solved as

$$\phi = \arctan\left(\frac{D}{m}\frac{\omega}{\omega_0^2 - \omega^2}\right). \qquad (16)$$

The amplitude of the oscillations can be then solved from

$$\left(A\left(\omega_0^2-\omega^2\right)\cos(\phi)+\frac{D}{m}\omega A\sin(\phi)-\frac{F_0}{m}\right)\cos(\omega t)$$
$$=A\left(\frac{\omega_0^2-\omega^2+\omega^2D^2/m^2}{\sqrt{(\omega_0^2-\omega^2)+\omega^2D^2/m^2}}\right)-\frac{F_0}{m}\quad=0 \tag{17}$$

as

$$A(\omega)=\frac{F_0}{m\sqrt{\left(\omega_0^2-\omega^2\right)^2+\omega^2D^2/m^2}} \tag{18}$$

The mechanical vibrations of the cantilever can also be described with a quality factor Q, which in turn describes the ratio of the stored energy to the energy lost in each cycle. It can be expressed by

$$Q=\frac{\omega_0}{\Delta\omega}=\frac{k}{\omega_0 D}. \tag{19}$$

The first term is the ratio between the resonance frequency and the width of the resonance peak, where $\Delta\omega$ is the full width at the half maximum of the resonance peak, i.e. the band where the signal is attenuated less than 3 dB from the maximum value. The Q factor is also related to the decay time $\tau=2Q/\omega_0$, which describes the time taken to dampen the amplitude of oscillations to $\frac{1}{e}$th part. Increasing the Q value will increase the amplification and narrow the bandwidth of the resonance peak, but it will also lengthen the decay time. Typically the Q factor is several hundred in vacuum, one hundred in atmospheric pressure and only a dozen in a gas filled chamber, where gas flow dampens the vibrations of the cantilever. [19, 37]

When the modulation frequency is well below the resonance frequency $\omega \ll \omega_0$, the movement of the oscillator has a wide, flat response, which is proportional to F_0/k. If the damping factor D is small, the Q value is large and the resonance peak is high whereas low Q values lead to a low peak. After the resonance peak, the oscillator response will start to decrease proportionally to $1/\omega^2$. It must be noted that the cantilever will interact with the environment and the real frequency response will have some variations from this model.

3.1.1 Comparison between a cantilever and a membrane

Microfabricated cantilevers were used to replace a membrane microphones due to their smaller gas spring constant. A moving membrane can also be measured optically, which reduces the spring constant since the gas spring is removed. Thin diaphragms can be fabricated with the same process as the cantilevers and they would even require less microfabrication steps since the cantilever has to be patterned. Unfortunately, they are much more rigid structures. The maximum displacement depends on the shape of the membrane. Square membranes have usually better sensitivity, but the displacement cannot be analytically solved. For a circular membrane with radius R, the maximum displacement is given by

$$x_{\max}=\frac{3p(1-\nu^2)R^4}{16Et^3}, \tag{20}$$

where ν is the Poisson ratio relating the strain perpendicular to the load to the strain parallel to the load and p the pressure bending the membrane [38]. The Poisson ratio for silicon depends on the crystal direction but it can be approximated to be 0.3. By setting the radius $R = l_c/2$, we can compare it with similarly sized cantilever. The displacement x of the uniformly loaded cantilever shown in Fig. 13 at the distance y from the base of the cantilever is

$$x = \frac{pw\left(y^4 + 6y^2 l_c^2 - 4y^3 l_c\right)}{24EI} = \frac{p\left(y^4 + 6y^2 l_c^2 - 4y^3 l_c\right)}{2Et^3}, \tag{21}$$

where $I = wt^3/12$ is the moment of inertia for a square beam [39].

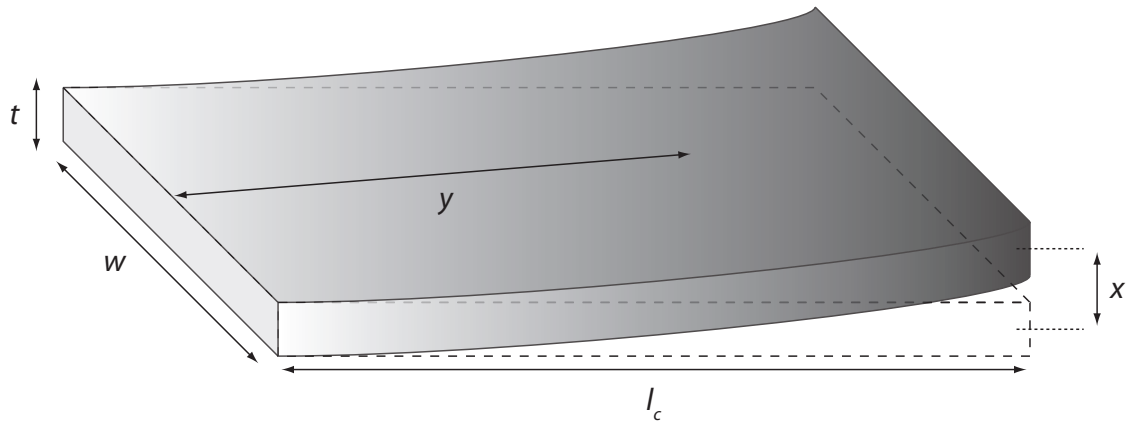

Figure 13: Bending of a cantilever.

Dividing Eq. 20 with Eq. 21 will give us the ratio between the maximum displacements as

$$\frac{(3pl_c^4)\,/\,(2Et^3)}{(2.73pl_c^4)\,/\,(256Et^3)} \approx 140.6. \tag{22}$$

For equally long sensors, the maximum displacement for a cantilever will be over 140 times higher than for a circular membrane.

3.1.2 Effective spring constant

A small change in the volume of the sample cell can be seen when $F_{\text{ext}}(t)$ bends the cantilever. The pressure caused by the external force is distributed to the whole area A_C of the cantilever. The movement of the cantilever due to this pressure can be written as

$$dF = A_C dp = k_0 dx. \tag{23}$$

A lower spring constant leads to higher displacement of the cantilever and therefore the sensitivity of the system is increased. In order to calculate the change of volume dV, we must first solve the average deflection of the cantilever. The average displacement can be calculated from Eq. 21 as

$$x_{\text{avg}} = \frac{p}{2Et^3}\frac{1}{l_c}\int_0^{l_c}\left(y^4 + 6y^2 l_c^2 - 4y^3 l_c\right)dy = \frac{3}{5}\frac{pl_c^4}{Et^3}. \tag{24}$$

The average deflection x_{avg} can be written in terms of maximum deflection as

$$x_{\mathrm{avg}} = \frac{3pl_{\mathrm{c}}^4}{5Et^3} = \frac{2}{5}\frac{3pl_{\mathrm{c}}^4}{2Et^3} = \frac{2}{5}x_{\mathrm{max}}. \tag{25}$$

The bending of the cantilever changes the volume V of the photoacoustic cell by

$$dV = \frac{2}{5}A_C dx. \tag{26}$$

The sample gas in a photoacoustic system can be considered as an ideal gas for which

$$pV = n\left(c_{\mathrm{p}} - c_{\mathrm{V}}\right)T, \tag{27}$$

where n is the number of moles, c_{p} and c_{V} specific heat capacities at constant pressure and constant volume, respectively. According to the first law of thermodynamics, the heat δQ transferred to the system must equal to the change in the internal energy dU and work dW done by the system. These changes can be written as a function of the changes in temperature dT and volume dV as

$$\delta Q = dU + dW = c_{\mathrm{V}} n dT + p dV \tag{28}$$

The change of temperature dT can be obtained by differentiating Eq. 27

$$n\left(c_{\mathrm{p}} - c_{\mathrm{V}}\right)dT = d(pV) = V dp + p dV. \tag{29}$$

Inserting dT from Eq. 29 into Eq. 28 will lead to

$$\delta Q = p dV + \frac{c_{\mathrm{V}} n}{n\left(c_{\mathrm{p}} - c_{\mathrm{V}}\right)}(V dp + p dV) = \left(\frac{c_{\mathrm{p}}}{c_{\mathrm{p}} - c_{\mathrm{V}}} p dV\right) + \left(\frac{c_{\mathrm{V}}}{c_{\mathrm{p}} - c_{\mathrm{V}}} V dp\right). \tag{30}$$

Using the relations for dp and dx in Eq. 23 and the relations for dV and dx in Eq. 26 in Eq. 30 will lead to

$$\frac{(\gamma - 1)\delta Q}{V} = \gamma\frac{p}{V}dV + dp = \gamma\frac{p}{V}\frac{2}{5}A_{\mathrm{C}}dx + \frac{k_0}{A_{\mathrm{C}}}dx. \tag{31}$$

The differential force can be solved by multiplying Eq. 31 with the area of the cantilever

$$dF = \left(k_0 + \gamma\frac{A_{\mathrm{C}}^2 p}{2.5V}\right)dx = \frac{A_{\mathrm{C}}(\gamma - 1)\delta Q}{V} \tag{32}$$

Comparing Eq. 23 with Eq. 32 will give us an equation for the effective spring constant

$$k = k_0 + \gamma\frac{A_{\mathrm{C}}^2 p}{2.5V}. \tag{33}$$

The effective spring constant k is formed from the spring constant of the cantilever and the change of volume caused by the bending of the cantilever. This effect is similar to the gas spring in membrane microphones but due to the more open structure, the gas spring constant is smaller in the cantilever enhanced systems.

Decreasing the area of the cantilever would decrease the gas spring constant quickly, since the spring constant is proportional to the square of the area. [19]

The gas spring constant is inversely proportional to the volume of the sample cell, i.e. the smaller the sample cell is, the larger the effect of the spring constant is. Kauppinen et al. have tested the effect of the sample cell volume on the resonant frequency of the cantilever and their results are shown in Fig. 14 [40]. [19]

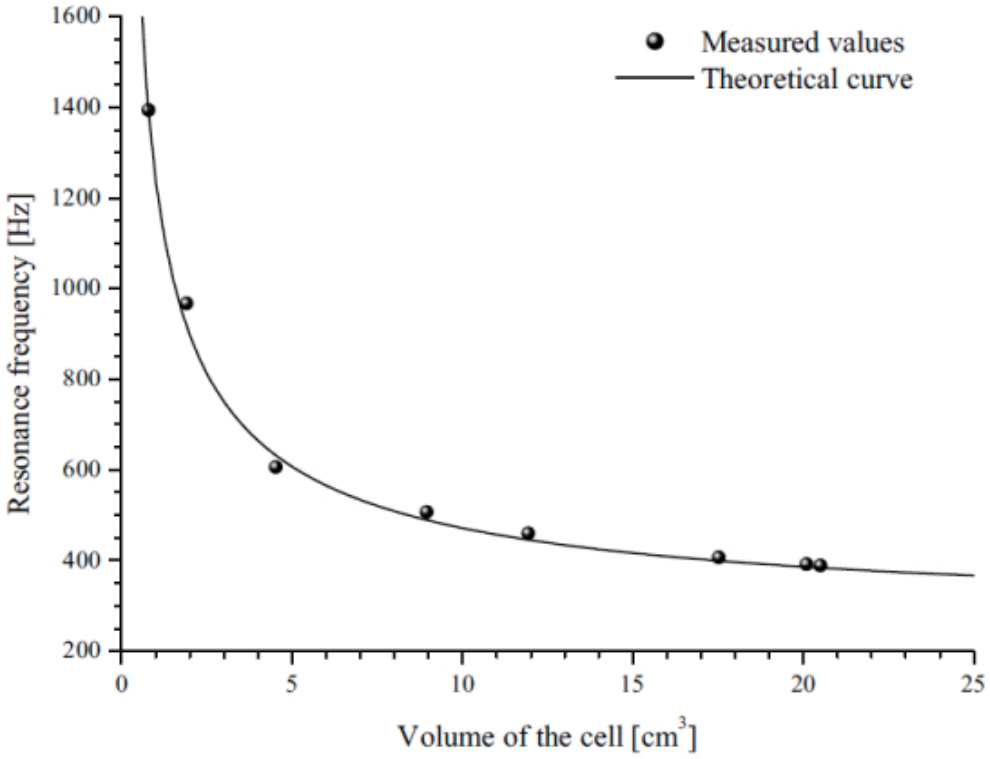

Figure 14: Resonant frequency of a cantilever as a function of the volume of the photoacoustic cell. [40]

The movement of gas affects the effective spring constant. Larger cavities would minimize the effect of the gas spring but they would either decrease the pressure in the measurement system or require more sample gas, which would diminish the advantages of a cantilever enhanced system. Another advantage of a larger sample cell is a smaller thermal diffusion to the walls.

3.1.3 Effective mass

Not only the gas affect the spring constant of the cantilever but also the mass. The effective mass can be calculated from the mass of the cantilever and the mass of the gas the cantilever is pushing. Analytical form for the mass have been approximated as

$$m \approx \frac{2}{3} m_{\mathrm{C}} + \rho_{\mathrm{gas}} \sum_{\mathrm{i,j}} \frac{(0.4 A_{\mathrm{C}})^2}{V_{\mathrm{j,tot}}^2 A_{\mathrm{i,j}}} \left[\frac{V_{\mathrm{i,j}}^2}{3} + V_{\mathrm{i,j}} V_{\mathrm{i,j,end}} + V_{\mathrm{i,j,end}}^2 \right] l_{\mathrm{i,j}}, \tag{34}$$

where m_C is the mass of the cantilever, $V_{j,tot}$ the total volume of j side of the cantilever, $A_{i,j}$, $V_{i,j}$ and $l_{i,j}$ area, volume and length of the chamber prior to the cantilever vibrations moving the gas and $V_{i,j,end}$ is the volume after the movement. [19]

Another model for the effective mass has been given in [41]. The effective mass is approximated as

$$m = 0.647 m_C + V^* \rho_{gas}, \tag{35}$$

where V^* is an effective volume depending from the size and shape of the sample cell and the interferometer cavity.

3.1.4 Gas leakage from the frame gap

Since the cantilever is not used in vacuum, the sample gas will affect the system response. The cantilever is usually used in nonresonant mode, i.e. the modulating frequency ω is lower than ω_0. Due to the long acoustic waves compared with the dimensions of the sample cell excited by low modulation frequencies, we can make a simplifying assumption and evaluate the sample gas as an ideal gas, i.e. pressure p, density ρ_{gas} and temperature T are constant over the whole cell.

A finite gap between the cantilever and the frame makes it possible for the gas to move freely from the sample cell to the interferometer cell. Leaking gas acts as a highpass filter and dampens the variations of the pressure. This filtering effect works through two mechanisms. The pressure difference is equalized by the net particle flow from the sample cell to the interferometer cavity. Warmer gas molecules have higher average speed and thus particles will flow to the colder side. When the heat energy is transferred to the other side, the gas on that side heats up and the pressure difference decreases.

The damping effect due to the gas and heat flow can be derived using the kinetic-molecular model. In the ideal case, all the gas molecules in the same cavity have the same speed that depends from their average translational kinetic energy $3k_B T/2$. The damping effect due to the pressure difference caused by a sinusoidal pressure source can be expressed as a highpass filter

$$H(\omega) = \frac{\omega\tau_2}{\sqrt{1 + (\omega\tau_2)^2}}, \tag{36}$$

where A_g is the area of the gap and the time constant τ_2 is

$$\frac{1}{\tau_2} = \frac{A_g}{2V_{eff}} v_{avg}, \tag{37}$$

where $1/V_{eff} = 1/V + 1/V_0$ is the effective volume and v_{avg} is the average speed of the molecules. The effective volume depends on the sample cell volume V and the interferometer cavity volume V_0. For a high signal, this volume should be as large as possible since the relative change in the number of molecules is small when large cavities are used. Another way to increase the signal would be to decrease the area

of the gap, but this is usually limited by the fabrication process. The average speed can be calculated from

$$v_{\mathrm{avg}} = \sqrt{\frac{3k_{\mathrm{B}}T}{2}\frac{2}{m_{\mathrm{mol}}}}, \tag{38}$$

where k_{B} is the Boltzmann constant and m_{mol} mass of a gas molecule. [19]

Damping caused by the temperature leakage through the gap can be also derived from the kinetic-molecular model. This effect can be approximated with a highpass filter

$$H(\omega) = \frac{\omega\tau_3}{\sqrt{1+(\omega\tau_3)^2}}, \tag{39}$$

where the time constant τ_3 is

$$\frac{1}{\tau_3} = \frac{A_{\mathrm{g}}}{4\sqrt{3}V_{\mathrm{eff}}}\sqrt{\frac{3k_{\mathrm{B}}T}{m}} = \frac{A_{\mathrm{g}}}{4\sqrt{3}V_{\mathrm{eff}}}v_{\mathrm{avg}}, \tag{40}$$

which is similar to Eq. 36. In fact, both mechanisms can be combined as a serial process, which give us effective time constant as a function of speed of sound v_{sound}

$$\frac{1}{\tau_{23}} = \frac{1}{\tau_2} + \frac{1}{\tau_3} = \frac{3}{2}\frac{A_{\mathrm{g}}}{4\sqrt{3}V_{\mathrm{eff}}} = \frac{3A_{\mathrm{g}}}{4\sqrt{\gamma}V_{\mathrm{eff}}}v_{\mathrm{sound}}. \tag{41}$$

Eq. 41 is only valid when the gas flow between the cells is low enough. Speed of sound v_{sound} sets the upper limit for the flow and the flow ceases to depend on pressure and temperature as soon as the limit is reached. [19]

Fortunately, the size of the gap is limiting the sensitivity only at low modulation frequencies. The modeled attenuation of the cantilever displacement due to the gas leakage with varying gap width is shown in Fig. 15. The modeled cantilever was 5 mm long, 1.2 mm wide and 10 μm thick with the effective volume of the photoacoustic and interferometric cells $V_{\mathrm{eff}} = 1.5$ cm^3.

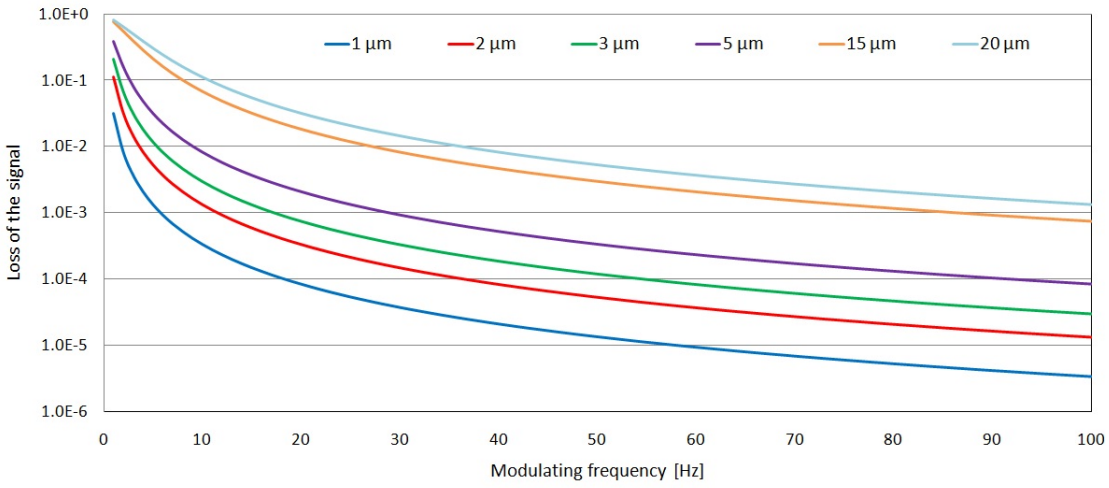

Figure 15: Loss of the signal due to gas leakage with varying width of the gap.

The gas leakage attenuates the displacement of the cantilever at very low frequencies. The attenuation decreases very quickly for narrow gaps, for example one micrometer wide gap attenuates the signal less than 10^{-4} at 20 Hz while the attenuation with 20 μm wide gap is still over 10^{-3} at 100 Hz.

3.1.5 Total system response

We can now combine the gas heating in Eq. 3, the relaxation time in Eq. 4, thermal diffusion through the wall in Eq. 6 with the frequency responses of the cantilever in Eq. 17 and filter due to gas leakage between the cantilever and the frame in Eqs. 36 and 39 for a total system response of

$$A(\omega) = \frac{A_{\mathrm{C}}(\gamma-1)}{V} \frac{\alpha_{\mathrm{x}} p_{\mathrm{x}} l P_0}{m\sqrt{\left(\omega_0^2-\omega^2\right)^2+\left(\omega D/m\right)^2}} W(r,\omega) \\ \frac{\tau_1}{\sqrt{1+(\omega\tau_1)^2}} \frac{\omega\tau_{23}}{\sqrt{1+(\omega\tau_{23})^2}} \frac{1}{\sqrt{1+(\omega\tau_{\mathrm{rel}})^2}}. \tag{42}$$

The total system response is shown in Fig. 16 with all the different components affecting it. At low frequencies, thermal diffusion to the cell walls reduces the pressure wave generated inside the cell and the gas leakage through the gap between the frame and the cantilever reduce the pressure difference bending the cantilever. The sensitivity increases with the modulation frequency until the heating of the sample gas and the relaxation mechanisms do not enough time to follow the modulation. Maximum sensitivity is usually achieved around 10 Hz. Frequency response decreases until the resonant frequency of the cantilever, where small local maximum is seen. At higher frequencies than resonant frequency, the total system response plunges with relaxation mechanisms and the cantilever responses.

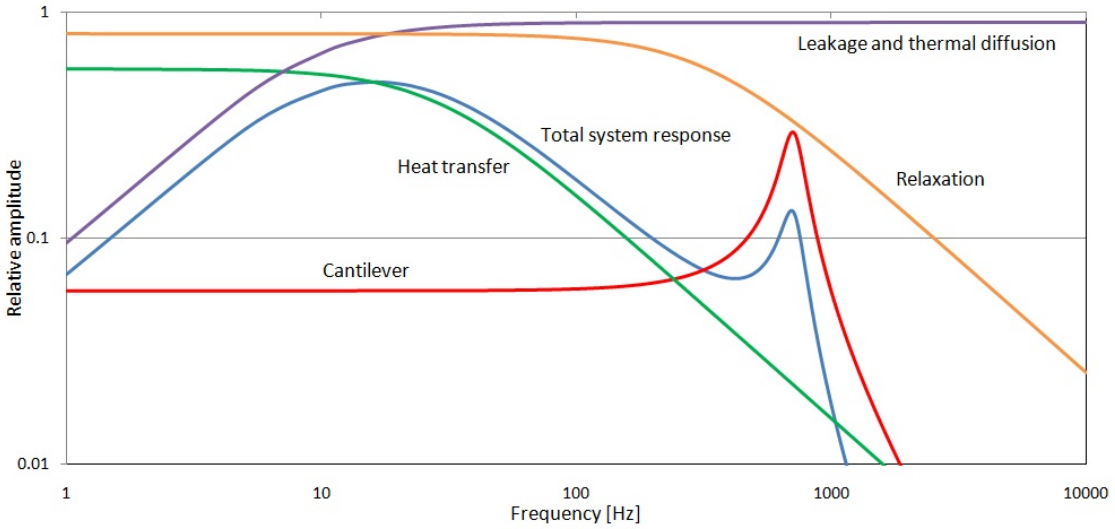

Figure 16: Components affecting the total system response.

3.2 Noise in the photoacoustic system

Even though a PAS system can be used to measure very small concentrations, the sensitivity is always limited by noise. Since the photoacoustic system interacts with the environment and the components of the photoacoustic cell are not ideal, several noise sources will appear in the measurements. A high response from the system can originate either from a real signal or noise so that the source cannot be identified. Therefore reliable measurements require good SNR in addition to good sensitivity. The photoacoustic spectroscopy systems have four main noise components, acceleration, Brownian, acoustic and electrical noise. The infrared source can also excite molecules in the windows and in the sample cell walls, which creates an additional noise component. Only the electrical noise is frequency independent, which means SNR cannot be increased by operating the system at the resonance frequency since noise increases with the signal. Several structures have been developed in order to reduce noise, from which balance chamber, "windowless" structures, acoustic baffles and differential cells are introduced.

3.2.1 Acceleration, acoustical, electrical and background noise

Acceleration noise is caused by coupling of external disturbances to the measurement system. Main sources for acceleration noise is building vibrations and vibrations caused by other machines, for example fans. In the worst case, disturbances have components perpendicular to the cantilever surface, which will bend the cantilever due to inertia and cause unwanted signals. External movement will also affect gas inside the cells, which can be used to compensate acceleration noise. The compensation is made by adding a balance cell shown in Fig. 17 to the sample cell. When the distance of the center of masses is

$$D_{\mathrm{CM}} = \frac{\rho_{\mathrm{Si}}}{\rho_{\mathrm{gas}}} t, \tag{43}$$

where ρ_{Si} is the density of a silicon cantilever, ρ_{gas} the density of the sample gas and t thickness of the cantilever, the pressure caused by the acceleration of the sample gas will be equal to the pressure caused by the movement of the cantilever. [20]

When a balancing chamber is used for compensating acceleration noise, the volume of the photoacoustic cell must be replaced with the effective volume V_{eff} where all three cavities (sample cell, interferometer cavity and balance cell) are taken into an account. Another advantage of the balance chamber is the reduction of the effective spring constant due to the reduced gas spring effect.

Acceleration noise can also be compensated by using differential setup where the same noise is coupled to another cantilever. The photoacoustic effect affects only one of the cantilevers, which leads to noise suppression when two signals are subtracted. The use of mechanical dampeners such as gas springs or gel pads can lead to a significant reduction in the acceleration noise for higher frequencies. Nevertheless, the acceleration noise is usually the dominant noise component below 25 Hz. [20]

The amplitude of the acceleration noise can be evaluated from the known external

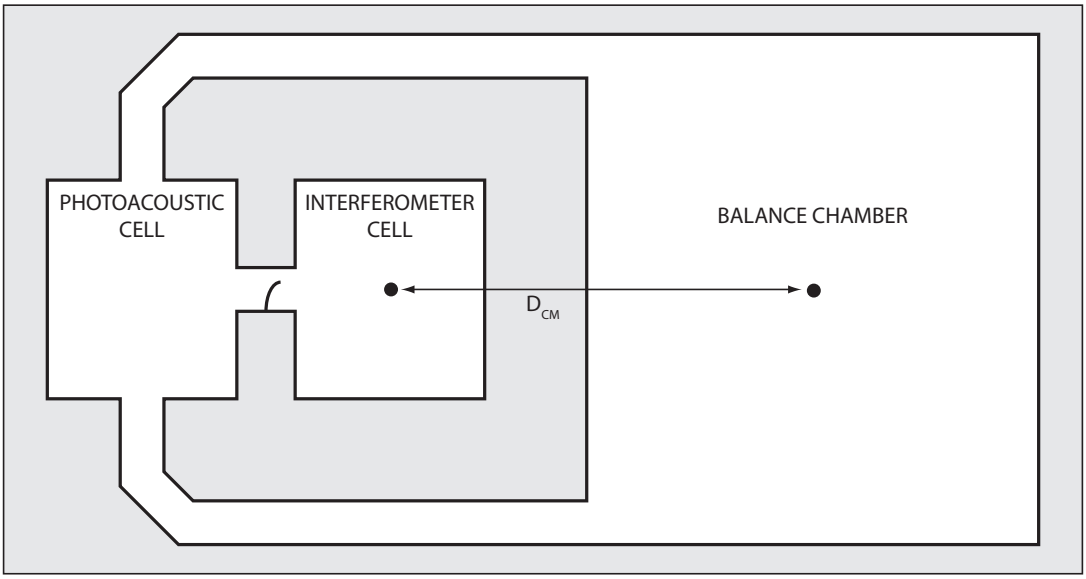

Figure 17: Acceleration noise compensation with a balance chamber. Redrawn from [20]

forces. External vibrations will bend the cantilever with a force

$$\Delta F_{\text{ext}} = m_{\text{C}} \Delta a = \rho_{\text{C}} A_{\text{C}} t \Delta a = k \Delta x, \tag{44}$$

where Δa is the amplitude of the acceleration and Δx the corresponding movement of the cantilever.

Acoustical noise forms when ambient acoustical waves penetrate into the sample cell through gaps in the measurement setup. The sources for the acoustical noise can vary from the speech and humming of fans to creaky hinges. Acoustical noise can be minimized by a careful construction and selection of materials. High frequency mechanical vibrations can generate acoustical waves if some flexible seals, which can vibrate under pressure, are connected to the sample cell. Typical sources for acoustical noise are tubes and valves connected to the sample cell. [20]

Amplitude of acoustical noise can be written as a function of the amplitude of the acoustical noise pressure Δp as

$$\Delta F = A_{\text{C}} \Delta p = k \Delta x. \tag{45}$$

Electrical noise develops from the laser of the interferometer, operational amplifiers and photodetectors. The main sources of disturbance are the shot noise of the laser, the dark current of the photodetectors and the input noise of the amplifiers. Input noise can be reduced by using low noise operational amplifiers. Even though every device has its own frequency characteristics, electrical noise is usually trivial in comparison with the other noise sources outside power network frequencies. Even if the measurement setup itself it nearly immune to the electrical noise, badly designed cabling can couple electrical noise to the measurements. Therefore shielded cables

should be used when possible, especially if low signal measurements are made or if high current cables are nearby. [41]

Background noise is produced on the sample cell walls and window and by dust particles. The heating of the walls and the window by the absorption of infrared radiation generates temperature variations in the gas close to the surfaces creating an acoustic wave in the gas. Background noise from the walls can be minimized by making them very reflective by coating the walls with gold and polishing. Adding dust filters in the gas inlets decreases the number of dust particles efficiently. [20]

3.2.2 Brownian noise

Brownian noise is an intrinsic limit for the noise amplitude. When all the other external noise sources have been minimized, collisions between molecules and the cantilever produce thermal fluctuations, which act as a force on the cantilever. Brownian motion can be described as fluctuations caused by microscopic thermal force with Langevin equation

$$m\ddot{x} + D\dot{x} + kx = F_{\text{ext}} + F_{\text{th}}(t), \tag{46}$$

where $F_{\text{th}}(t)$ is random force due to thermal fluctuations. Due to the randomness of the impacts, these forces do not correlate. From the power spectral density of a harmonic oscillator, a value for the amplitude of the displacement of the cantilever can be derived as shown in [19]. If $\omega \ll \frac{k_{\text{B}}T}{\hbar}$, where $\hbar = h/2\pi$ is Planck's constant, the potential energy of the cantilever is equal to the thermal energy

$$\langle \frac{1}{2}kx^2(t) \rangle = \frac{1}{2}k_{\text{B}}T. \tag{47}$$

Using the transfer function of a harmonic oscillator derived in Eq. 17 and defining the power density of $F_{\text{th}}(t)$ as $S_{\text{th}}(\omega)$, the spectral power density for the displacement $x(t)$ due to the thermal fluctuations is

$$S(\omega) = \frac{S_{\text{th}}(\omega)}{\left(k - m\omega^2\right)^2 + D^2\omega^2}. \tag{48}$$

With the help of Eqs. 47 and 48, the expectation value for the potential energy in the frequency domain can be calculated from

$$\frac{1}{2}k\langle x^2(t) \rangle = \frac{1}{2}k_{\text{B}}T = \frac{1}{2}k\frac{1}{2\pi}\int_{-\infty}^{\infty} S(\omega)d\omega. \tag{49}$$

Assuming the force $F_{\text{th}}(\omega)$ acting on the cantilever is white noise with a constant spectral density σ^2 and that the damping is small, we can integrate Eq. 49 by forming a residue integral

$$I = \int_{-\infty}^{\infty} \frac{dx}{(x^2 + a^2)(x^2 + b^2)}, \tag{50}$$

where

$$\left(x^4 + \left(a^2 + b^2\right) x^2 + a^2 b^2\right) = m^2 \left(\omega^4 + \frac{D^2 - 2mk}{m^2}\omega^2 + \frac{k^2}{m^2}\right). \tag{51}$$

From this equation, we can see that

$$a^2 + b^2 = \frac{D^2 - 2mk}{m^2} \ \wedge a^2 b^2 = \frac{k^2}{m^2} \tag{52}$$

and

$$(a+b)^2 = a^2 + 2ab + b^2 = \frac{D^2 - 2mk}{m^2} + \frac{2k}{m} = \frac{D^2}{m^2}. \tag{53}$$

The integral in Eq. 50 is analytical in upper half-plane except at the two poles at $z = ia$ and $z = ib$ and it will vanish stronger than $1/z^2$, which makes it possible to take the real axis and a infinitely large semicircle in the upper plane as a contour of integration. According to the residue theorem the integral over the semicircle vanishes and the

$$I = \int_{-\infty}^{\infty} \frac{dz}{(z^2 + a^2)(z^2 + b^2)} = 2\pi i \sum \text{residues}. \tag{54}$$

The residues at the poles are

$$\begin{aligned} f(z) &= \frac{1}{(z - ia)(z + ia)(z - ib)(z + ib)} && (55)\\ \text{Res}_{z=ia} f(z) &= \frac{1}{2iai^2(a^2 - b^2)} = \frac{i}{2a(a^2 - b^2)} && (56)\\ \text{Res}_{z=ib} f(z) &= \frac{1}{2ibi^2(b^2 - a^2)} = \frac{-i}{2b(a^2 - b^2)} && (57)\\ \Rightarrow I &= 2\pi i \left(\frac{i}{2a(a^2 - b^2)} - \frac{i}{2b(a^2 - b^2)}\right) = \frac{\pi}{ab(a+b)}. && (58) \end{aligned}$$

The integral in Eq. 47 can be solved with the help of previous equations as

$$\int_{-\infty}^{\infty} \frac{d\omega}{\left(k - m\omega^2\right)^2 + D^2\omega^2} = m^2 I = \frac{\pi}{kD}. \tag{59}$$

Using the results of the residue intergral, the spectral density σ^2 can be solved from

$$\frac{1}{2} k_{\mathrm{B}} T = \frac{k\sigma^2}{4\pi} \frac{\pi}{mD\omega^2}. \tag{60}$$

Inserting σ^2 from Eq. 60 into Eq. 48 we get power spectral density

$$S(\omega) = \frac{2k_{\mathrm{B}} TD}{\left(k - m\omega^2\right)^2 + D^2\omega^2}. \tag{61}$$

Root-mean-square displacement Δx_{rms} of the cantilever tip due the thermal noise below resonant frequency ω_0 with measurement time τ_{m} is

$$\Delta x_{\mathrm{rms}} = \sqrt{S(\omega)/\tau_{\mathrm{m}}} = \sqrt{\frac{2k_{\mathrm{B}} TD}{k^2 \tau_{\mathrm{m}}}} = \sqrt{\frac{2k_{\mathrm{B}} T}{m\omega_0^3 Q \tau_{\mathrm{m}}}}. \tag{62}$$

3.2.3 Signal-to-noise ratio

Signal-to-noise ratio is defined as

$$SNR(\omega) = \frac{A(\omega)}{Noise\ amplitude}. \tag{63}$$

where $A(\omega)$ is the total system response from Eq. 42. Solving amplitude Δx from Eq. 63 and omitting the effects of the high- and lowpass filters, signal-to-noise ratio for acceleration noise can be written as

$$SNR_{\mathrm{acc}}(\omega) = \frac{(\gamma-1)\alpha_{\mathrm{x}} p_{\mathrm{x}} l P_0}{\omega(m/k)\sqrt{\left(\omega_0^2-\omega^2\right)^2 + (\omega D/m)^2} V \rho_{\mathrm{C}} t \Delta a}. \tag{64}$$

If the modulating frequency ω is well below the resonance frequency ω_0 and the absorption in the gas is low, the equation for the SNR will simplify to

$$SNR_{\mathrm{acc}}(\omega) \approx \frac{(\gamma-1)\alpha_{\mathrm{x}} p_{\mathrm{x}} l P_0}{\omega V \rho_{\mathrm{C}} t \Delta a}. \tag{65}$$

The SNR for acceleration noise can be improved by decreasing the volume of the sample cell. Since the signal is proportional to the absorption length, this decrease can only be done by decreasing the radius of the cell. The volume can be decreased to a limit where other factors such as the fast cooling of the sample gas and short absorption length start to limit the signal. The increase in the SNR is due to a larger relative pressure change, since the same amount of heat is released in a smaller space.

Using the same conditions as with acceleration noise, SNR for acoustical noise SNR_{acoust} can be written as

$$SNR_{\mathrm{acoust}}(\omega) \approx \frac{(\gamma-1)\alpha_{\mathrm{x}} p_{\mathrm{x}} l P_0}{\omega V \Delta p}. \tag{66}$$

Since the external acoustic waves bend the cantilever through the same mechanism as the photoacoustic signal, the only way to increase the SNR is to reduce the radius of the sample cell. Therefore it is important to prevent acoustic waves from forming in the cell by proper design.

Signal-to-noise ratio in terms of Brownian noise can be written as

$$SNR_{\mathrm{B}}(\omega) = \frac{A_{\mathrm{C}}(\gamma-1)\alpha_{\mathrm{x}} p_{\mathrm{x}} l P_0}{\omega V k \sqrt{2 k_{\mathrm{B}} T/(m\omega_0^3 Q \tau_{\mathrm{m}})}} = \frac{A_{\mathrm{C}}(\gamma-1)\alpha_{\mathrm{x}} p_{\mathrm{x}} l P_0}{\omega V \sqrt{2 k_{\mathrm{B}} T k/(\omega_0 Q \tau_{\mathrm{m}})}}. \tag{67}$$

Again SNR of the photoacoustic cantilever system can be increased by making the sample cell smaller. It can also be enhanced by increasing quality factor Q and thus reducing the width of the resonance peak. A sharp resonance peak reduces the total Brownian noise that has equal noise amplitude for all frequencies, by limiting noise accumulated outside the resonance peak. A few techniques have been proposed to increase the Q factor by making the damping factor D smaller. Some of these techniques are discussed in Chapter 4.3.

3.2.4 Noise reduction methods

"Windowless" PAS is used to minimize power lost in the reflections and the absorption of the radiation in the window. The heating of the window will also form acoustic waves that increase system noise. Reflections can be minimized by using multilayer antireflecting coating or by placing the window at the Brewster angle. According to the Fresnel formulae, the reflectivity for a light polarized in the plane of incidence drops to zero when the angle between the reflected and transmitted beams is 90°. The use of Brewster angle works well with tunable sources since there is only a small deviation due to change in wavelength for most typically used transparent materials. [25, 42]

Acoustic baffles or buffers are used between the sample cell and the end mirrors of a multipass cavity to suppress external noises. A sharp change in the cross sections between the sample cell and a larger buffer cell can be optimized to suppress the noise signal from the windows and from the gas flow in open ended resonators. Typical multipass setup includes two or more identical buffer volumes depicted in Fig. 5 (c) but also asymmetrical volumes have been used to suppress window noise. On the other hand, openings in the acoustic cell induce radiation losses, which decreases the acoustic signal. In addition, the mixing of gas between the buffer cell and the acoustic cell will increase the rise time of the photoacoustic signal. [11]

The acoustic buffers offer the best attenuation when destructive interference occurs, i.e. their length is one quarter of acoustic wavelength. At this path length, the phase of the acoustic wave changes 180° every time it passes the buffer. When a new wave is formed at the same point, the sum of these waves is nearly a zero. Coupling between the acoustic cavity and the buffer volume can be decreased by increasing the buffer cavity dimensions. Larger dimensions also offer a better ratio between the acoustic volume and the surface area, which decreases the coupling of the signal to the walls. Window noise can be further suppressed if tunable air columns are placed near the windows as band stop filters. The ideal length for the tunable air columns is $\lambda/4$. Properly placed tunable air column can decrease the window noise down to 1/50th part. [17]

In a *differential setup*, two identical sample cells and microphones measure the same sample but only one of the cells is illuminated with IR radiation [11]. In the ideal case, the same external noise will be measured with both microphones whereas only one of the microphones will measure the photoacoustic signal. In reality, the noise components can couple differently to both sample cells and the window noise remains uncompensated. Since only one of the cells is illuminated, the acoustic noise due to window and wall heating cannot be measured in a reference cell. Due to the randomness of Brownian noise, it cannot be decreased with a differential system.

Another way is to use a single microphone system shown in Fig. 18. Modulated light is directed through two parallel cells, a reference cell containing only non-absorbing reference gas and a sample cell containing small amount of unknown gas. Both cells are connected to a u-shaped photoacoustic cell filled with unknown gas. Difference in the power of incident light creates pressure difference between the upper and lower cells that is detected with the microphone. A variable attenuator can be

used to compensate the spatial variations of optical power. A differential system combines the good sensitivity of a photoacoustic system with increased sensitivity due to the spectral correlation schemes. [43]

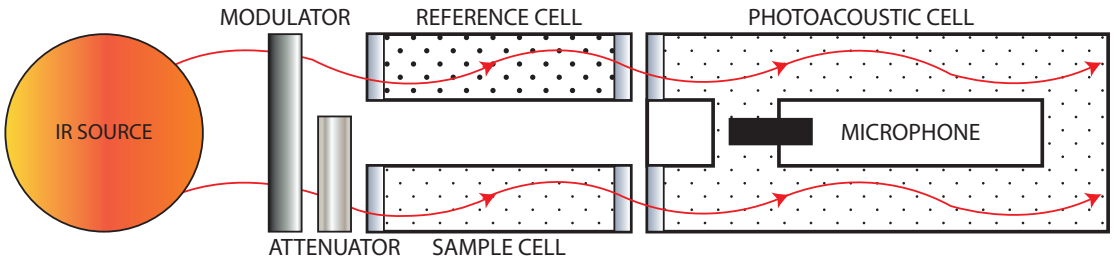

Figure 18: PAS system with a differential cell.

In addition to external noises, the differential cell system using only a single photoacoustic cell is nearly immune to the instabilities of the radiation source such as power fluctuations. Since both parts of the cell are illuminated, the window noise will be nearly equal in both parts if the absorption of the radiation in the sample cell is small. A differential photoacoustic cell system can measure flowing gas samples since the acoustic noise from the gas flow should affect both sides similarly if the positions of the connectors are selected properly. [20]

A combination of long absorption length due to the multipass structure and the good selectivity of differential photoacoustic spectroscopy has been tested with ceramic blackbody radiator, a mechanical chopper and an optical microphone. With 100 cm absorption length in the sample cell and 20 cm path length within the photoacoustic cell, the detection limit for methane was 13 ppb with 0.37 second measurement time. Using the same setup with 100 second measurement time, the concentration of 0.2 ppb of methane was measured. [4, 40]

In the *differential mode excitation* (DME), two light beams are modulated with the same modulator and then focused on the photoacoustic cell. The cell is split in three parts. Each part has different length and diameter and thus different resonance frequency. The first beam can only propagate in the first part whereas the second part can propagate through the whole structure. The first beam will mostly excite the resonant mode of the first cavity whereas the second beam will excite all of the resonance frequencies. An experimental DME-PAS system is shown in Fig. 19. [44]

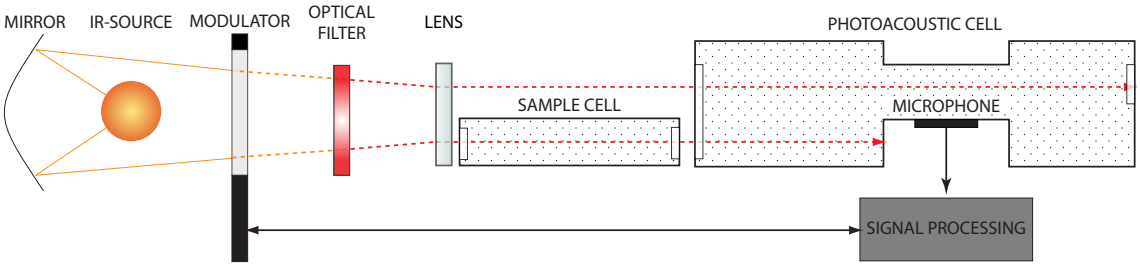

Figure 19: Photoacoustic spectroscopy system based on differential mode excitation.

A sample cell is placed in front of the first beam, which decreases the intensity as the beam propagates into the photoacoustic cell. The sample gas concentration defines the attenuation of the first beam, which can then be measured from the ratio of excited modes in the photoacoustic cell. DME uses optical correlation techniques where the sample gas acts as an optical filter. The change in the ratio of the excited acoustic modes depends only on the absorption of infrared radiation in the sample gas. This way a blackbody source can be used effectively without several spectral bandpass filters needed for adequate selectivity. Unfortunately, DME cannot be used to distinguish several components in the sample gas from each other. [44]

Since the signal depends only on the ratio of the amplitude of the acoustic modes, the DME-PAS is immune to the intensity fluctuations of the source and the microphone drifts and it has reduced frequency drift due to flowing gas thanks to the external sample cell. Since the measurements are made with a Planckian source, a large wavelength range can be used but the sensitivity is lowered. [44]

3.2.5 Summary of noise in PAS

The proper design of the photoacoustic cantilever enhanced spectroscopy system can effectively eliminate acceleration and acoustic noise and proper choosing of electrical components can minimize electrical noise compared with other sources. Brownian noise is typically dominant noise source in addition to $1/f$ like component presumably caused by the gas flow in the gap between the cantilever and the frame. The measured noise spectrum in a Brownian noise dominant system is depicted in Fig. 20.

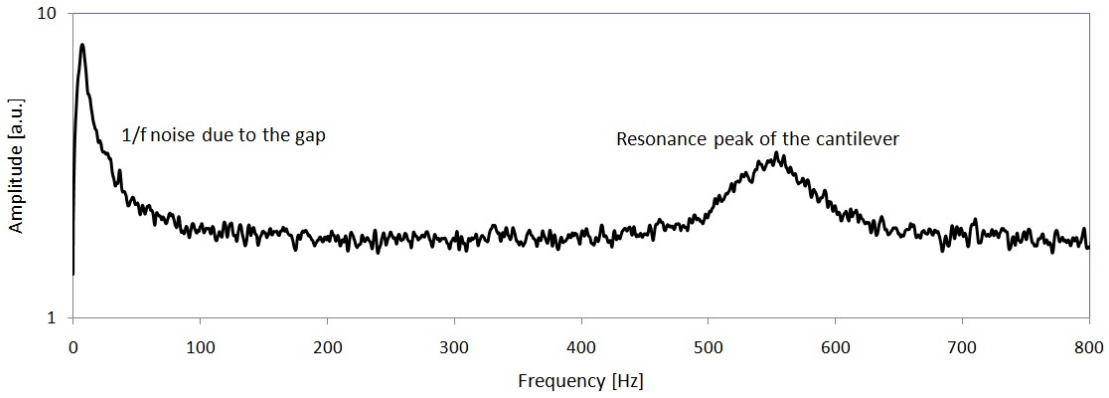

Figure 20: Measured noise in a Brownian noise dominant system.

The total noise in a photoacoustic system can be modeled as a combination of Brownian noise with noise spectrum S_1 and $1/f$ noise with noise spectrum S_2. The square of the noise spectrums is set to be identical to the thermal energy of a molecule

$$(S_1 + S_2)^2 = \frac{1}{2} k_{\mathrm{B}} T. \tag{68}$$

No analytical solution for the equation has been found, especially since the exact mechanics behind the $1/f$ noise in the cantilever remains unknown.

4 Fabrication of the micromachined cantilevers

Microfabricated cantilevers and cantilever arrays can be found in a various kinds of applications. A micromachined cantilever coated with functionalized molecules can be used for example as a chemical or a biological sensor. With an appropriate coating, a cantilever can be used to detect almost anything from bacteria to even pH values. Even more established applications include the topography imaging force sensors in atomic and scanning force microscopes. The most significant benefits of the cantilevers are their small size, fast response time and high sensitivity in the wide range of pressures or damping materials. [45].

The first part of this chapter presents the process used in Micronova for the fabrication of silicon cantilevers. The dimensions of the cantilever affect the noise components and the mechanical strength of the cantilever and they must be selected carefully in order to achieve the best SNR. Chapter 4.2 concentrates on the design of the cantilevers. The last part of this chapter presents alternative methods used by other laboratories for the cantilever microfabrication.

4.1 Microfabrication process

Silicon is the most used material in microfabrication. Silicon wafers are readily available in various sizes. Silicon has good mechanical strength and elasticity, which makes it a very good material for cantilevers even though the strength of silicon is usually hampered by its brittleness. Silicon fractures easily when the yield point is reached whereas most metals deform elastically before fracturing.

Microfabricated cantilevers are made from silicon wafers by etching away the excess silicon around the components. The structures can be protected with an oxide layer when selective etching is used to remove the rest of the wafer. The selective etching is based on the varying etching speed between different materials. In certain materials, the etching speed depends also on the properties of different crystal planes.

The crystal structure of silicon is shown in Fig. 21(a). The diamond lattice consists of 18 atoms. This structure is the smallest periodically repeating pattern in the crystal lattice. The planes in the cell can be described with Miller indices shown in Fig. 21(b–d). The properties of silicon depend on the plane, for example the Young's modulus E is approximately 150 GPa in (100) plane and 190 GPa in (111) plane. [46]

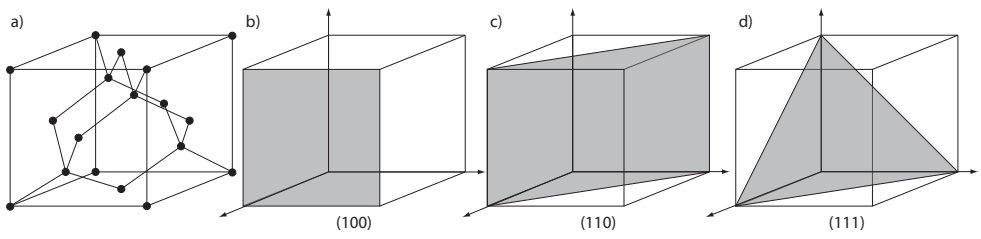

Figure 21: (a) Crystal structure of silicon (b) (100) (c) (110) (d) (111) plane.

4.1.1 Cleaning and oxidation

The fabrication process of the cantilevers made for photoacoustic spectroscopy used in Micronova is based on commonly available, boron doped, (100) oriented silicon-on-insulator (SOI) wafers. The used SOI wafers have a three layer structure, where a 1 μm thick silicon dioxide layer is buried between 10 and 380 μm thick silicon layers. The upper layer is called the device layer and it defines the thickness of the cantilever while the lower, handle layer determines the thickness of the frame. [37]

At the beginning of the fabrication process, the SOI wafers are wet cleaned to prevent unwanted contamination in processes and to prepare the surface of the wafers to a known condition. Wet cleaning is performed by sinking the wafers in cleaning baths. Because of the wide variety of impurities, multiple cleaning solutions must be used. The used cleaning solutions are RCA-1 ($NH_4OH : H_2O_2 : H_2O$, 1:1:5), RCA-2 ($HCl : H_2O_2 : H_2O$, 1:1:6) and DHF (dilute hydrofluoric acid, $HF : H_2O$, 1:50), where the first two RCA cleans are also known as the standard clean. Cleaned wafers are coated with 95 nm thick silicon dioxide film in thermal wet oxidation as shown in Fig. 22(a). The oxidation takes approximately 10 min at 1000 °C. [46]

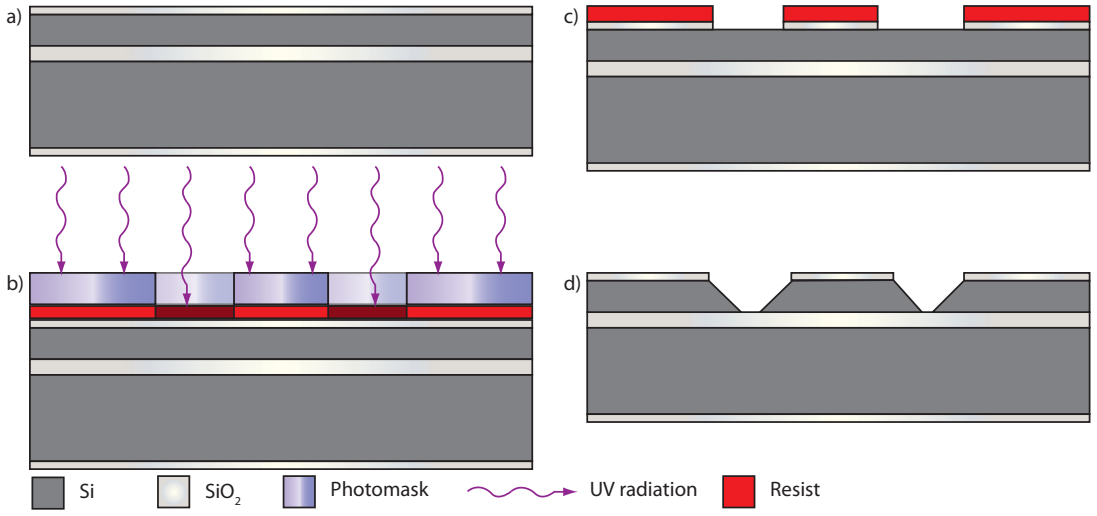

Figure 22: (a) Oxidized SOI wafer (b) Illumination of the resist (c) Oxide etch (d) Si etch. Courtesy of Päivi Sievilä.

Certain etches such as tetramethylammonium hydroxide (TMAH) and ethylene-diamine pyrocatechol (EDP) etch silicon fast but oxide very slowly whereas buffered hydrofluoric acid (BHF) is used to etch silicon dioxide. This effect can be used to selectively etch silicon by forming an oxide layer on top of the wafer. Due to the oxygen in air, a thin film (approximately 1 nm) of native silicon dioxide is formed when silicon is exposed to air. Micrometer thick layers can be grown with thermal oxidation. In thermal oxidation, silicon wafers are exposed to oxygen or water vapor at high temperatures, typically 800–1200°C. The water vapour forms silicon dioxide faster, but the formed layer is also more prone to defects. [46]

4.1.2 Optical lithography

Silicon dioxide forms a uniform layer on top of the wafer. In order to only protect selected parts, an additional layer is needed to define holes in the SiO_2 layer. This can be done with a photoresist and optical lithography. Solubility of the photoresist changes when it is exposed to ultraviolet (UV) radiation. Therefore a partially transparent photomask placed between the wafer and the UV source can be used to define patterns in the resist. Usually, the adhesion of the photosensitive resist is increased for example by growing a monomolecular layer of hexamethyl disilazane (HDMS) on the surface of the wafer. [46]

The wafers are first prepared for the HDMS treatment by heating them at 120 °C for 10 min. This heating is needed in order to remove moisture from the wafers. After the HDMS is evaporated on the wafer in vacuum, liquid photoresist is spin coated on the device layer. In spincoating, the wafer is attached to a holder with a vacuum pump and 3 ml of liquid resist is applied on the wafer. The spinner is then accelerated to several thousands of rpm spreading the resist very evenly. Excess solvent is removed from the wafer by soft baking the wafers in an oven at 90 °C for 20 minutes.

A simple way to define the patterns on the photoresist is to use a transparent photomask from which selected areas are covered with opaque films. When the photomask is used to expose parts of the wafer to UV radiation as is shown in Fig. 22 (b), the solubility of these parts changes. When the resist is sunk in a developer, exposed parts of the resist are removed. The photomask can be used either in proximity or contact lithography. In contact lithography, the wafer and the photomask are pressed together, whereas in proximity lithography a small gap is left between the mask and the wafer. A better resolution is achieved with the contact method but the risk of mask damage is also higher. The proximity lithography is not as susceptible to damage, but the achieved resolution is worse due to the diffraction of light in the gap. The current process is implemented using the contact mode, where the wafer is pressed against the photomask and exposed to UV radiation for 2 seconds. [46, 37]

After the wafer is exposed to the UV light, it is dipped in the developer and the exposed areas are removed revealing the selected parts of the oxide layer, which define the shape of the cantilever in the device layer as shown in Fig. 22 (c). The wafer is then postbaked in an oven at 120 °C in order to ensure that the resist will not be etched with the revealed oxide layer. The bulk side of the wafer is also protected with the photoresist in order to protect the SiO_2 film. When both sides of the wafer are protected by the photoresist, the wafer is sunk into a silicon dioxide etch until the device layer is revealed. After the oxide is etched, the photoresist is stripped with acetone and isopropyl alcohol (IPA) to form the structure shown in Fig. 22 (d).

4.1.3 Etching

There are two basic methods for etching, wet etching and dry plasma etching. In wet etching, a solid material reacts with liquid etchant leaving soluble products and in

plasma etching, a solid material and a gaseous etchant lead to volatile products. A typical etch rate for both methods vary from 100 to 1000 nm/min. One of the most used methods for making microfabricated systems from silicon is *anisotropic wet etching*. Different crystal planes in silicon have distinct etching rates, which leads to typical v-groove and inverted pyramid structures when a (100) oriented silicon wafer is used. A common anisotropic wet etchant, potassium hydroxide (KOH) can have a 200 fold difference between the different planes. A wet etching mask must be designed by taking into account the sloped walls, i.e. the varying etching rate between planes, which lead to larger gaps on the mask. [46]

TMAH is used in the current process as the anisotropic wet etchant. At first, the TMAH solution is heated up to 86 °C, which increases the etching rate. The wafers are kept in the etchant until the buried oxide becomes visible. After the TMAH etching, the wafer is dipped into BHF solution until the silicon dioxide mask is removed from the wafer.

As an alternative anisotropic plasma etching, also known as *reactive ion etching* (RIE) can be utilized. In RIE, the wafer is bombarded with ions in a plasma reactor making it possible to fabricate almost vertical walls. The size of the structures follows the exposed photoresist very closely. In the process described, RIE can be used to etch silicon dioxide. [46]

A special method of RIE can be used to make deep trenches. In *cryogenic deep reactive ion etching* (DRIE), the wafer is cooled below −100 °C in order to slow down the isotropic etching. The cold temperature can crack resist films and therefore other materials are used as the etching mask. Only the lateral surfaces are removed by the ion bombardment and thus vertical walls can be obtained. Another advantage of the anisotropy in RIE is the immunity to the undercutting of the corners. [47]

4.1.4 Handle side processing

Freed structure is re-oxidized in order to protect the etched device layer. The wafer is thermal wet oxidized in 1000 °C for 420 minutes in order to form a 100 nm thick SiO_2 layers. The oxide layer thickness must be selected to match the buried oxide layer thickness after the second wet etching. If the thicknesses match, the shear stress bending the cantilever will be effectively compensated. The lower side of the wafer is prepared as earlier for the lithography process used to define rectangular shape under the cantilever. Exposed areas are etched in the oxide etchant and afterwards in TMAH until the buried oxide shown in Fig. 22 is reached. Usually, a slightly larger area is etched below the cantilever. This etching forms a thin frame around the cantilever, which in turn is connected to the 380 μm thick bulk. This process will take approximately 11 h for a 380 μm thick wafer. The last step is to release the cantilever by removing the oxide layers with BHF solution. [37]

4.2 Cantilever design

We can deduce the relation between the displacement of the cantilever and the dimensions of the cantilever from Eq. 42 as

$$A(\omega) \propto \frac{A_{\mathrm{C}}}{m\sqrt{\left(\omega_0^2-\omega^2\right)^2+\left(\omega D/m\right)}}\left(\frac{9A_{\mathrm{g}}^2 v_{\mathrm{sound}}^2}{16\gamma V_{\mathrm{eff}}^2\omega^2}+1\right)^{-1/2}. \tag{69}$$

This can be approximated in the low frequency range ($\omega \ll \omega_0$) as

$$A(\omega) \propto \frac{A_{\mathrm{C}}}{k} = \left(\frac{2}{3}E\frac{t^3}{l_{\mathrm{c}}^4}+\gamma\frac{A_{\mathrm{C}}p}{2,5V_{\mathrm{eff}}}\right)^{-1}, \tag{70}$$

if the size of the gap and the damping factor are small. In addition to the maximum displacement, we are also interested in the minimum detectable force. If a Michelson interferometer is used to measure the displacement, the sensitivity of the system is limited by the Brownian noise. Using Eq. 62 with the relations $F = kx$ and $k = m\omega^2$, the minimum detectable force is

$$F_{\mathrm{min}} = \sqrt{\frac{2kk_{\mathrm{B}}T}{\omega_0 Q\tau_{\mathrm{m}}}} = \sqrt{\sqrt{\frac{k}{m}}\frac{2k_{\mathrm{B}}T}{Q\tau_{\mathrm{m}}}}. \tag{71}$$

From this equation, we can see that the sensitivity of the cantilever can be increased not only by decreasing the effective spring constant but also by increasing the Q value and the measurement time τ_{m}. Therefore the relation between the quality factor and the dimensions must be known in order to maximize the sensitivity.

4.2.1 Attenuation due to the gap

The attenuation would decrease quickly if the gap was made narrower, but the width of the gap is limited by the wet etching process. At the moment, the TMAH etching can reliable produce gap widths in the range of 3...5 μm. TMAH could in theory etch infinitely narrow gaps, but in practice the nonuniformity of the wafers, the resist and the etches limit the minumum achievable width.

The use of DRIE etching could in theory reduce the gap width down to 1 μm, which is the minimum linewidth of the mask aligner used in Micronova. A thinner gap could be milled with a focused ion beam, but it would be much slower and the cantilevers would have to be milled one by one. The only way to reduce the gap size with the current fabrication process is to reduce the length or the width of the cantilever. When the measurements are made at 10 Hz, the attenuation due to the gap is approximately one percent and the effective spring constant has much larger effect on the sensitivity. Very narrow gaps could jam the cantilever if the walls are uneven or if the cantilever lengthens due to its movement or heating.

Another factor added to the gap size is the undercutting of the convex corners shown in Fig. 23 (a) due to the fast and slowly etching planes even though several corner compensation designs have been developed in order to reduce the rounding

effect shown. One of these designs is shown in Fig. 23 (b) [46]. At present, the corner rounding induces very minor effect since it increases the area of the gap only less than 0.1 %. Additional holes or piles may appear in the cantilever or in the frame due to faults in the fabrication process.

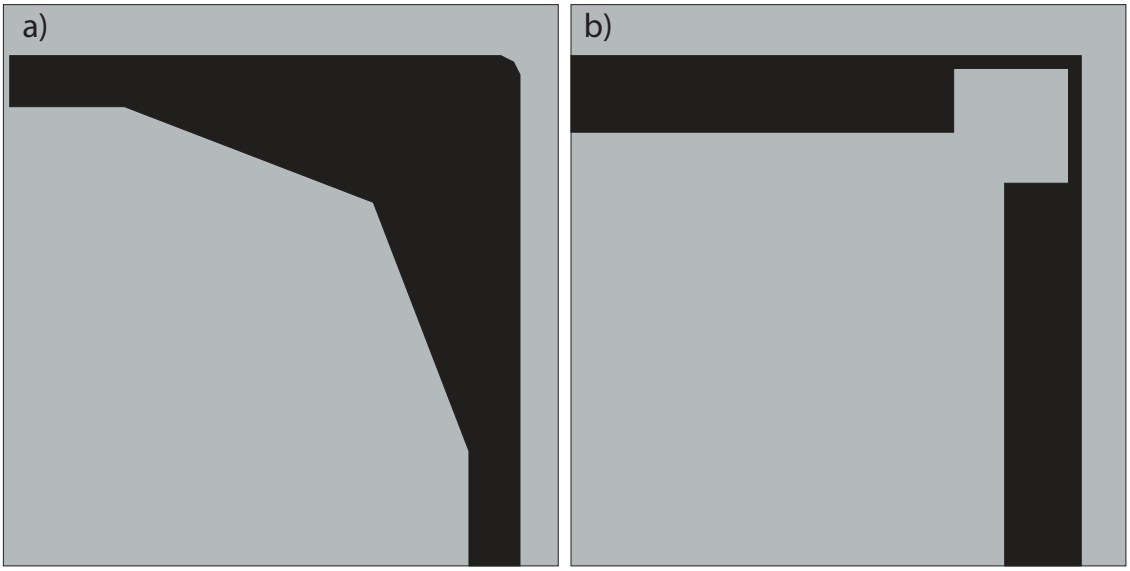

Figure 23: (a) Undercutting of convex corners in (100) Si (b) Structure used for corner compensation.

Other faults in the fabrication process can also affect the gap size. Uneven photoresist, dirt in the photolithography step, scratches and inhomogeneous etchants cause varying surface structures. A thin photoresist may be developed even if it was not exposed to UV light. A hill will appear when a dust particle blocks UV light from a spot and the photoresist will not be removed in the developer. Additional holes in the cantilever could increase the gas movement and thus increase the gap area and the gas flow due to the temperature and the pressure difference.

4.2.2 Damping factor

The damping factor must be taken into an account if a more accurate model is wanted. The damping effect is directly proportional to the speed of the cantilever and it can be described with

$$D = \frac{k}{\omega_0 Q}. \tag{72}$$

This form will show the relation between the amplitude and the quality factor Q as

$$A(\omega) \propto \frac{A_{\mathrm{C}}}{\sqrt{(k-\omega^2)^2 + k\omega^2/Q^2}}. \tag{73}$$

One way to increase the quality factor is to use a feedback system presented in Chapter 4.3.

4.2.3 Increasing the sensitivity of the cantilever

The internal spring constant of the cantilever can be reduced notably by decreasing the thickness of the cantilever. At the moment, the thickness of the cantilever is defined by the device layer of the SOI wafer. Another factor limiting the thickness of the cantilever is the damping caused by gases at atmospheric pressures. A very thin cantilever could break under pressure, which would limit the dynamic range. Reducing the thickness would also decrease the first flexural resonant frequency. If the resonance frequency was tuned too low, the 1/f noise would decrease the SNR.

If the gas spring term would be reduced for example by lowering the pressure, the sensitivity could easily be increased by making the cantilever longer. The length of the cantilever is mainly limited by the mechanical stress and strain caused by the manufacturing process. Longer cantilevers would require thicker structure, which would reduce the sensitivity. The length of the cantilever can also limit the dynamic range since the beam must reflect back to the interferometer. If the angle between the cantilever and the frame grows too large, the reflected beam will not illuminate the detectors and the signal cannot be detected. An increase in the length would also increase the area of the cantilever, which in turn increases the gas spring constant.

A narrower cantilever would reduce both spring constants, but the width is currently limited by the interferometer. Narrower cantilevers could be used if an additional lens was added after the beam splitter, but they would make the whole system more complicated and less robust. In most applications, the sensitivity of the system is limited by the Brownian noise. If the sensitivity is kept constant, the length of the cantilever can be decreased with the thickness with the ratio of t^3/l_c^4. These shorter cantilevers would have higher resonance frequency and more of them could be fabricated with each wafer.

4.2.4 Coating of the cantilever

The refractive index of the material determines the fraction of incident light reflecting from the cantilever. When a multilayer structure is used, light will be reflected from every interface. If the thickness of the layer is smaller than the coherence length of the laser, interference will occur at these reflections. When the incident laser beam is perpendicular to the cantilever, the intensity reflectance can be calculated from

$$R = |r|^2 = \left| \frac{(m_{11} - m_{22}) + i\,(m_{12} - m_{21})}{(m_{11} + m_{22}) + i\,(m_{12} + m_{21})} \right|^2 , \tag{74}$$

where m_{ij} are entries from a matrix M. When a cantilever is coated with gold, a thin titanium adhesion layer is needed between the silicon surface and the gold coating. The coatings are usually placed on both sides in order to compensate the residual stress. This forms a structure of several stacked thin films with different refractive indices. Each of these films can be represented with a matrix

$$M_{\mathrm{j}} = \begin{pmatrix} \cos(\delta_{\mathrm{j}}) & \frac{i}{n_{\mathrm{j}}} \sin(\delta_{\mathrm{j}}) \\ i n_{\mathrm{j}} \sin(\delta_{\mathrm{j}}) & \cos(\delta_{\mathrm{j}}) \end{pmatrix}, \tag{75}$$

where n_j is the complex refractive index of the jth layer. δ_j is the phase change due to the layer, which can be calculated from

$$\delta_\mathrm{j} = \frac{2\pi}{\lambda} n_\mathrm{j} t\mathrm{j}, \tag{76}$$

where t_j is the thickness of the film. The whole structure can be described with a product matrix $M = M_1 M_2 M_3 ... M_\mathrm{n}$. In real applications, the angle between the incident beam and the cantilever changes, but this change is usually less than 0.02° and it is therefore omitted here. [48]

The complex refractive indices for titanium, gold and silicon at 632.8 nm are $n = 2.15325 - i2.9248$, $n = 0.19683 - i3.09054$ and $n = 3.88126 - i0.018938$, respectively [49]. Using 3 nm thickness for the titanium layers between silicon and gold films, the intensity reflectance for 4.5–5.5 μm and 10 μm thick cantilevers as a function of the thickness of the gold layer is shown in Fig. 24.

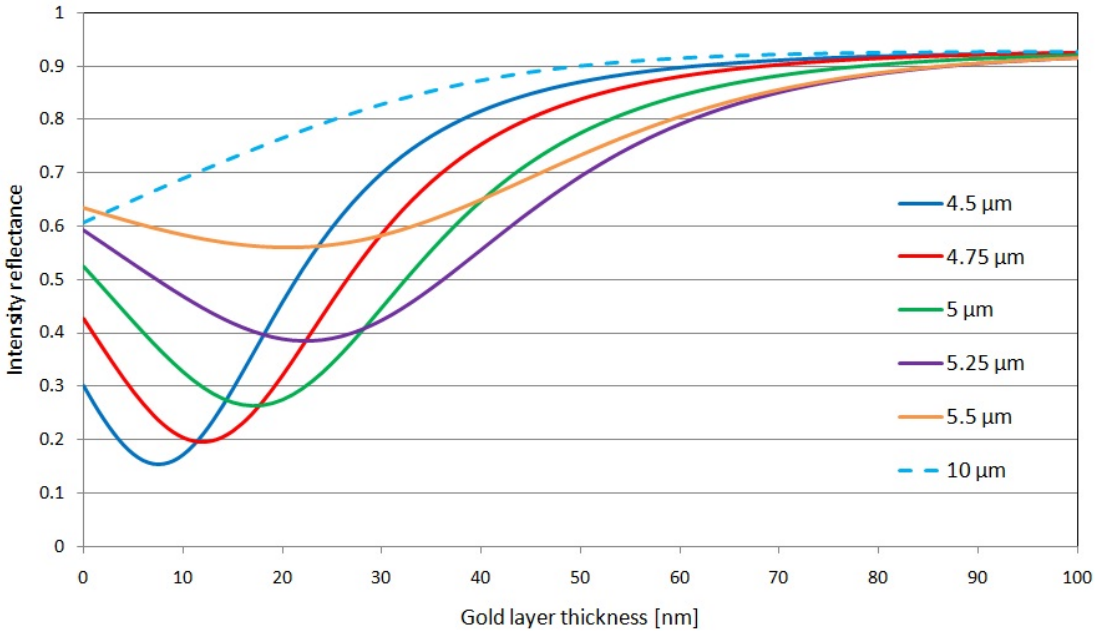

Figure 24: Intensity reflectance of six thin cantilevers.

The reflectance of the pure silicon cantilever without the titanium coating is approximately 5 % higher than what is shown in Fig. 24. The 10 μm thick cantilevers can be measured without coating, but to obtain a strong signal, reflectance of 80 % or higher is wanted. Unfortunately, even a small thickness variation in the 5 μm thick cantilevers can make optical measurements impossible. Regardless of the thickness of the wafer, a 50...60 nm thick gold layer on both sides of the cantilever should provide reflectance high enough for the interferometer.

4.3 Quality factor of the cantilever

The Q factor can be expressed as a relation between stored energy and energy lost in each cycle of vibration. Even a perfect crystal dissipates mechanical energy. The related fundamental processes are thermoelastic dissipation (TED) and phonon-phonon interactions. Thermoelastic dissipation is caused by continuous volume changes in a vibrating structure. These variations of volume transfer locally into thermal energy, which is then lost. Phonons are vibrations of the crystal lattice. A sound wave can create local changes in the phonon distribution function, i.e. increase the number of phonons in one part and decrease it in other. The phonon-phonon interaction restores thermal equilibrium in a system where phonon distribution function is perturbed away from equilibrium by a sound wave. [50]

Part of the mechanical energy is coupled to the frame and some of it is lost in the movement of the defects. For a thick cantilever, most of the internal losses occur due the bulk effects. Making the cantilever thinner will increase the surface to volume ratio. The surface effects will thus begin to dominate when the cantilever is thinned down to sub-micron dimensions. The Q value can be written as a sum

$$\frac{1}{Q} = \frac{1}{Q_{\text{clamping}}} + \frac{1}{Q_{\text{TED}}} + \frac{1}{Q_{\text{volume}}} + \frac{1}{Q_{\text{surface}}} + \frac{1}{Q_{\text{other}}}. \tag{77}$$

For an infinitively large frame, the Q_{clamping} can be approximated as $2.17\,(l/t)^3$. [51]

A typical photoacoustic cantilever has a l/t ratio of 500 leading to $Q_{\text{clamping}} > 2.7 \times 10^8$. The flexural vibrations warm the compressing side and cool down the expanding side of the cantilever. Thermoelastic Q value can be expressed as a product of the material dependencies of the TED and the ratio of the cantilever frequency to the rate of heat flow across the cantilever thickness. If the coefficient of the thermal expansion is α, the quality value can be written as

$$Q_{\text{TED}} = \frac{(\pi G)^2 + (2fpc_{\text{p}}t^2)^2}{2f\alpha^2 TEGt^2}, \tag{78}$$

where G is the thermal conductivity of the cantilever, p the pressure, c_{p} specific heat capacity and t the thickness of the cantilever. For a 10 μm thick cantilever at $f = 600$ Hz, $Q_{\text{TED}} = 10^7$ and even higher at lower frequencies. [51]

The Q factor due to the volume effects is defined by the ratio of real and imaginary part of the Young's modulus. These values are constants depending on the material but usually the real part is much larger and therefore the Q value is not limited by the volume effects. The Q value due to the surface effects can be approximated as

$$Q_{\text{surface}} = \frac{wt}{2\delta(3w + t)} \frac{E_1}{E_2^S}, \tag{79}$$

where E_1 is the real part of the Young's modulus, E_2^S the dissipative effects (surface contamination, disruption of atomic lattice at interface) of the surface and δ the thickness of the surface layer. Again, E_1 is usually much larger than E_2^S and therefore Q_{surface} is very large. Since the Q values for the cantilever even in the relatively

low pressure of 0.1 mbar are approximately 1000, we can see that Q factor of the microfabricated cantilevers is limited by other factors, which in turn are dominated by the gas damping. The Q factor depends also on the doping of the silicon wafer. High purity single crystal silicon can have over an hundredfold times higher Q factor than heavily boron-doped structures [52]. [51]

Several attempts have been made in order to increase the quality factor with feedback systems. In the parametric amplification, the thermal noise is limited by periodically modulating the spring constant. This modulation can be done for example by electrically or magnetically affecting coils or electrodes on the cantilever since the spring constant of some materials show temperature dependence. The maximum increase in the spring constant should be applied when the displacement of the oscillator is the largest. Since the energy stored in an oscillator depends from the spring constant, the parametric amplification can increase the energy. Unfortunately, this method induces thermal noise to the system and cannot therefore be used to increase the Q value of a Brownian noise limited system. [53]

Another approach is to use external force to dissipate thermal energy. Additional external force $F_{\text{ext}} = -D'\dot{x}$ in Eq. 46 can act as an external dissipative force, which will reduce the total thermal energy of the cantilever by a factor of $1 + D'/D$. Dissipative force F_{ext} will always reduce the true amplitude of the thermal vibrations. Therefore it cannot be used to separately suppress Brownian noise without decreasing the acoustic signal. This method has been shown to decrease the thermal movement of an atomic force microscopy (AFM) cantilever. Unfortunately, this method can be only applied to static measurements and thus it cannot either increase the sensitivity of a PAS system. [54]

4.4 Other possible materials and structures

The current fabrication process has produced very sensitive cantilevers and further refining of the dimensions can make these cantilevers smaller and even more sensitive. The downside of the fabrication process is its complexity. Silicon dioxide and silicon nitride cantilevers could be grown on a bulk silicon wafer and they could be etched selectively. Thus SOI wafers would not be needed, since SiO_2 and Si_3N_4 thin films can be grown with almost arbitrary thicknesses. An alternative method for fabricating silicon cantilevers from a bulk wafer is also presented. At the end of this chapter, alternative shapes for future cantilevers are presented.

4.4.1 Silicon dioxide cantilevers

Even though the strength of silicon makes it an appropriate material for micromachined cantilevers, the high Young's modulus of silicon limits the sensitivity since the spring constant is directly proportional to E. Young's modulus for silicon dioxide is less than half of the modulus of silicon (70 GPa vs. 169 GPa), which means a smaller spring constant for a similarly sized cantilever. SiO_2 is commonly used to fabricate nanometer sized cantilevers but since it is more fragile than silicon it is not very suitable for millimeter sized PAS cantilevers. Another disadvantage of SiO_2

cantilevers is their need for coating since the silicon dioxide has a lower refractive index than silicon making it almost transparent.

SiO_2 cantilevers have been fabricated for example at the Technical University of Denmark by growing a 850 nm thick thermal oxide layer on the top of a silicon wafer. The cantilever was patterned with UV lithography and released with reactive ion etching. Their largest cantilever was only 209 μm long and 10 μm wide but even larger ones can be made. The cantilevers were coated with gold and the Q factor of uncoated and coated cantilevers were measured in vacuum and at atmospheric pressure. The 100 nm coating reduced the Q value of a 850 nm thick SiO_2 cantilever to half in vacuum but at atmospheric pressure the coating increased the Q value slightly. Even though the gold coating increased the thermoelastic damping, it also increased the mass, which in turn increased the total vibrational energy. The gold coating should be as thin as possible since in a PAS system the increased mass would lead to a decrease in sensitivity. [55]

4.4.2 Silicon nitride cantilever

Another material for a micromachined cantilever is silicon nitride (Si_3N_4) used for example by Lee and White. Depending on the deposition methods of (Si_3N_4), Young's modulus is roughly the same for silicon and silicon nitride. The density of silicon nitride is higher, which would mean an increase in the spring constant unless this is compensated with a thinner layer of material.

At the beginning of the fabrication process shown in Fig. 25, the cleaned silicon wafer is coated with 200 nm thick thermal oxide layer. A 500 nm thick silicon nitride layer is grown by low pressure chemical vapor deposition (LPCVD). The silicon nitride layer is released from below by anisotropic wet etching. In order to control the residual stress, another 500 nm thick silicon nitride layer is grown on both sides of the membrane. When both nitride layers bend the cantilever in opposite directions with larger stress than the initial layer, the relative stress on one side is reduced and the cantilever does not bend during the process. [56]

A piezoelectric ZnO layer is grown on top of the structure with two polysilicon electrodes used for electrical measurements. The layers are insulated from each other with two low temperature deposited silicon dioxide (LTO) layers. The electrodes were covered with a sputtered 500 nm thick Al contacts as shown in Figs. 25 (c) and (d).

A 500 nm thick sputter deposited Al layer is grown on the back side in order to support the cantilever during the etching processes. The cantilever is released from the front side with silicon dioxide and silicon nitride etches and from the back side with Al etch as shown in Fig. 25 (e) and (f). [56]

4.4.3 Alternative method for fabricating silicon cantilevers

An alternative method for fabricating the silicon cantilevers was tested at the Institute of Semiconductor Technology of the Technical University at Brunswick [34]. The same fabrication process based on a bulk silicon wafers have been also tested at Micronova. In the fabrication process silicon dioxide layers are grown on both

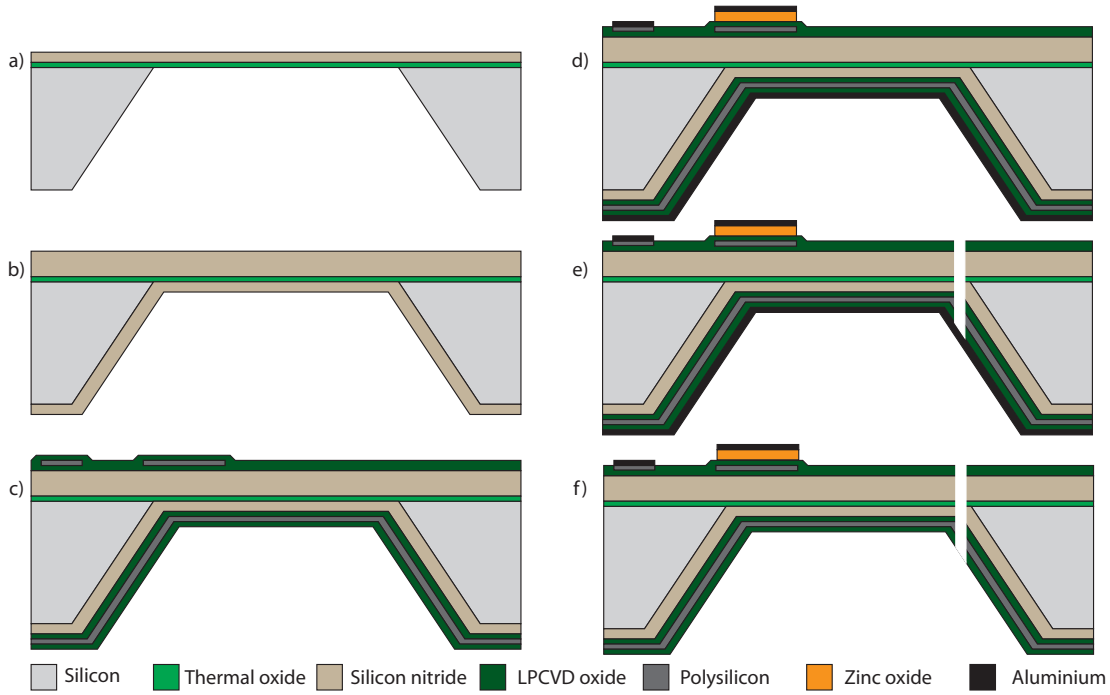

Figure 25: Fabrication process flow for silicon nitride cantilevers: (a) Bulk etched Si/Si_3N_4 (b) Second Si_3N_4 layer (c) Polysilicon electrodes (d) Al support (e) Front side etch (f) Al etch.

sides of the wafer in order to protect the wafer during the etching. The cantilever is patterned with optical lithography and V-grooves (due to the anisotropic etching of different crystal planes) determining the thickness of the cantilever were etched with TMAH. After the etching, the wafer was re-oxidized and the handle side of the wafer were etched until the v-grooves on both sides combined and the cantilever was released from the back side. [37]

In theory, the gap width could be made very small, but due to the problems described in Chapter 4.2.1, the minimum widths of the gap were considerable larger than what have been achieved with the current process. Maybe the largest disadvantage of this fabrication process is the stress between the silicon and silicon dioxide layers, which can deform or even break the cantilever. With a proper doping, the etching could be stopped at the interface of the doped layer. Due to the exponential doping profile, this method is not very accurate and the dopants itself may change the vibrational properties of the cantilever. [37]

4.4.4 Piezoelectric measurements

The piezoelectric effect used in Chapter 4.4.2 is based on material with acentric crystal symmetry and ionic bonding. When the material is strained, the center of gravity for negative and positive charges differs and an electric dipole is formed. The electric charge can be measured as such with a charge amplifier or by growing the piezoelectric layer on top of the gate oxide of a metal-oxide-semiconductor field-

effect transistor. When the piezoelectric layer is stressed, the electric dipole affects the drain current, which can be measured with increased accuracy. Even though optically measured cantilevers have better sensitivity, piezoelectric materials can be used more easily to integrate the whole gas detection system on a single chip. Cantilevers with 2x2 mm^2 area and 5...10 μm thickness coated with 1 μm thick layer of piezoelectric material measured with a charge amplifier has been used to detect nitrogen concentrations down to 330 parts per million [57]. The disadvantage of piezoelectric systems is their need for power, which will heat the cantilever and cause additional noise to the measurements. [38]

4.4.5 Alternatively shaped cantilevers

A Swiss team has showed that additional holes in the cantilever can reduce the spring constant. The team used rectangular cantilevers which were 464 μm long, 74 μm wide and 4.97 μm thick. The spring constant of the cantilever was reduced by 74 % when the thickness of the cantilever was locally thinned near the support down to 1 μm. An additional 4.2 μm wide and 40 μm long hole in the cantilever reduced the spring constant by 25 %. These holes are relative simple to make since they can be altered at the same time as the rest of the device layer defining the cantilever shape. Unfortunately, the stress near the holes increases much faster than the sensitivity and therefore the treated cantilevers can break easily. [58]

The movement of the cantilever limits the possible shapes of the cantilevers if the gap between the cantilever and the frame is kept small. A rectangular shape is the most used since it is easy to etch and it will not stuck easily to the frame. Even though triangular cantilevers are used for example as a tip for AFM, they are not very efficient at the pressure measurements, since only a small part of the force will affect the tip of the cantilever, which will limit the maximum displacement. In addition, the beam size of the interferometer laser sets the limit to the minimum width of the cantilever.

5 Measurement setup

In this chapter, the measurement setup used in this thesis to measure various cantilevers is presented. As presented earlier, in order to measure the sample gas, a photoacoustic system needs a (tunable) infrared source and a microphone. The signal from the microphone is usually digitally processed in order to transform it into a more appropriate form. The last part of this chapter is dedicated to the measured and modeled cantilevers.

The cantilevers were measured using a photoacoustic setup shown in Fig. 26 manufactured by Gasera Ltd. The cantilevers were placed in a gold coated, 40 mm long photoacoustic cell with a volume of 2 ml. The photoacoustic cell is connected to a balance cell with a volume of 8 ml. The sample cell consisted of the sample cavity, two BaF_2 windows for the incoming and transmitted infrared radiation and two electrically controlled valves for the sample gas exchange. The incident beam was focused with a lens having a focal length of 8.0 mm and numerical aperture (NA) of 0.50.

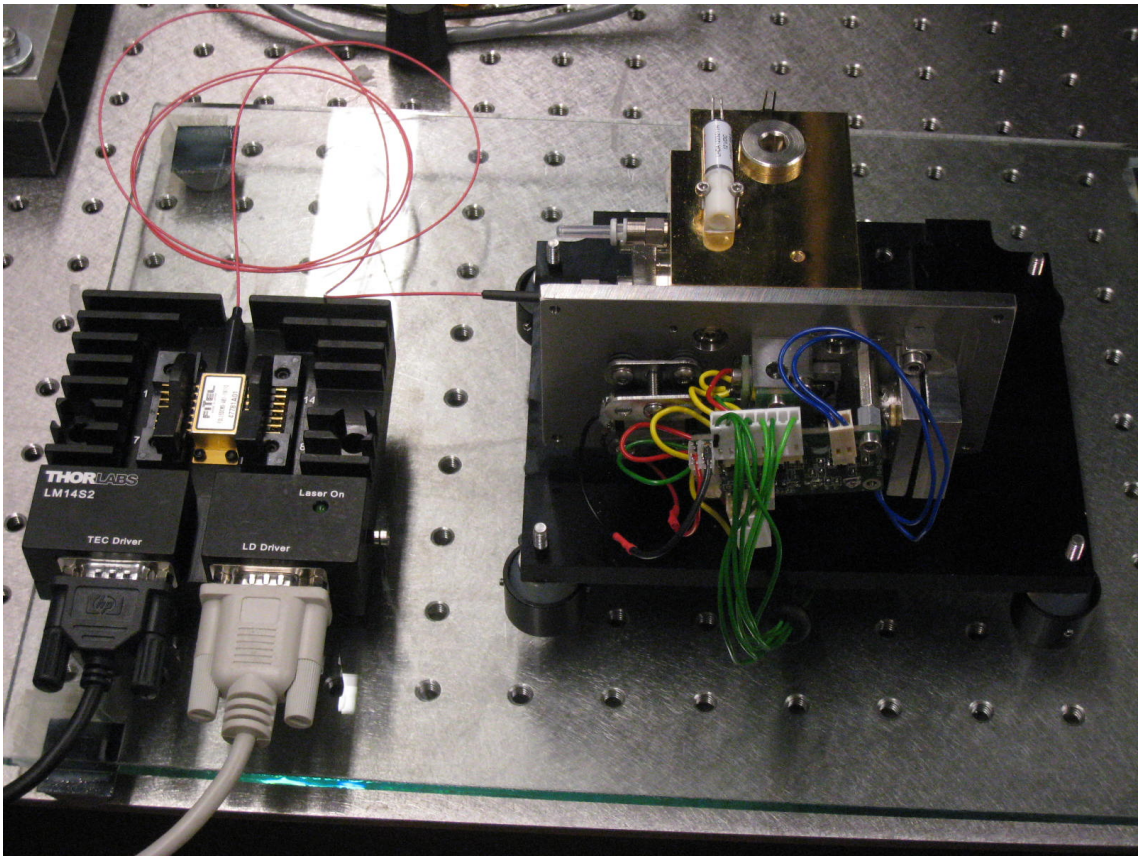

Figure 26: A diode laser connected to the photoacoustic system.

5.1 Diode laser

The sample gas was excited with a 1566 nm DFB diode laser. The more specific information for the laser is given in Table 1. The laser was connected to a 14-pin butterfly mount and was controlled with a Thorlab TEC 2000 thermoelectric temperature controller and a LDC 500 laser diode controller.

Table 1: Diode laser [14].

Manufacturer	Fitel Technologies Inc.
Model	FOL15DCWD-A81-19110
Maximum optical output power	40 mW
Maximum laser diode current	350 mA
Maximum thermoelectric element current	1.6 A
Minimum wavelength	1566.0 nm
Maximum wavelength	1571.5 nm
Line width	150 pm

The optical power of a diode laser depends on the diode current. When a semiconductor junction is forward biased, electrons and holes can recombine and emit a photon. When the current is low, the gain of the laser is lower than the losses and the spontaneous emissions dominate. When the current increases, the gain increases and optical power increases rapidly due to the stimulated emission. The optical power and the wavelength are shown as a function of diode current at 25°C in Fig. 27. The optical power can be tuned almost linearly with the current. Unfortunately, the wavelength changes with the current and the temperature of the laser must be changed in order to compensate this change in temperature.

According to the band theory, the atomic energy levels expand into energy bands. At 0 K, the highest band filled with electrons is called a valence band and the lowest empty band a conduction band. These bands are separated by a bandgap, which changes as a function of temperature. The bandgap defines the wavelength of the laser and therefore the wavelength can be changed by warming or cooling the diode laser.

The temperature of the diode laser is changed with a thermoelectric cooler (TEC) based on the Peltier effect. The Peltier effect can be seen when current is flowing through a junction between two different conductors. Depending on the direction of the current, the junction heats up or cools down. This effect is due to the difference in the energy of the charge carriers in different materials. Since the current, or the number of charge carriers, is equal in both materials, the energy (temperature) of the lattice must change when the energy of the charge carriers changes. [38]

Since the temperature of a diode laser depends from the current flowing through the diode and the ambient temperature, a thermistor is needed in order to monitor the temperature. The thermistor is a resistor with a high temperature dependence.

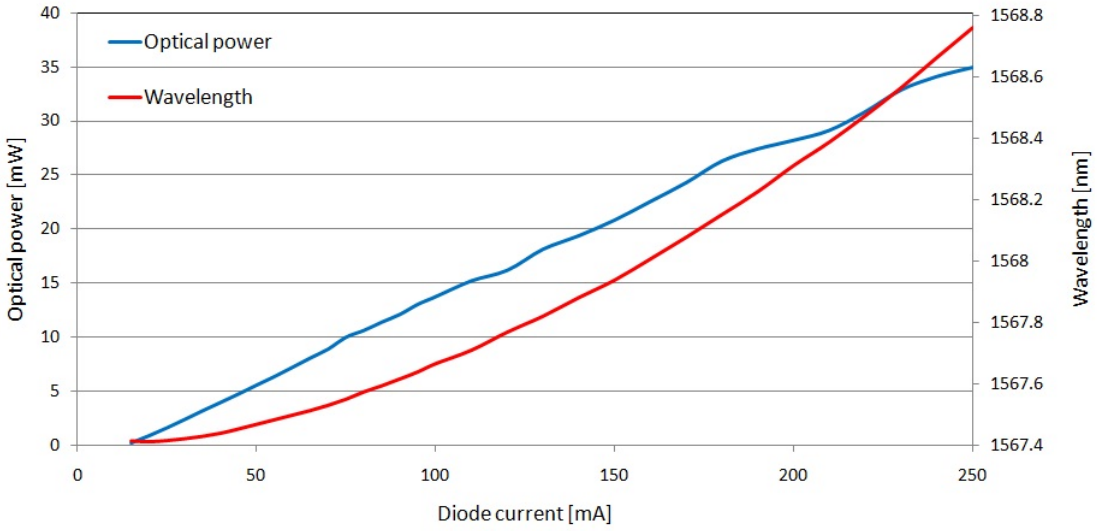

Figure 27: Wavelength and optical power of a laser diode as a function of current

The resistance of the thermistor can be calculated from

$$R(T) = 10\mathrm{k}\Omega \exp\left(B(1/T - 1/T_{25})\right), \tag{80}$$

where $B = 3900$ K is the energy constant and $T_{25} = 25°\mathrm{C}$ the nominal temperature [14]. The resistance is continuously measured by the TEC controller and the TEC current is changed accordingly in order to keep the resistance at the set value. The temperature dependence of the wavelength of the diode laser is shown in Fig. 28. The absolute change in the wavelength does not depend much from the diode current and therefore Fig. 28 can be used directly to tune the wavelength without additional wavelength measurements unless very accurate value is needed.

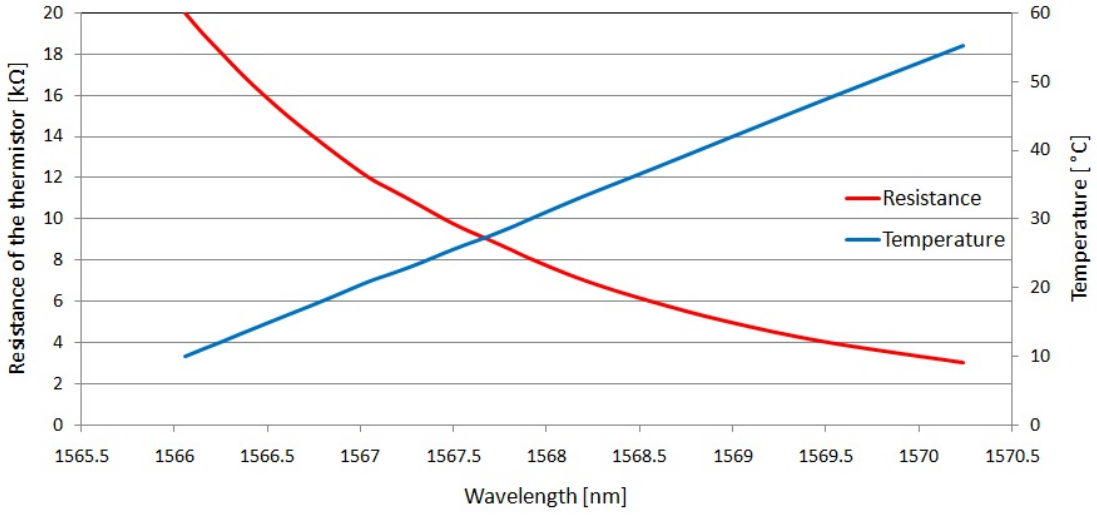

Figure 28: Wavelength of a laser diode as a function of temperature.

5.2 Interferometer

The movement of the cantilevers is detected from the interference pattern of a 633 nm HeNe-laser. The displacement of the cantilever is measured with the photodetectors shown in Fig. 29 by adjusting the reference mirror until only one interference fringe covered both halves with a phase difference of $\pi/2$ between them. The other branch is detected in a similar way while having a phase difference of π with the first branch.

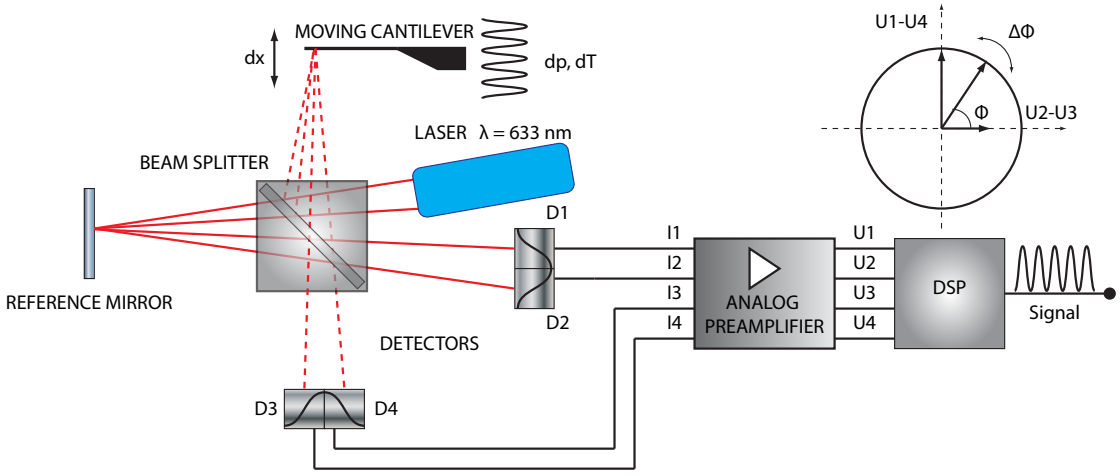

Figure 29: Signal generation in a Michelson interferometer. Redrawn from [20].

If the detector signals are marked as U_1, U_2, U_3 and U_4, where the first two signals come from the detectors in the first branch and the last two from the second branch, the displacement of the cantilever will be seen as a phase difference

$$\phi = \arctan\left(\frac{U_1 - U_4}{U_2 - U_3}\right). \tag{81}$$

A displacement of $\lambda/2$ is seen as a phase difference of 2π. This phase change is due to the change in the optical path length for the incident and reflected beams. This method can be used to measure the distances of multiple wavelengths because when the phase difference exceeds 2π another interference fringe appears in the detectors and the multiple half wavelengths can be calculated from the number of the interference fringes. [20]

Signals from the photodiodes are amplified and transferred to a digital signal processor (DSP). DSP calculates the displacement of the cantilever from the signal. Every time the signal from a channel goes from +1 V through -1 V to +1 V, the cantilever moves by 316.5 nm. These signals are combined into a voltage signal proportional to the displacement that is transmitted to the computer.

The interferometer is first calibrated by moving and tilting the reference mirror until a clear interference pattern is seen. This pattern is caused by the movement of the cantilever due to noise or applied vibrations. A slight misalignment between the detectors or difference in the sensitivity of the photodetectors is compensated with

tunable amplifiers. This tuning is done by connecting the detectors to an oscilloscope set in an X-Y-mode. The amplification settings are correct when a round circle is formed with a 1 V radius. When real gas concentrations are measured, the signal should first be calibrated with a known reference gas in a known pressure. The intended use for this setup is only to compare various cantilevers and therefore this calibration was omitted.

5.3 Signal processing

The calibrated signal is Fourier transformed from the time into the frequency domain using the Hanning window function with 16384 samples sized blocks. The block size N_{FFT} determines the frequency resolution Δf which is inversely proportional to the measurement time t and directly proportional to the sampling frequency f_{s} and is given by

$$\Delta f = \frac{1}{t} = \frac{f_{\mathrm{s}}}{N_{\mathrm{FFT}}}. \tag{82}$$

The Hanning window function, also known as Hann window, obtains the element y_{i} from the original sequence element x_{i} by

$$y_{\mathrm{i}} = 0.5 x_i \left[1 - \cos\left(\frac{2\pi n}{N_{\mathrm{FFT}}}\right)\right], \tag{83}$$

where the $n = 0, 1, 2, ..., N_{\mathrm{FFT}} - 1$. The Fourier transformed signal is averaged 100 times in order to decrease the Brownian noise amplitude. Since the Brownian noise can be approximated as a white noise, different samples do not correlate and the sum of the signals is obtained by

$$e_{100} = \sqrt{\sum_{i=1}^{100} e_{\mathrm{i}}^2}. \tag{84}$$

Since the signals are fully correlated, they can be directly summed and thus new SNR for high frequencies (since the 1/f noise correlate partly) will be

$$SNR_{\mathrm{N}} = \frac{S_1 + S_2 + ... + S_N}{\sqrt{e_1^2 + e_2^2 + ... + e_{\mathrm{N}}^2}} = \frac{N \cdot S_0}{\sqrt{N} e_0} = \sqrt{N} \cdot SNR_0, \tag{85}$$

where SNR_0 is the signal to noise ratio of each measurement.

5.4 Sample gas

The tunable range of the laser overlaps with 1006 absorption lines of various gases from which the 100 strongest peaks are shown in Fig. 30. Carbon monoxide (CO) has the second strongest intensity but due to its dangerous nature, carbon dioxide (CO_2), water vapor (H_2O) and nitrous oxide (N_2O) offer better choices for the sample gas. The average width of the absorption peaks of carbon dioxide is 23 pm and the linewidth of the laser 150 pm. When the distance between the absorption

peaks is less than 150 pm, they cannot be separated with the laser and thus the wavelength modulation cannot be used. The same problem arises if small amount of sample gas is mixed with air if the carbon dioxide concentration is relatively high. Therefore the chamber must first be flushed for example with nitrogen before other sample gas are added.

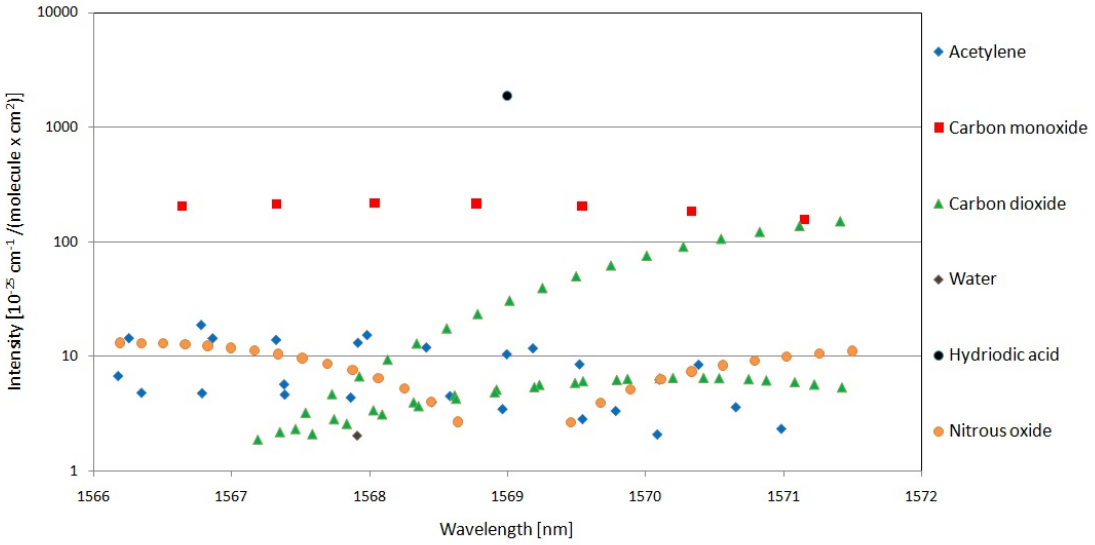

Figure 30: Absorption peaks overlapping with the used diode laser range.

Since the volumes of the sample cell and the balance cell are relatively small (2 ml and 8 ml), small concentration of sample gas cannot be easily added from a high pressured N_2O tank. A pure nitrous oxide sample gas can be added by using high pressure N_2O flow to flush the chamber. The outflow valve is then closed and the pressure in the chamber is reduced to 1 bar through a safety valve. The inflow valve connecting the chamber to the gas tank should be closed as soon as the valve ceases the work in order to prevent the sample from mixing with air.

For low pressure measurements, the sample cell can be connected to a vacuum pump. The pressure in the system can be monitored between 10^{-9} and 2 bar with a Combivac CM 32 pressure sensor connected between the photoacoustic cell and the pipe. The Vacuumbrand MZ 2D diaphragm based vacuum pump is able to drop the pressure down to 8 mbar. Special caution must be maintained when the vacuum pump is used with to the photoacoustic cell since the air flow can break the cantilever inside the cell if the pressure difference between cavities is too high.

5.5 Measurement series

A series of cantilevers was fabricated and measured in order to obtain signal and noise spectra for variously sized cantilevers. The different sizes for the cantilevers are shown in Table 2. The gold coating was deposited on both sides of the cantilevers in order to increase the reflectance. The gold coating for the 9.5 μm thick cantilevers were 50 nm thick and for the 5 μm thick cantilevers 56 nm thick. The cantilevers

with 17.4 and 16.7 μm gap widths were made with DRIE etching and the rest with TMAH etching. The initial thickness variation of the device layer was 0.5 μm, which is omitted from the models, though. The cantilevers were measured at 1 bar pressure and approximately 300 K temperature. The photoacoustic system was fixed on gel dampeners that were placed on an actively dampened optical table.

Table 2: Measured cantilevers.

Length [mm]	Width [mm]	Gap width [μm]	Thickness [μm]	Gold coating
5	1.2	3.3	9.5	X
5	1.2	2.3	9.5	
4	1.5	5.1	9.5	X
4	1.5	17.4	9.5	X
6	1.5	3.8	9.5	X
6	1.5	16.7	9.5	X
3	1.5	3.1	9.5	
3	1.5	21.2	5	X
3	1.5	25.6	5	X

5.6 FEM models

FEM models of the cantilevers were made with Comsol Multiphysics 3.4. A thin frame around the cantilever has been shown to affect the resonance frequency of the cantilever [37]. The relation between the frame width and the spring constant was tested by modeling cantilevers with a frame width varying from 0 to 1 mm at 0.1 mm steps. The frame width models were done with 5 mm x 1.2 mm x 10 μm sized cantilevers. Shaped cantilevers shown in Fig. 31 (b) and (c) were modeled without the frame. A few simplifications were used in the FEM models. The sloped walls and the rounding of corners were omitted, the gap width was assumed to be 5 μm for all of the cantilevers and the residual stress on the cantilevers was assumed to be insignificant. The 380 μm thick frame was replaced with an infinitely high wall, which made calculations faster without any visible changes in the results.

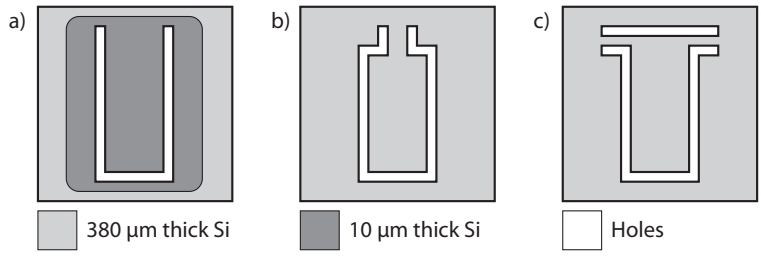

Figure 31: (a) Wide frame (b) racket shaped cantilever (c) T-shaped cantilever.

6 Results

In order to make reliable gas concentration measurements, the signal and noise generation in a photoacoustic system must be known. A theoretical basis for the signal generation and the noise sources were presented in Chapter 3. The first part of this chapter is dedicated to the noise analysis showing dominant noise sources in the measurements. In the second part, the photoacoustic system was tested by measuring carbon dioxide from the room air as well as pure nitrous oxide. The measured values were compared against the model. The last part of this chapter presents various FEM models of shaped cantilevers.

6.1 Noise measurements

Due to the almost constant power spectral density, Brownian noise can be used to detect the whole frequency response of the cantilevers during one measurement. Therefore noise was used to excite bare silicon and gold coated cantilevers. The measured noise spectra of the two 5 mm long cantilevers are shown in Fig. 32. As predicted in Chapter 3, the sensitivity is limited by Brownian and 1/f noise.

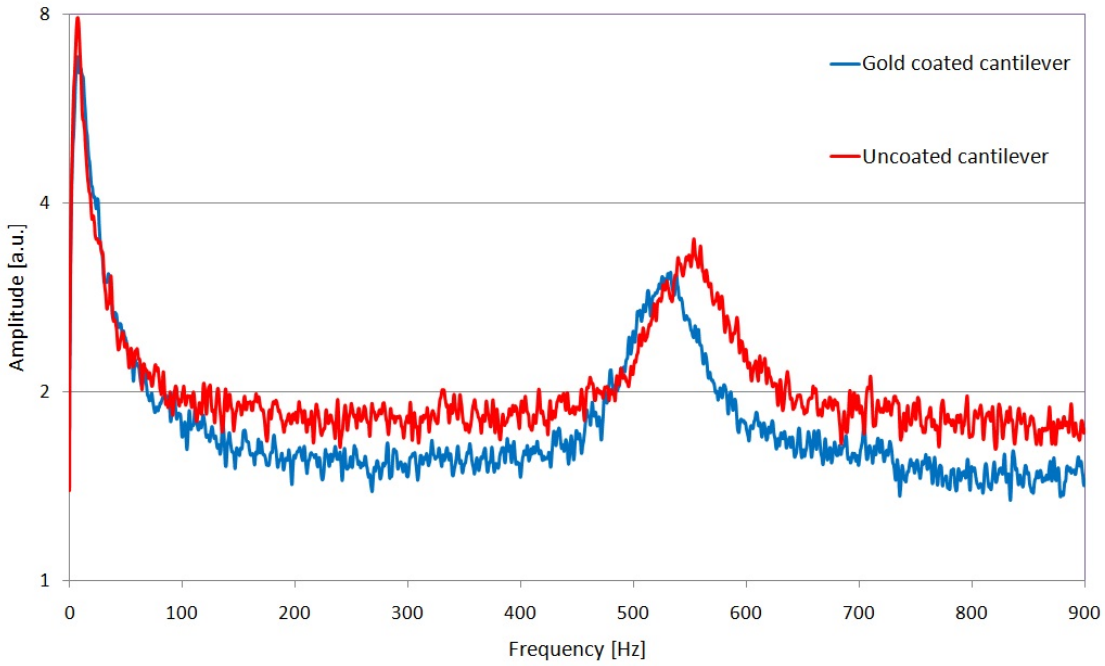

Figure 32: Noise spectrum of a 5 mm long cantilevers.

The noise spectrum corresponding to the 5 mm long cantilevers shows unexpected changes in the system response when the cantilevers are coated. A 50 nm thick gold coating on both sides should increase the effective spring constant by 1.6 %. Due to the gold coating, the noise signal decreased by 11.6 %, which exceeds the expected value quite much. Since the Young's modulus of gold (79 GPa) is smaller than that of silicon, the main reason for this change is probably the residual stress of the

coating, which effectively makes the cantilever more rigid. The gold coating led to the decrease of the resonance frequency from 548 Hz to 526 Hz (4.0 %). This change is somewhat unexpected since the resonance frequency should be proportional to $\sqrt{k/m_{\text{eff}}}$. The effective mass increased by 33.1 %, which is much more than the mass of gold coating (8 %).

6.2 Low frequency noise

The low frequency noise spectrum was measured from 4 mm long cantilevers at the university of Turku. The two 4 mm long cantilevers with different gap widths showed both similar noise spectra at the low frequency range as shown in Fig. 33. The DRIE processed cantilever with a 17.4 μm wide gap shows larger amplitude oscillations than the TMAH processed cantilever with a 5.1 μm wide gap. Since the peaks of the oscillations are at the same frequencies, it is highly probable that they are caused by the same sources.

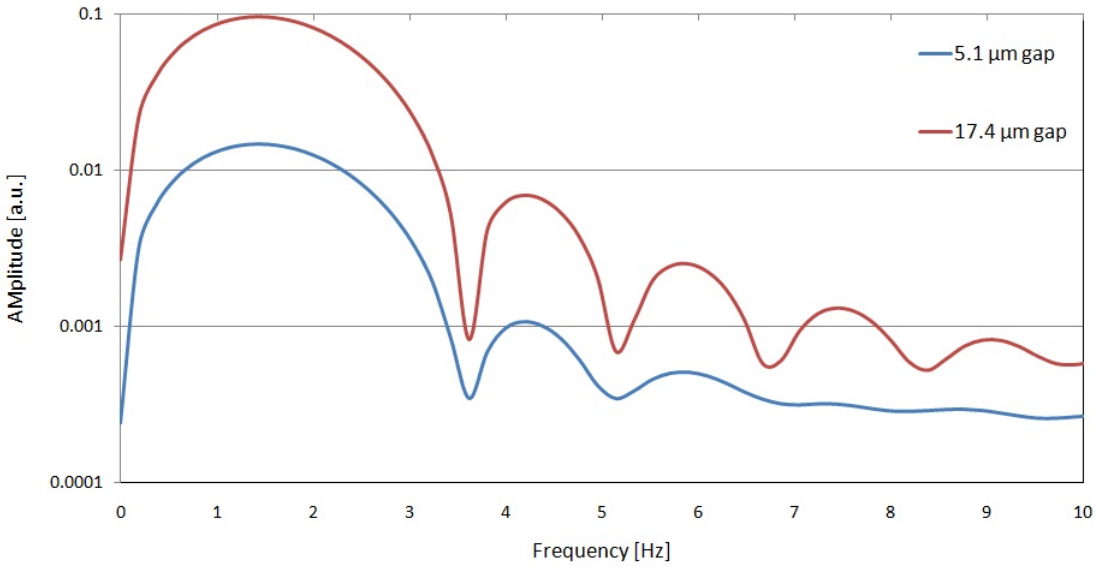

Figure 33: Low frequency noise spectra of 4 mm long cantilevers.

The measurements could not be repeated easily since low frequency noise changed almost constantly. External noise components have usually larger amplitude than the oscillations shown in Fig. 33. When the noise measurements were repeated at Micronova, a wide band, varying, low frequency noise component was detected which prevented the low frequency noise comparison between the cantilevers. The very low frequency noise (less than 10 Hz) is mainly due to the acceleration noise, i.e. building vibrations, which can be caused for example by the traffic outside the building, fans and vibrating machines and people walking by. Higher frequency 1/f noise in turn is probably caused by acoustical sources and gas flow through the gap. The measured noise spectra of 6 mm long cantilevers are shown in Fig. 34.

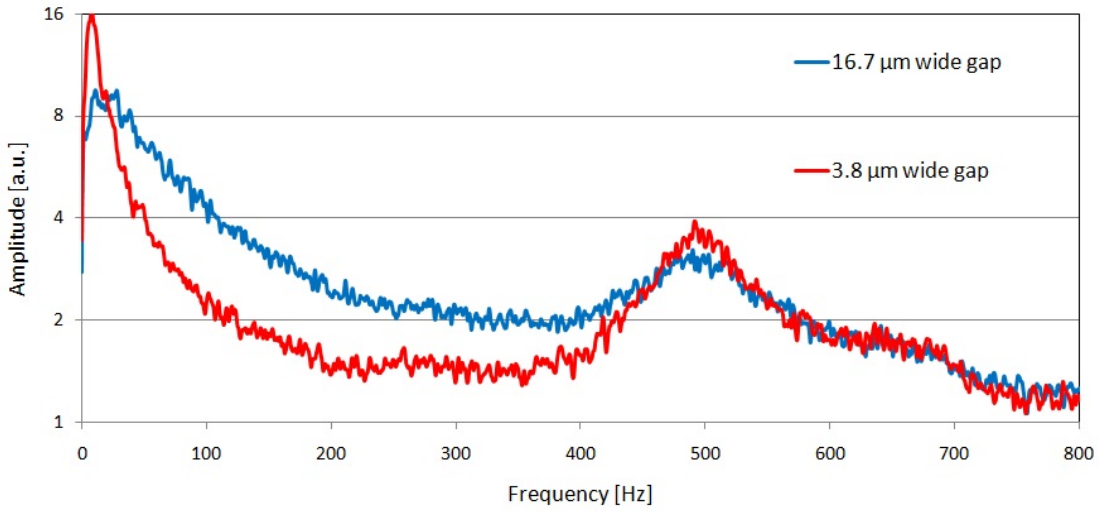

Figure 34: Noise spectra of two 6 mm long cantilevers.

Unlike in the previous measurements, no similar low frequency components could be seen in the noise spectra. Still, larger gap seems to spread the 1/f noise to higher frequencies. This effect could be connected to the increase of the gas flow through the larger gap area.

6.3 Low pressure noise

Even though Brownian noise is usually the main noise source, other noise components can become dominant when the pressure is reduced. A 5 mm long cantilever was used in the measurements of the noise spectra shown in Fig. 35 at three different pressure levels. Regardless of the pressure, the Brownian noise is the dominant source. Sharp peak at 100 Hz is caused by an electrical interference. The high peak at 50 Hz at 10 mbar is also probably due to the coupling of voltage from power lines. Since the 1/f noise is reduced with the pressure, we can assume that it requires gas molecules, i.e. it is either caused by the gas flow or by an external acoustic source coupled to the system.

When the pressure is reduced to 160 mbar, a slight decrease is seen in the Brownian noise amplitudes. This effect is due to the increase in the quality factor and the decrease in the spring constant, which partly compensate each other. When the pressure is further decreased to 10 mbar, the same kind of effect can be seen. Due to the relatively large increase in the resonance peak, we can see that the quality factor is indeed limited by the pressure. The Q values derived from the measurements were 24, 30 and 70 when the pressure was 1 bar, 160 mbar and 10 mbar, respectively. Even though reducing pressure lowers the spring constant and Brownian noise due to the reduced gas spring and higher Q value respectively, we must take into an account the partial pressure term in the absorption part of the SNR_{B} in Eq. 67. If the partial pressure p_{x} of the sample gas decreases with the total pressure, the SNR_{B} is in fact reduced since the noise amplitude decreases less than the signal.

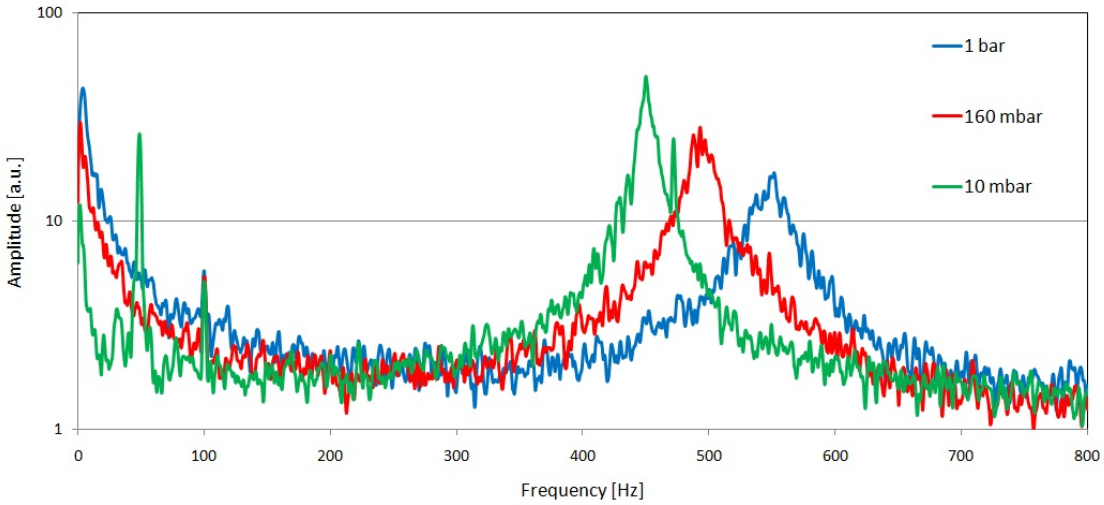

Figure 35: Noise spectra of 4 mm long cantilever at reduced pressures.

6.4 Sample gas measurements

The signal generation in the system was tested with various cantilevers using both carbon dioxide and nitrous oxide as the sample gases. The voltage measured from the DSP is proportional to the displacement of the cantilever. Since the DSP can be used in a wide range of displacements, it has a variable amplifier in order to tune the output voltage. All of the following measurements were made with the same amplification. The displacement of the cantilever is mostly less than $\lambda = 633$ nm. The first measurements were made with a mixture of 95 % nitrous oxide and 5 % air using 2.5 mW of optical power. The measured signal with 50 different modulation frequencies is shown in Fig. 36. The model derived in Chapter 3 can be fitted to overlap very well with the measured peaks. In order to fit the resonance peaks of the measurements and the model at the same frequency, the ratio of the effective spring constant and effective mass of the cantilever had to be divided by 2.36. This indicates that the effective mass is mostly due to the sample gas. The measured Q value was 17.

6.4.1 Carbon dioxide measurements

After the initial tests, the sample gas was removed and the measurements were made in air using 6 mm long cantilevers. The signal spectrum with 50 different modulation frequencies is shown in Fig. 37. The optical power of the laser was 35 mW at 1569 nm. Again, the model can be fitted very well to the measurements when the effective mass was multiplied by 2.36. The measured Q value was 16.

The previously measured cantilevers might have been exposed to dust and fiber particles before the signal measurements. When a contaminated 6 mm long cantilever was sunk in an isopropyl alcohol bath and shaken with ultrasound, the Q value was increased to 21. Unfortunately, the cantilevers break easily in a liquid and therefore this method cannot be used continuously.

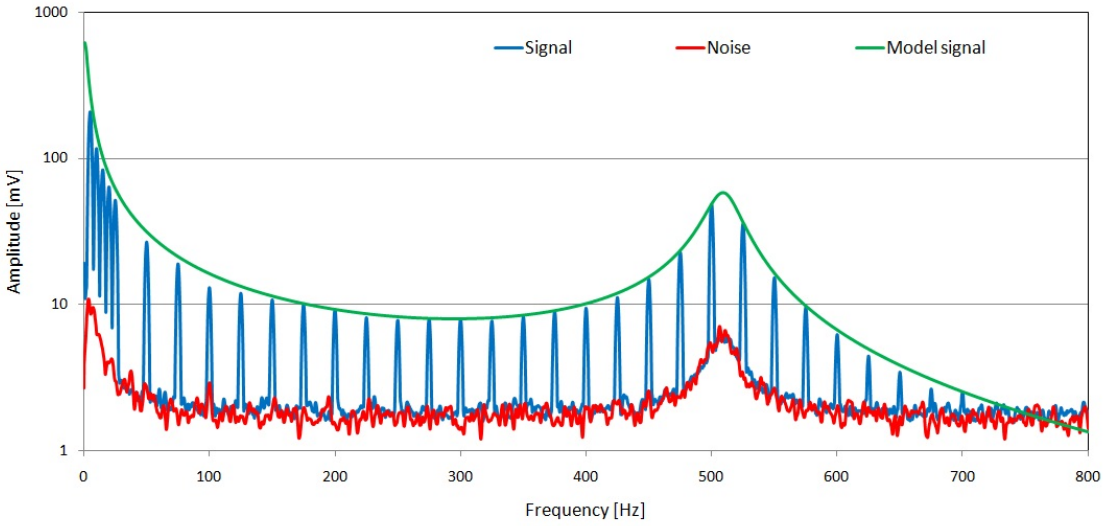

Figure 36: Signal and noise spectra with the 5 mm long cantilevers.

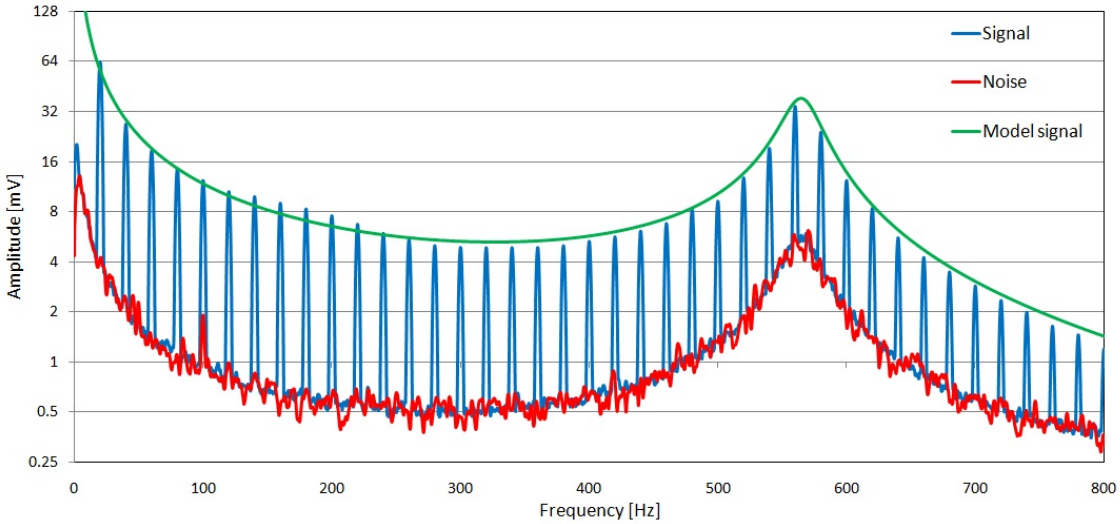

Figure 37: Signal and noise spectra with the 6 mm long cantilevers.

When two fresh 4 mm long cantilevers were used, a more pronounced resonance peaks were seen as is shown in Fig. 38. The measured Q value was 23, which is almost 10 % higher than the Q value of a cleaned cantilever. The calculated effective mass was only 2.2 times the effective mass of the cantilever.

Even though the two 4 mm long cantilevers were similarly sized except the width of the gap, large differences in the signal and noise spectra can be seen. The model predicts higher attenuation due to a larger gap at below 200 Hz. Still, the measured differences greatly exceed the values predicted by the model (34 % instead of 9 % at 100 Hz). This difference can be due to the change in the carbon dioxide concentration of air or some defects in the structure of one of the cantilevers. A slight shift in the resonance frequency (1.2 %) supports the latter one.

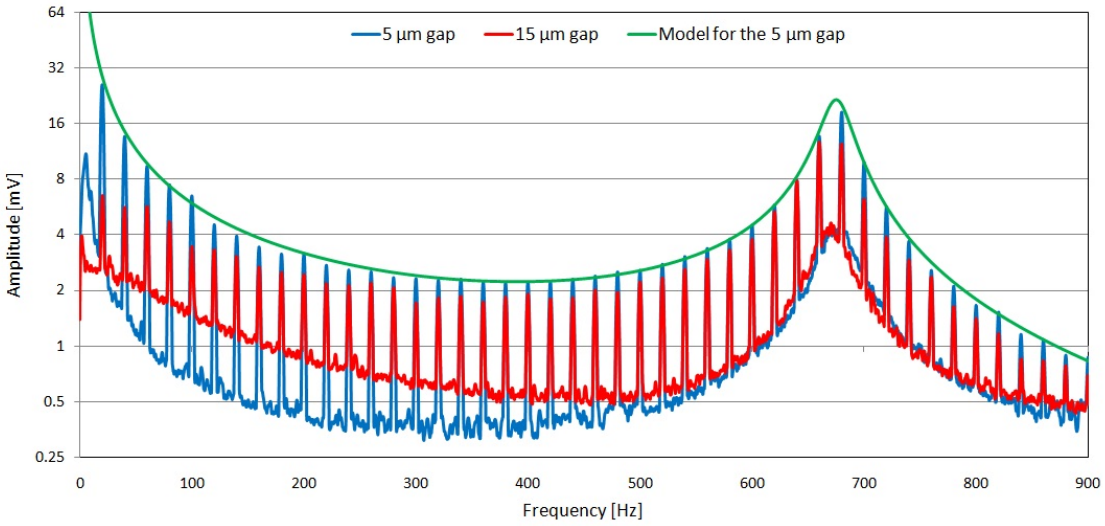

Figure 38: Signal and noise spectra of two 4 mm long cantilever.

Even larger difference can be seen in the noise spectra at frequencies below the resonance peak. 1/f noise is presumably caused by the gas flow through the gap between the cantilever and the frame. A larger gap leads to wider 1/f noise, which could be explained by an increased gas flow. Since the total energy of the vibrations due to the 1/f and Brownian noise should equal to the thermal energy, both noise spectra should cover the same area. Still, the area defined by the noise spectrum of the cantilever with 15 μm wide gap is clearly larger than the area defined by the other cantilever.

6.4.2 Thin cantilevers

Similar results were obtained with the 10 μm thick and 3 mm long cantilever shown in Fig. 39. The value for the correction factor for the effective mass was 2.38 and the measured Q value was 18. The deformation of the resonance peak at 950 Hz is due to wideband noise components, which can fortunately be ignored with low-frequency measurements. The 5 μm thick cantilevers had slightly reduced Q values of 18 and 16 whereas the correction factor for the effective mass was increased to 2.63. This is expected, since only the mass of the cantilever is reduced.

When the 10 μm thick cantilever is compared with the two 5 μm thick cantilevers, an unexpected increase in the signal-to-noise ratio is seen. Even though the Brownian noise should increase as much as the signal, the thinner cantilevers have much better SNR between 300...800 Hz despite their larger gap as shown in Fig. 40. This phenomenon can be explained if the SNR of the thicker cantilever is limited by electrical noise. Since the electrical noise is coupled to the system after the interferometer, it remains the same despite the movement of the cantilever. When a more sensitive cantilever is used, only the signal and the Brownian noise are amplified. The noise peak at 470 Hz was due to the acoustical noise of the fan of the laser current controller.

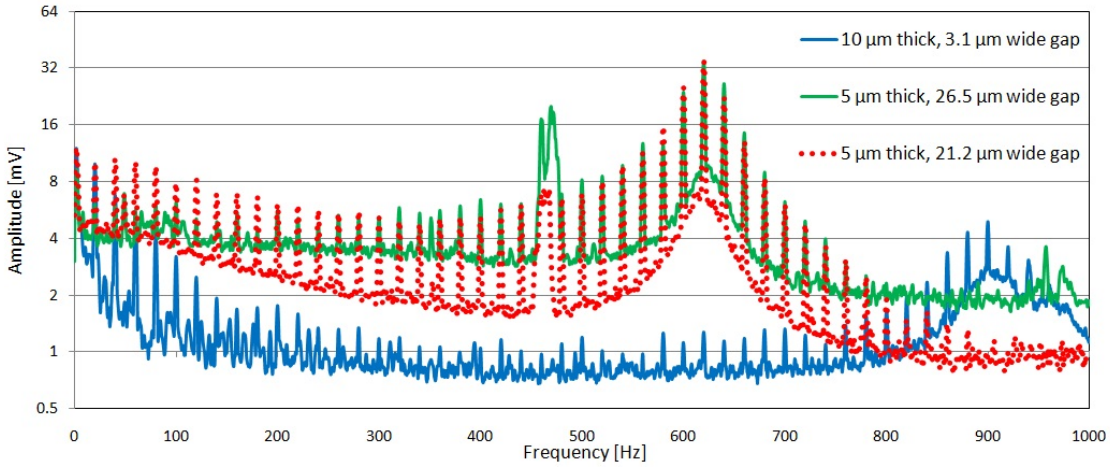

Figure 39: Signal and noise spectra with the 3 mm long cantilevers.

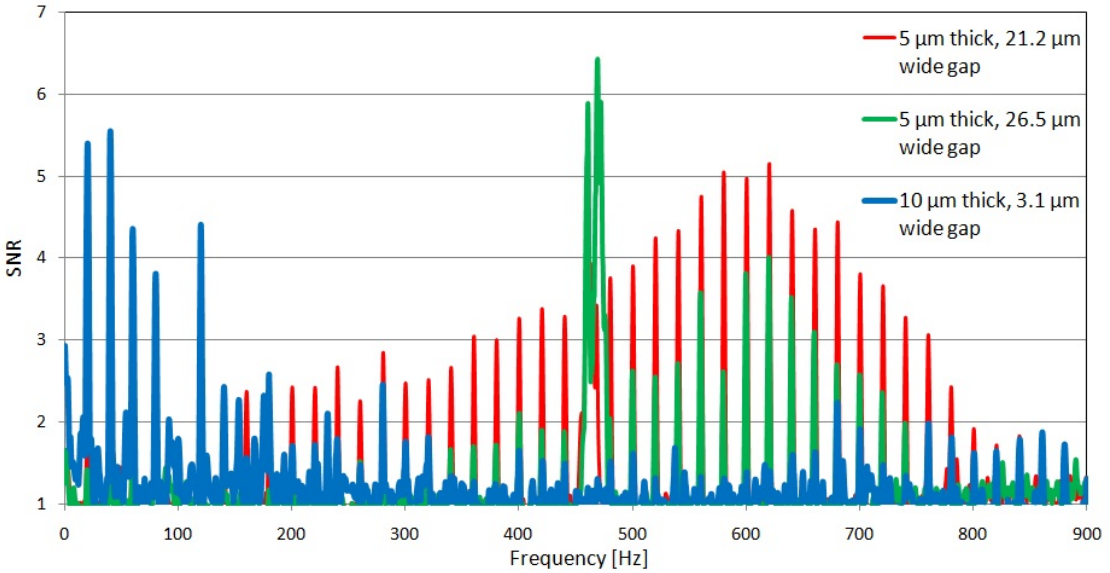

Figure 40: Signal-to-noise ratio of 3 mm long cantilevers.

Even though the signal model could easily be fitted to the measurements, a large difference between the model and the measurements was seen with the thin cantilevers as is shown in Fig. 41. When the measured value (21.2 μm) was used for the gap, the model greatly exaggerated the signal at low frequencies. In order to fit the model to the measurements, the width of the gap had to be increased to an unrealistic value of 660 μm. The similar effect was seen when the measurements were repeated with the other thin cantilever. In that case, the width of the gap had to be increased from 26.5 μm to 1.2 mm.

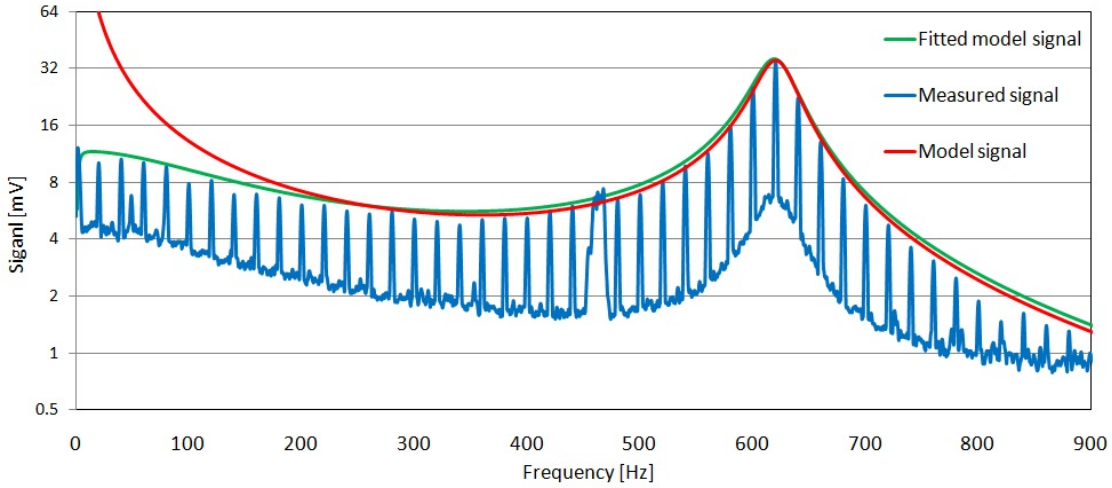

Figure 41: Signal and modeled spectra with a 3 mm long cantilever.

6.5 FEM models

With the current cantilevers, almost 60 % of the effective spring constant is due to the gas spring. Instead of making the cantilever thinner, changing the shape of the cantilever can have a significant effect on the spring constant. In the first models, a racket like shape shown in Fig. 31 (b) was used. The width of the handle was varied from 0.1 mm to 1.2 mm with 0.1 mm steps and these measurements were repeated with 5 μm, 100 μm, 1 mm and 3.8 mm long handles. The cantilevers were excited with 1 Pa pressure waves and the maximum displacement was numerically calculated. The effective spring constant calculated from the displacements is shown in Fig. 42. Since the gas spring is the main source of the spring constant, the cantilevers with the smallest surface area show the smallest effective spring constant.

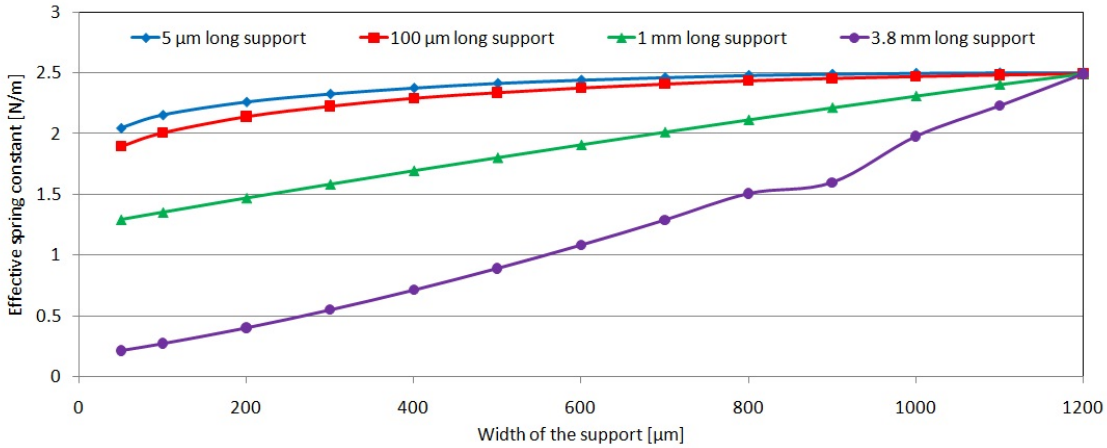

Figure 42: Modeled spring constant of a racket shaped microphones.

Another way to reduce the spring constant is to use hinged structures shown in Fig. 31 (c). In the hinged structures, the connection between the cantilever

and the frame is moved from the end of the cantilever to the sides. These hinged structures were compared with cantilevers connected to a wide, thin frame. The current cantilevers are connected to an approximately 0.5 mm wide frame shown in Fig. 31 (a), which acts as a flexible membrane. A small decrease in the spring constant can be seen due to this membrane as shown in [37]. If the hinged structures connected would be connected directly to the thick frame only from the ends of the hinges, smaller spring constants could be achieved as shown in Fig. 43.

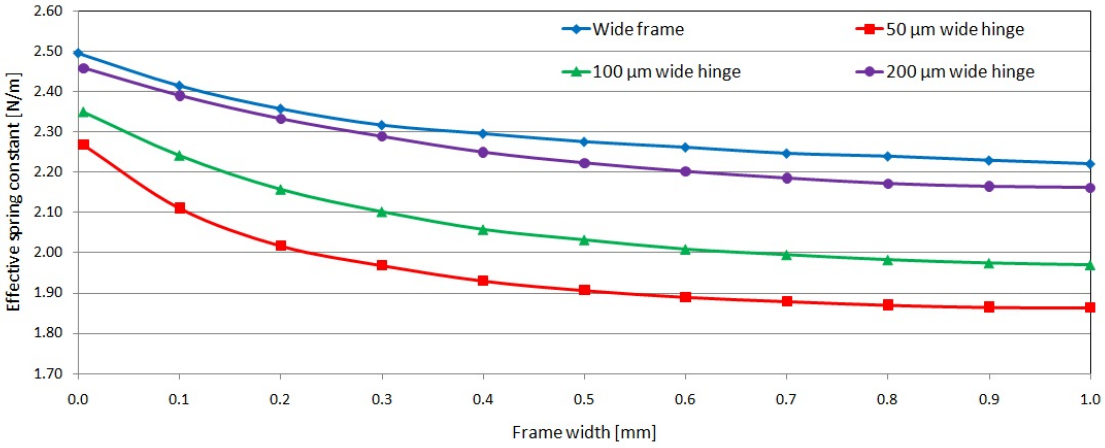

Figure 43: Effective spring constant of four modeled cantilevers.

As we can see from Fig. 43, the effective spring constant of the cantilever reduces only by 10 % when the width of the thin frame changes from 0 to 1 mm. 50 μm wide hinges could be used to reduce the spring constant by 20 % using the same space. Unfortunately, these hinges would also be much more fragile than the thin frame, which in practice makes them useless.

7 Conclusions

The photoacoustic phenomenon was discovered at the end of the 19th century. The method remained rather unused until the development of lasers in the 60s made it possible to use photoacoustics in many new applications. Further advancements in developing IR sources increased the sensitivity of the photoacoustic systems until the theoretical limit of the membrane based microphones was reached. This limit was bypassed when the condenser microphones were replaced with quartz tuning forks and optically measured cantilevers. The sensitivity was increased over ten times with tuning forks and over a hundred times with micromachined cantilevers.

In this work, a literature review was made in order to establish a clear picture of the current state of the photoacoustic spectroscopy. The review presented various structures used in a modern photoacoustic setup. In order to further develop cantilever microphones, a short mathematical review was also given from the signal generation in the photoacoustic system.

The main properties affecting the sensitivity of the cantilever are the length, width, thickness and the size of the gap between the cantilever and the frame. The width, the thickness and the gap size are limited by the available wafers, the spot size of the laser and the fabrication process, respectively. Only the length and the shape can be freely changed, which limits the possibilities of developing the cantilevers.

A smaller gap increases the signal at low frequencies, but it also affects the noise properties. Wide gaps have shown spectrally wider 1/f noise, which limits the signal-to-noise ratio. Still, even relatively wide gaps (several dozens of micrometers) do not totally prevent measurements. Even though the modeled gap effect coincided with the measurements at small gap sizes, a significant difference occurred when the gap width increased over 20 μm. Due to the small number of cantilevers with a large gap, more samples are needed before this effect can be verified and modeled.

Two novel 5 μm thick cantilevers were measured and compared against similarly sized 10 μm cantilevers. A remarkable increase in the signal-to-noise ratio was detected, which cannot be explained with the current model if a Brownian noise limited system is used. It may be possible that the sensitivity is limited by electrical noise, even though most of the measurements seemed to be Brownian noise dominated. A higher number of thin cantilevers with different sizes are needed in the future in order to find out the reason for this phenomenon.

By using low optical power with amplitude modulation, successful measurements were performed with N_2O. The assembled setup can easily be used to measure carbon dioxide from the air if the optical power is increased to 30 mW. Even though a clear dependence can be seen between the size of the cantilever and the sensitivity and the signal-to-noise ratio, the sample gas induces even larger effects. Numerical values for the sample gas effects can be calculated when the cantilevers are modeled as harmonic oscillators. For the current cantilevers, the gas spring can form 2/3 of the effective spring constant and almost 3/5 of the effective mass. Two sets of differently shaped cantilevers were modeled with the finite element method, which showed that a racket shaped microphone could be used to reduce these effects.

References

[1] Harren, F. J. M., Cotti, G, Oomens, J., te Lintel Hekkert, S., *Photoacoustic Spectroscopy in Trace Gas Monitoring*, in: Meyers, R. A. (ED), *Encyclopedia of Analytical Chemistry*, John Wileys & Sons Ltd, Chichester, 2000, p. 2203–2226.

[2] Patel, C. K. N., *Laser Photoacoustic Spectroscopy Helps Fight Terrorism: High Sensitivity Detection of Chemical Warfare Agent and Explosives*, The European Physical Journal - Special Topics, vol. 153:1, 2008, p. 1–18.

[3] Sigrist, M. W., *Trace Gas Monitoring by Laser-photoacoustic Spectroscopy*, Infrared Physics & Technology, vol. 36:1, 1994, p. 415–425.

[4] Uotila, J., Koskinen, V., Kauppila, J., *Selective Differential Photoacoustic Method for Trace Gas Analysis*, Vibrational Spectroscopy, vol. 38:1–2, 2005 p. 3–9.

[5] Besson, J.-P., *Photoacoustic Spectroscopy for Multi-gas Sensing Using Near Infrared Lasers*, Ph.D. Thesis, École Polytechnique Fédérale de Lausanne, La Faculté Sciences et Techniques de l´ingénieur, Lausanne, 2006.

[6] West, G., Barrett, J. J., Siebert, D. R., Reddy, K. V., *Photoacoustic Spectroscopy*, Review of Scientific Instruments, vol. 54:7, 1983, p. 797–817.

[7] McDonald, F. A., Wetsel, G. C. Jr., *Generalized Theory of the Photoacoustic Effect*, Journal of Applied Physics, vol. 49:4, 1978, p. 2313–2322.

[8] Wilcken, K., Kauppinen, J., *Optimization of a Microphone for Photoacoustic Spectroscopy*, Applied Spectroscopy, vol. 59:9, 2003, p. 1087–1092.

[9] Rothman, L. S. *et al.*, *The HITRAN 2008 Molecular Spectroscopic Database*, Journal of Quantitative Spectroscopy and Radiative Transfer, vol. 110:9–10, 2009, p. 533–572.

[10] Wolff, M., Harde, H., *Photoacoustic Spectrometer Based on a Planckian Radiator with Fast Time Response*, Infrared Physics & Technology, vol. 44:1, 2003, p. 51–55.

[11] Miklós, A., Hess, P., Bozóki, Z., *Application of Acoustic Resonators in Photoacoustic Trace Gas Analysis and Metrology*, Review of Scientific Instruments, vol. 72:4, 2001, p. 1937–1955.

[12] Veres, A., Bozóki, Z., Mohácsi, Á., Szakáll, M., Szabó, G., *External Cavity Diode Laser Based Photoacoustic Detection of CO_2 at 1.43 μm: The Effect of Molecular Relaxation*, Applied Spectroscopy, vol. 57:8, 2003, p. 900–905.

[13] Silfvast, W. T., *Laser Fundamentals*, Cambridge, Cambridge University Press, 2004.

[14] Fitel 1550 nm CW DFB Laser Diode Module Component Specifications, Version B, 2007, refered 30.8.2010, available: `http://www.ilxlightwave.com/laser-diode/Data/FITEL_FOL15DCWx-Axx-xxxxx-x.pdf`.

[15] Yu, C-S., K. A. H., *Grazing-incidence Periodically Poled $LiNbO_3$ Optical Parametric Oscillator*, Journal of the Optical Society of America B, vol. 16:12, 1999, p. 2233–2238.

[16] Kosterev, A., Wysocki, G., Bakhirkin, Y., So, S., Lewicki, R., Fraser, M., Tittel, F., Curl, R. F., *Application of Quantum Cascade Lasers to Trace Gas Analysis*, Applied Physics B: Lasers and Optics, vol. 90:2, 2008, p. 165–176.

[17] Bijnen, F. G. C., Reuss, J., Harren, F. J. M., *Geometrical Optimization of a Longitudinal Resonant Photoacoustic Cell for Sensitive and Fast Trace Gas Detection*, Review of Scientific Instruments, vol. 67:8, 1996, p. 2914–2923.

[18] Saarela, J., Toivonen, J., Manninen, A., Sorvajärvi, T., Hernberg, R., *Wavelength Modulation Waveforms in Laser Photoacoustic Spectroscopy*, Applied Optics, vol. 48:4, 2009, p. 743–747.

[19] Kuusela, T., Kauppinen, J., *Photoacoustic Gas Analysis Using Interferometric Cantileve Microphone*, Applied Spectroscopy Reviews, vol. 42:5, 2007, p. 443–474.

[20] Uotila, J, *Use of Optical Cantilever Microphone in Photoacoustic Spectroscopy*, Ph.D. Thesis, University of Turku, Department of Physics and Astronomy, Turku, 2009.

[21] Tavakoli, M., Tavakoli, A., Taheri, M., Saghafifar, H., *Design, Simulation and Structural Optimization of a Longitudinal Acoustic Resonator for Trace Gas Detection Using Laser Photoacoustic Spectroscopy (LPAS)*, Optics & Laser Technology, vol. 42:5, 2010, p. 828–838.

[22] Koch, K. P., Lahmann, W., *Optoacoustic Detection of Sulphur Dioxide Below the Parts Per Billion Level*, Applied Physics Letters, vol. 32:5, 1978, p. 289–291.

[23] Herriott, D., Kogelnik, H., Kompfner, R., *Off-Axis Paths in Spherical Mirror Interferometers*, Applied Optics, vol. 3:4, 1964, p. 523–526.

[24] McManus, J. B., Kebabian P. L., Zahniser, M. S., *Astigmatic Mirror Multipass Absorption Cells for Long-Path-Length Spectroscopy*, Applied Optics, vol. 34:18, 1995, p. 3336–3348.

[25] Shtrikman, S., Slatkine, M., *Trace Gas Analysis with a Resonant Optoacoustic Cell Operating Inside the Cavity of a CO_2 Laser*, Applied Physics Letters, vol. 31:12, 1977, p. 830–831.

[26] Harren, F. M. J., Bijnen, F. G. C., Reuss, J., Voesenek, L. A. C. J., Blom, C. W. P. M., *Sensitive Intracavity Photoacoustic Measurement with a CO_2 Waveguide Laser*, Applied Physics B: Lasers and Optics, vol. 50:2, 1990, p. 137–144.

[27] Kosterev, A. A., Bakhirkin, A., Curl, R. F., Tittel, F. K., *Quartz-enhanced Photoacoustic Spectroscopy*, Optics Letters, vol. 27:21, 2002, p. 1902–1904.

[28] Kosterev, A. A., Tittel F. K., Serebryakov, D. V., Malinovsky, A. L., Morozov, I. V., *Applications of Quartz Tuning Forks in Spectroscopic Gas Sensing*, Review of Scientific Instruments, vol. 76:4, 2005.

[29] Liu, K., Li, J., Wang, L., Tan, T., Zhang, W., Gao, X., Chen, W., Tittel, F. K., *Trace Gas Sensor Based on Quartz Tuning Fork Enhanced Laser Photoacoustic Spectroscopy*, Applied Physics B: Laser and Optics, vol. 94:3, 2009, p. 527–533.

[30] Koskinen, V., Fonsen, J., Roth, K., Kauppinen, J., *Cantilever Enhanced Photoacoustic Detection of Carbon Dioxide Using a Tunable Diode Laser Source*, Applied Physics B: Lasers and Optics, vol. 86:3, 2007, p. 451–454.

[31] Fonsen, J., Koskinen, V., Roth, K., Kauppinen, J., *Dual Cantilever Enhanced Photoacoustic Detector with Pulsed Broadband IR-source*, Vibrational Spectroscopy, vol. 50:2, 2009, p. 214–217.

[32] Lawall, J., Kessler, E., *Michelson Interferometry with 10 pm Accuracy*, Review of Scientific Instruments, vol. 71:7, 2000, p. 2669–2676.

[33] Cunningham, M. J., Cheng, S. T., Clegg, W. W., *A Differential Interferometer for Scanning Force Microscopy*, Measurement Science and Technology, vol. 5:11, 1994, p. 1350–1354.

[34] Peiner, E., Scholz, D., Schlachetzki, A., Hauptmann, P., *A Micromachined Vibration Sensor Base on the Control of Power Transmitted between Optical Fibers*, Sensors and Actuators A, vol. 65:1, 1998, p. 23–29.

[35] Breguet, J., Gisin, N., Pellaux, J. P., *Photoacoustic Detection of Trace Gases with an Optical Microphone*, Sensors and Actuators A: Physical, vol. 48:1, 1995, p. 29–35.

[36] McClelland, J. F., Jones, R. W., Bajic, S. J., *FT-IR Photoacoustic Spectroscopy* in: Chalmer, J. M., Griffiths, P. R. (ED), *Handbook of Vibrational Spectroscopy*, vol. 2, 2002.

[37] Sievilä, P., Rytkönen, V-P., Hahtela, O., Chekurov, N., Kauppinen, J., Tittonen, I., *Fabrication and Characterization of an Ultrasensitive Acousto-optical Cantilever*, Journal of Micromechanics and Microengineering, vol. 17:5, 2007, p. 852–859.

[38] Middelhoek S., Audet, S. A., *Silicon Sensors*, London, Academic Press, 1989.

[39] Hearn, E. J., *Mechanics of Materials: An Introduction to the Mechanics of Elastic and Plastic Deformation of Solids and Structural Materials*, Norwich, Knovel, 2001.

[40] Koskinen, V., Fonsen, J., Kauppinen, J., Kauppinen, I., *Extremely sensitive trace gas analysis with modern photoacoustic spectroscopy*, Vibrational Spectroscopy, vol. 42:2, 2006, p. 239–242.

[41] Koskinen, V., Fonsen, J., Roth, K., Kauppinen, J., *Progress in Cantilever Enhanced Photoacoustic Spectroscopy*, Vibrational Spectroscopy, vol. 48:1, 2009, p. 16–21.

[42] Gerlach, R., Amer, N. M., *Brewster Window and Windowless Resonant Spectrophones for Intracavity Operation*, Applied Physics, vol. 23:3, 1980, p. 319–326.

[43] Kovalyov, A. A., Klebleyev, N. R., *Resonant optoacoustic Detector in Nondispersive Gas Analyzer Scheme*, Infrared Physics & Technology, vol. 38:7, 1997, p. 415–421.

[44] Rey, J. M., Sigrist, M. W., *Differential Mode Excitation Photoacoustic Spectroscopy: A New Photoacoustic Detection Scheme*, Review of Scientific Instruments, vol. 78:6, 2007.

[45] Lang, H. P., Hegner, M., Gerber, C., *Cantilever Array Sensors*, Materials Today, vol. 8:4, 2005, 30–36.

[46] Franssila, S., *Introduction to Microfabrication*, John Wiley & Sons Ltd, Chichester, 2004.

[47] Sainiemi, L., *Cryogenic Deep Reactive Ion Etching of Silicon Micro and Nanostructures*, Ph.D. Thesis, Helsinki University of Technology, Faculty of Electronics, Espoo, 2009.

[48] Driscoll, W. G., Vaughan, W., *Handbook of Optics*, New York, McGraw-Hill Inc., 1978.

[49] *Refractive Index Info*, refered 16.9.2010, available: `http://refractiveindex.info/`.

[50] Braginsky, V. B., Mitrofanov, V. P., Panov, V. I., *Systems with Small Dissipation*, Chicago, University of Chicago Press, 1986.

[51] Yasumura, K. Y., Stowe, T. D., Chow, E. M., Pfafman, T., Kenny, T. W., Stipe, B. C., Rugar, D., *Quality Factors in Micron- and Submicron-Thick Cantilevers*, Journal of Microelectromechanical Systems, vol. 9:1, 2000, p. 117–125.

[52] Stemme, G., *Resonant Silicon Sensors*, Journal of Micromechanics and Microengineering, vol. 1:2, 1991, p. 113–125.

[53] Zalalutdinov, M., Olkhovets, A., Zehnder, A., Ilic, B., Czaplewski, D., Craighead, H., G., Parpia, J., M., *Optically Pumped Parametric Amplification for Micromechanical Oscillators*, Applied Physics Letters, vol. 78:20, 2001, p. 3142–3144.

[54] Liang, S., Medich, D., Czajkowsky, D. M., Sheng, S., Yuan, J-Y., Shao, Z., *Thermal Noise Reduction of Mechanical Oscillators by Actively Controlled External Dissipative Forces*, Ultramicroscopy, vol. 84:1–2, 2000, p. 119–125.

[55] Sandberg, R., Mølhave, K., Boisen, A., Svendsen, W., *Effect of Gold Coating on the Q-factor of a Resonant Cantilever*, Journal of Micromechanics and Microengineering, vol. 15:12, 2005, p. 2249–2253.

[56] Lee, S. S., White, R. M., *Piezoelectric Cantilever Acoustic Transducer*, Journal of Micromechanics and Microengineering, vol. 8:3, 1998, p. 230–238.

[57] Ledermann, N., Muralt, P., Baborowski, J., Forster, M., Pellaux, J-P., *Piezoelectric $Pb(Zr_x, Ti_{1-x})O_3$ Thin Film Cantilever and Bridge Acoustic Sensors for Miniaturized Photoacoustic Gas Detectors*, Journal of Micromechanics and Microengineering, vol. 14:12, 2004, p. 1650–1658.

[58] Fabian, J-H., Scandella, L., Fuhrmann, H., Berger, R., Mezzacasa, T., Musil, Ch., Hobrecht, J., Meyer, E., *Finite Element Calculations and Fabrication of Cantilever Sensors for Nanoscale Detection*, Ultramicroscopy, vol. 82:1, 2000, p. 69–77.